R89-917437-3

DISPERSION STRENGTHENING OF HIGH TEMPERATURE NIOBIUM ALLOYS

Prepared by
D. L. Anton
D. B. Snow
L.H. Favrow
A. F. Giamei

FINAL REPORT

Contract F49620-86-C-0053

for

Air Force Office of Scientific Research
Building 410
Bolling Air Force Base
Washington, DC 20332

July 31, 1989

**UNITED
TECHNOLOGIES
RESEARCH
CENTER**

East Hartford, Connecticut 06108

OCT 23 1989

89 10 24 078

REPORT DOCUMENTATION PAGE		Form Approved OMB No 0704-0188

1a. REPORT SECURITY CLASSIFICATION Unclassified	1b. RESTRICTIVE MARKINGS	
2a. SECURITY CLASSIFICATION AUTHORITY	3. DISTRIBUTION/AVAILABILITY OF REPORT Approved for public release;	
2b. DECLASSIFICATION/DOWNGRADING SCHEDULE	distribution unlimited.	

4. PERFORMING ORGANIZATION REPORT NUMBER(S) R89-917437-3	5. MONITORING ORGANIZATION REPORT NUMBER(S) AFOSR-TR- 89 - 1257

6a. NAME OF PERFORMING ORGANIZATION United Technologies Research Center	6b. OFFICE SYMBOL (If applicable)	7a. NAME OF MONITORING ORGANIZATION Same as 8a
6c. ADDRESS (City, State, and ZIP Code) East Hartford, CT 06108		7b. ADDRESS (City, State, and ZIP Code) Same as 8b

8a. NAME OF FUNDING/SPONSORING ORGANIZATION Air Force Office of Scientific Research	8b. OFFICE SYMBOL (If applicable) NE	9. PROCUREMENT INSTRUMENT IDENTIFICATION NUMBER F49620-86-C-0053

8c. ADDRESS (City, State, and ZIP Code) Building 410 Washington, DC 20332-6448	10. SOURCE OF FUNDING NUMBERS			
	PROGRAM ELEMENT NO. 61102F	PROJECT NO. 2306	TASK NO. A1	WORK UNIT ACCESSION NO

11. TITLE (include Security Classification)

DISPERSION STRENGTHENING OF HIGH TEMPERATURE NIOBIUM ALLOYS

12. PERSONAL AUTHOR(S)
D. L. Anton, D. B. Snow, L. H. Favrow, A. F. Giamei

13a. TYPE OF REPORT Final	13b. TIME COVERED FROM 5/86 TO 4/89	14. DATE OF REPORT (Year, Month, Day) 1989 July 31	15. PAGE COUNT 86

16. SUPPLEMENTARY NOTATION

17. COSATI CODES			18. SUBJECT TERMS (Continue on reverse if necessary and identify by block number)
FIELD	GROUP	SUB-GROUP	Niobium, Particle coarsening,
			Dispersion strengthening, Refractory metals,
			High temperature strength,

19. ABSTRACT (Continue on reverse if necessary and identify by block number)

Niobium base alloys are very attractive as high temperature materials for advanced gas turbine applications. After many conventional metal-lurgical approaches, a high temperature creep resistant alloy has yet to be identified which will replace nickel base superalloys. The best chance for obtaining high temperature creep resistance in these alloys is through dispersion strengthening with a stable precipitate that is introduced through rapid solidification. This would result in a very fine dispersion of nonshearable precipitates that would not coarsen upon long term exposure at temperatures in excess of 1200°C.

A study has been conducted here to identify such a stable dispersion, fabricate alloys through a rapid solidification approach and characterize the coarsening of the resulting precipitates. A thermodynamic argument is presented to select candidate dispersions for evaluation. Arc melted and splat quenched alloys were fabricated and evaluated through micro-hardness measurements. An indirect assessment of particle stability is introduced which resulted in a coarsening parameter determined for each candidate precipitate at 1400°C. Microscopic examination of the more stable alloys were made via optical and thin foil TEM analyses. Tensile and strain-rate sensitivity tests were run on these alloys at 1400°C.

The strongest alloys studied here were those with precipitates of the refractory metals Zr and Hf as either nitrides or borides and an alloy containing TiN. Tensile strengths were commiserate with their low alloy content and the strain rate sensitivity tests indicate large back stresses similar to that found in cast Ni-base superalloys. These precipitates were found to be in either a plate or needlelike morphology and uniformly distributed throughout the matrix. Large blocky oxides of the refractory elements were observed in the grain boundaries along with discrete particles of niobium nitrides or borides.

20. DISTRIBUTION/AVAILABILITY OF ABSTRACT ☐ UNCLASSIFIED/UNLIMITED ☒ SAME AS RPT ☐ DTIC USERS	21. ABSTRACT SECURITY CLASSIFICATION Unclassified	
22a. NAME OF RESPONSIBLE INDIVIDUAL Dr. A. H. Rosenstein	22b. TELEPHONE (Include Area Code) (202) 767-4933	22c. OFFICE SYMBOL NE

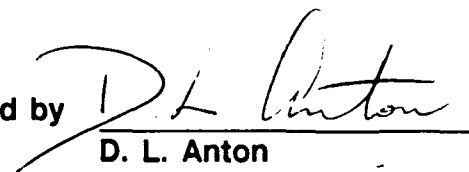DD Form 1473 JUN 86   Previous editions are obsolete.

R89-917437-3

*Dispersion Strengthening of High
Temperature Niobium Alloys*

1989 July 31
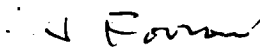
Reported by

D. L. Anton
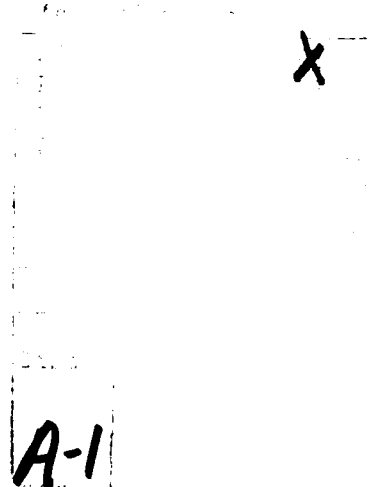
D. B. Snow

L. H. Favrow

A. F. Giamei

Approved by

E. R. Thompson

Dispersion Strengthening of High Temperature Niobium Alloys

TABLE OF CONTENTS

1.0 INTRODUCTION

The efficiency of current gas turbine engines for aerospace applications is limited by their working gas temperatures. The internal load bearing components are restricted in temperature capability by their available strength. The commonly used Ni–base superalloy have a maximum useful temperature of approximately 1176°C (2150°F). This is approaching the γ' solvus temperature, the theoretical limiting temperature of these alloys. In order to obtain improvements in thrust to weight ratio, new materials will need to be developed that are not only strong at high temperatures but also stable in oxidizing environments. These materials must have high strength–to–density ratios as well. A class of metals which has not been directly utilized in this regard is the refractory metals. In particular, niobium alloys have shown promise as being useful as structural components in high temperature applications due to their relatively low density, stable oxide, low ductile brittle transition temperature and high melting point.

A substantial effort was expended into the possible use of refractory metals as high temperature materials in the 1960's. This effort essentially terminated with the decline of the space program in the United States. However, research has continued in the Soviet Union to the present time. Two basic problems have proven to be difficult to overcome. These are oxidation resistance and high temperature creep strength. The subject of this study is to address the high temperature strength while temporarily disregarding environmental effects. The Soviet literature, as well as conclusions drawn from the western data of the 60's, indicate that for niobium alloys to have useful high temperature strength, strengthening by both solid solution as well as dispersion mechanisms will be necessary.

Solid solution strengthening in niobium alloys is well understood, but a dispersion which is stable enough to withstand extended high temperature exposure with minimum coarsening has been elusive. This program was undertaken with the intent of surveying the literature and performing screening experiments utilizing rapid solidification to form a finely dispersed particulate in a niobium matrix. Analytical transmission electron microscopy was performed to verify the dispersion's chemistry, crystallography and morphology. High temperature mechanical evaluations were performed to determine the suitability of these dispersions for gas turbine applications.

1.1 Commercial Alloying Strategies

Commercial niobium alloys can be divided into roughly three categories: high strength–low ductility, moderate strength–some ductility, and low strength–high ductility. Only the first category can be considered for very high temperature use. A list of some typical alloys and their chemistries is given in Table I (Ref. 1). To obtain high strengths it is seen that high concentrations of W and/or Ta are used. In addition to these solid solution strengtheners, Zr and

Hf are added in conjunction with C to precipitate either ZrC or HfC (Refs. 2, 3). In addition to carbide strengthening, oxides of Nb, Zr and Hf have been studied in experimental alloys (Ref. 4). These precipitates have been found to coarsen too rapidly to be used at temperatures exceeding 1000°C (1832°F) (Ref. 4). Extended exposure at these temperatures has led to rapid precipitate growth, thus reducing the strength of these alloys.

TABLE I – COMPOSITION OF ADVANCED NB–BASE ALLOYS

High Strength	W	Mo	Ta	Ti	Zr	V	Hf	Other
Cb–1	30				1			0.06C
B–88	28						2	0.06C
VAM–79	22						2	0.06C
Ch–132M	15	5	20		2.5			0.013
AS–30	20				1			0.1C
F–48	15	5			1			0.05/0.1C
Sy–31	1						3.5	0.1C
Moderate Strength and Ductility								
Su–16	11	3					2	0.08C
Fs–85	10		28		1			
D–43	10				1			0.1C
CB–752	10				2.5			
SCb–291	10		10					
C–129Y	10						10	0.2Y
B–66		5			1		5	
AS–55	5				1			0.2Y
PWC–11					1			0.1C
PWC–33					3			0.35C
Low Strength and High Ductility								
Cb–753					1.25	5		
C–103				1	0.7		10	
B–33						5		
D–14					5			
D–36				10	5			
Nb–1Zr					1			

While one of the factors in choosing Nb as a candidate for high temperature structural applications is its high melting point, it does not exhibit inherent high temperature strength. Strengthening must then come from either precipitation hardening, solid solution hardening, work hardening or a combination of thermo-mechanical treatments. Most of the commercial Nb base alloys currently being used rely to a large extent on solid solution strengthening and work hardening for their strength (Ref. 1). Work hardened alloys have been found to be ineffectual at elevated temperatures, where recrystallization nullifies the beneficial effects of deformation strengthening.

The elements most commonly used for solid solution strengthening in commercial Nb alloys are W, Mo and Ta. These elements are combined at concentrations of 1-5% for Mo and at levels of 10-30% for W and Ta. These elements have a wide solubility limit in Nb and aid in increasing both the modulus and the yield strength without compromising the melting temperatures. Figure 1 illustrates the effect on melting point of different alloying elements. Note that Cr, Ti and V (all of which have been found to enhance the oxidation properties of pure Nb) lead to severe melting point depression and have been found to sharply reduce the creep resistance (Ref. 4). For enhanced high temperature mechanical properties, these elemental additions should be minimized or avoided.

Dispersion strengthening is not novel in niobium metallurgy, where both oxide and carbon dispersions have been introduced into strong Nb alloys. These dispersions coarsened at a rate too rapid for use at elevated temperatures for extended periods of time, and have been abandoned. A number of promising experiments have been conducted in which dispersions of nitrides and borides have shown high temperature stability. This program studied the feasibility of using these precipitates as dispersion strengthening agents in Nb alloys at elevated temperatures.

1.2 Creep Deformation

If we limit our discussion to dispersions which are impenetrable by dislocations, we find that a threshold stress to activate creep by local climb is given by Ref. 5 as

$$\tau_{lc} = \frac{\mu b}{2\pi\lambda}\ell n\left(\frac{\lambda}{r_o}\right) \tag{1}$$

where τ_{lc} is the shear stress required to initiate local climb, μ is the shear modulus, b the Burger's vector, λ the interparticle spacing and r_o the dislocation core radius. This model is limited to volume fractions of precipitates less than 12% where local climb of dislocations around precipitates can be modeled as separate events. By substituting the following equa-

3

tion which relates the particle size and volume fraction to the interparticle spacing for a random distribution (Ref. 5)

$$\lambda = a\,(f^{-1/3} - 1) \tag{2}$$

where a is the particle radius, one immediately sees that the dependence of threshold stress on precipitate volume fraction becomes

$$\tau_{lc} = af^{1/3}\,\ell n(f) \tag{3}$$

for constant particle size. Equation (3) is again limited to low volume fractions. Thus precipitate volume fraction will directly affect the threshold creep stress. In addition, the particle spacing must be sufficiently low to maximize the threshold stress, which as shown in Eq. (1) is proportional to the Orowan bowing stress by

$$\tau_{ob} = \frac{\mu b}{\sqrt{8\pi\lambda}}\,\ell n\frac{\lambda}{r_o} \tag{4a}$$

or

$$\tau_{lc} = \sqrt{2}\,\tau_{ob} \tag{4b}$$

where τ_{ob} is the shear stress required to loop a particle by the Orowan process. By substituting Eqs. (2) and (4a) into (4b) one sees that

$$\tau_{lc} = a^{-1}\,\ell n(a) \tag{5}$$

Here, the former term dominates the latter, resulting in τ_{lc} decreasing with increasing a to the limit where the particles are cut by the dislocations. To this point, the practical lower limit to the particle size is governed by the lack of stability of very small particles to coarsening due to their inherently high chemical activity at elevated temperatures. This must be determined separately for each dispersion strengthened system since both coarsening rates and precipitate strengths will vary widely.

Using data for Nb in the above equations, a plot of τ_{lc} vs particle radius can be generated for a number of particle volume fractions. This is given in Fig. 2 for particles ranging in size

4

from 0.1 nm (1Å) to 1 mm, and for dispersion volume fractions from 0.005 through 0.1. One sees that for particulate volume fractions of 5%, a maximum critical shear stress of over 1000 MPa can be achieved at a particle size of 1 nm. If we arbitrarily pick a minimum shear stress of 100 MPa, one notes that an average particle size of 10 nm will result in no creep deformation for 0.5% precipitate volume fraction. Increasing the volume fraction by a factor of twenty results in τ_{lc} increases of only a factor of three, a second order effect. However, this type of analysis does show that a fine dispersion of nonshearable particles can lead to creep resistant alloys.

When the applied shear stress is greater than τ_{ob}, creeping dislocations will either bypass the particles by climbing over them as occurs at stresses lower than τ_{ob} (Ref. 6) where the minimum creep rate is given as

$$\dot{\epsilon}_m = \frac{\pi b^3 D}{2RT} \frac{\sigma}{a^2} \tag{6}$$

or bow in between them when the applied stress exceeds the Orowan stress (Ref. 7) and is given as

$$\dot{\epsilon}_m = \frac{2\pi D}{2RT} \frac{\sigma^4 \lambda^2}{\mu^3 a} \tag{7}$$

Empirically, this has not been found to be an adequate representation of creep in dispersion strengthened metals. The empirical formula typically used to model creep data is given as

$$\dot{\epsilon}_m = K \frac{(\sigma - \sigma_b)^n}{e} \exp\left(\frac{-Q}{RT}\right) \tag{8}$$

where σ_b is the back stress, Q_c is the activation energy for creep and K and n are empirically derived constants. Inclusion of the back stress term (Ref. 8) was found necessary so as to bring the n and Q_c terms into approximate agreement with values found for pure metals.

1.3 Precipitation in Nb Alloys

High temperature strengthening of metals can be obtained through precipitation hardening. For a dispersion of precipitates to be useful as a high temperature strengthening agent, it must be stable at its use temperature, be of sufficient size so as to present non–shearable

obstacles to dislocation motion and be of sufficient volume fraction so as to diminish Orowan looping. First, for a precipitate to have maximum stability at high temperatures, it must conform to one of the following criteria. It must have low surface energy with the matrix, or be composed of components of which one must have low solubility in the matrix. Examples of these two types of precipitate strengthening, which defy one of the above-mentioned rules, but which are still useful, are given below. Ni-base superalloys, having the coherent γ' precipitate with a very low interfacial energy, are used extensively up to 1093 °C (2000 °F); despite the high solubility and rapid diffusivity of Al in the Ni matrix, rapid particle coarsening does not occur. Another alloy system of considerable high temperature strength is TD nickel where the thorium in the incoherent thoria particles maintains a very low solubility and diffusivity in the nickel matrix leading to precipitates which resist coarsening after extended exposure at high temperatures, despite a matrix-particle surface energy which is very high due to its incoherent nature. Thus, precipitation strengthened systems can be utilized if one of the above cited stabilizing mechanisms overrides the other.

Particle coarsening can usually be modeled by the equation:

$$r_o^3 - r^3 = \frac{8V^2\gamma C_i D}{9RT}\, t = kt \tag{9}$$

where r and r_o are the particle radius at time t and initially, V is the molar volume of the precipitate, γ is the particle/matrix surface energy, C_i is the concentration, D is the diffusion coefficient of the rate limiting constituent and k is short-hand notation for the constant term. The interfacial energy, γ, is not expected to vary by more than one order of magnitude as shown in Ref. 9, where a compilation of interfacial energies is given for a number of coherent and incoherent precipitate system. The molar volume, V, will likewise vary only slightly from one compound to another. Thus, the diffusion rate of the dispersion's constituents along with their solubility can be used to determine candidate dispersoids.

The solubility of a dispersion in an alloy matrix will be proportional to its free energy of formation, $- \Delta G$. Low solubility precipitates can be found by limiting the search to very stable particles at temperatures in excess of 1400 °C. A reasonably complete listing of free energies of formation for metallurgically important compounds is given in Ref. 10. For a compound to be considered stable in a Nb alloy, it must have a free energy less than its Nb counterpart, in addition to being low in its own right (i.e. < -100 kJ/mole). The free energies for candidate dispersions are given in Table II.

TABLE II – FREE ENERGIES OF FORMATION FOR CANDIDATE-DISPERSIONS

Compound	$-\Delta G_{1500}$(kJ/mole compound)	$-\Delta G_{1500}$(kJ/mole solute)
NbN	***	–
Si_3N_4	251	63
TiN	195	195
ZrN	223	223
NbB_2	235	118
CeB_6	313	52
HfB_2	316	158
TiB_2	303	152
ZrB_2	302	151
Nb_2C	***	–
ZrC	184	184
$NbSi_2$	131	65
Ta_5Si_3	361	120
Mo_5Si_3	323	108
NbO_2	518	259
Ta_2O_5	1413	283
Ti_3O_5	1797	359
Y_2O_5	1482	296
SiO_2	640	320

Diffusivities of elements in pure Nb have also been compiled for those experiments using the tracer method in Ref. 11. Table III gives a number of commonly used Nb alloying elements with their frequency factor, D_o, activation energy, Q, and diffusivity at 1400°C. It is interesting to note that at this temperature Ta has a much higher diffusivity than Mo while both C and Y maintain reasonably low diffusivities. It should be remembered that these data are limited to tracer diffusion studies and do not include diffusivity data gained by other means.

7

TABLE III – TRACER DIFFUSION DATA IN PURE NIOBIUM

Element	D_0 (cm^2/sec)	Q (kcal/mole)	$D_{1500°C}$(cm^2/sec)
Ti	0.40	88.5	0.039
Zr	0.47	87.0	0.460
Ta	1.00	99.3	0.970
Y	1.5×10^{-3}	55.6	0.001
C	3.3×10^{-2}	37.9	0.033

In view of the fact that diffusivity data are incomplete, precipitate stability was judged primarily on free energy arguments. Thus, the selected aim dispersions are given in Table II. In general, the borides look very promising as candidate dispersions as do the silicides; both B and Si have low solubilities in Nb from binary phase diagrams.

The most stable compounds listed here by far are the oxides of Ti, Ta and Y. Oxide dispersion strengthening of Nb alloys has been investigated in the past with the conclusion that particle coarsening rates were excessively high for their applicability as high temperature dislocation barriers as described previously. The oxides previously examined were those of Zr and Hf while additions of Ti and Ta most assuredly deoxidized the alloys additionally. The free energies of ZrO_2 and HfO_2 are −409 and −414 kJ/mole at 1500°C, respectively. These are low free energies (in terms of absolute value) with respect to the borides and nitrides, but the high diffusivity of oxygen and the metal atoms would appear to supersede the thermodynamic stability.

Carbides of Zr and Hf have been studied to the greatest extent in Nb alloys. The − ΔG for ZrC at 1500°C is seen to be the highest one given in Table I. This gives some indication as to the reason for the carbide's lack of thermal stability.

It is clear from the above discussion that a stable dispersion is needed to impart high temperature creep strength, and that the dispersions previously suggested thus far are not stable at the temperatures of probable application of these alloys. A number of recent Russian articles have shown that dispersions of nitrides or borides in a Nb matrix impart significant high temperature strength after extended exposure at these temperatures. The ZrN and HfN dispersions, in particular, show exceptional properties that would make them useful in high temperature applications.

A comparison of the ultimate tensile strength of a number of dispersion strengthened alloys is given in Fig. 3 (Ref. 4) with the Ni alloy D.S. Mar M–200 above 1200°C; the M(IV) nitride and carbide dispersions impart greater strength than oxides, and the nitrides comparably strengthened the alloy at lower volume fractions.

Furthermore, it has been shown that these nitride dispersions can be modified by high temperature heat treatments as given in Fig. 4 (Ref. 12). An anneal at 1800°C (3272°F) is seen to substantially increase both the yield and ultimate strengths of Nb. Aging at 1000°C (1832°F) after a high temperature anneal leads to further increase in yield strength. We have concluded from these preliminary experiments that the ZrN precipitates are heat treatable to some extent. Microscopic evidence for HfN dissolution in Nb has been shown (Ref. 13). After annealing at 1800°C (3272°F), precipitates 0.7 μm in size were observed while an age of 700°C (1292°F) yielded precipitates of 1.8 μm From this evidence it was concluded that the large precipitates formed on casting are completely solutioned at 1800°C (3272°F) and re-precipitate on slow cooling to a finer size.

The pseudo–binary phase diagram for the Nb–ZrN system has been identified for Zr:N = 1.0 and is given in Fig. 5 (Ref. 14). This diagram is instrumental in determining the amount of Zr and N which needs to be added to the Nb alloy in order to obtain the required precipitate dispersion. The top axis shows for instance the volume fraction of precipitates which would be expected for a given atom fraction of Zr and N, and also the homogenization temperature required. In this instance, a maximum volume fraction of 4.2% ZrN can be achieved with the possibility of solutioning the precipitates completely.

This complete solubility allows for a wide degree of latitude in tailoring microstructures to necessary property requirements if the precipitates do not significantly coarsen at the use temperature. For instance, single crystals of dispersion strengthened Nb alloys can be grown and subsequently heat treated if the nitrides are in solution just below the melting point of the alloy. On the other hand, rapid solidification techniques can be used to form a supersaturated solution of Nb, Zr and N after which consolidation and heat treatment can precipitate a fine dispersion of ZrN at lower temperatures as is being successfully utilized in Ti alloys (Ref. 15).
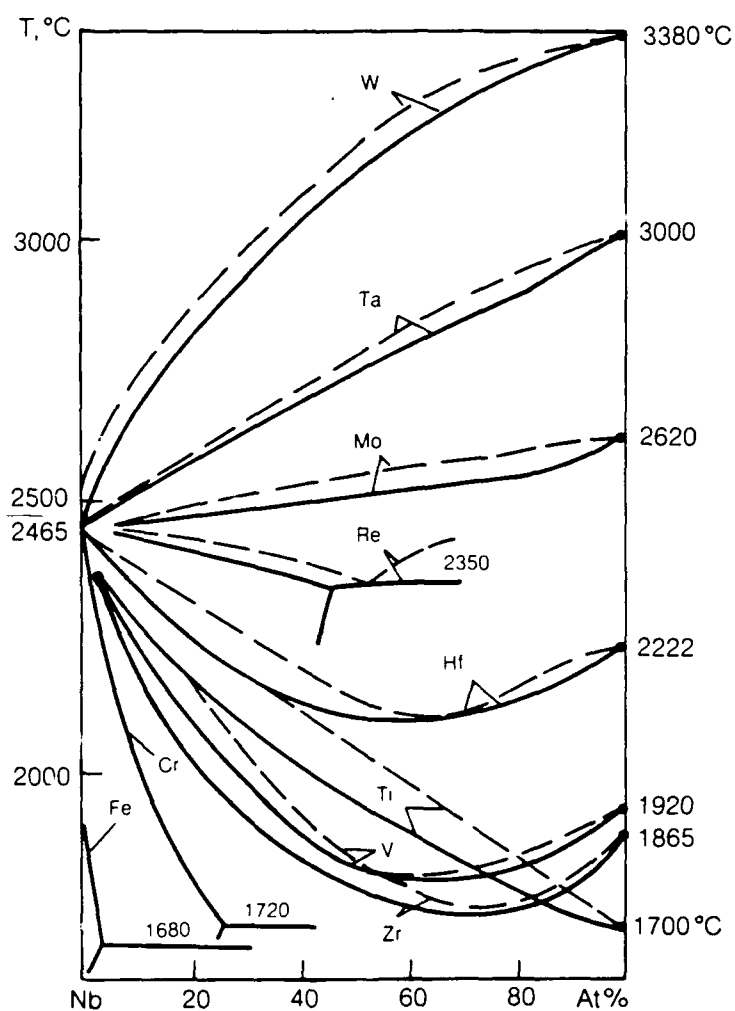
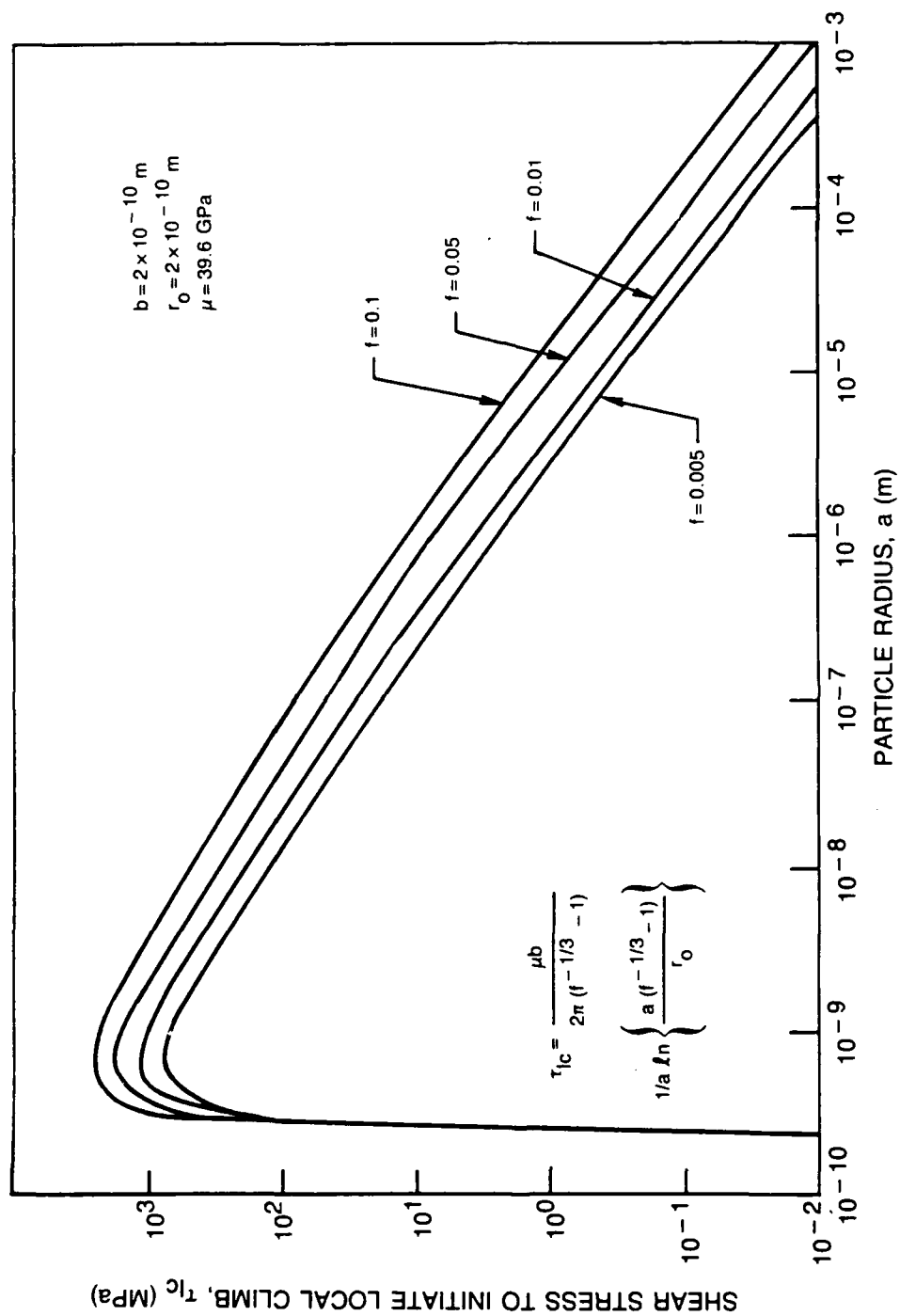Figure 1. Effect of Alloying Elements on the Melting Point of Niobium

Figure 2. Shear Stress Required for Local Climb as a Function of Precipitate Size and Volume Fraction
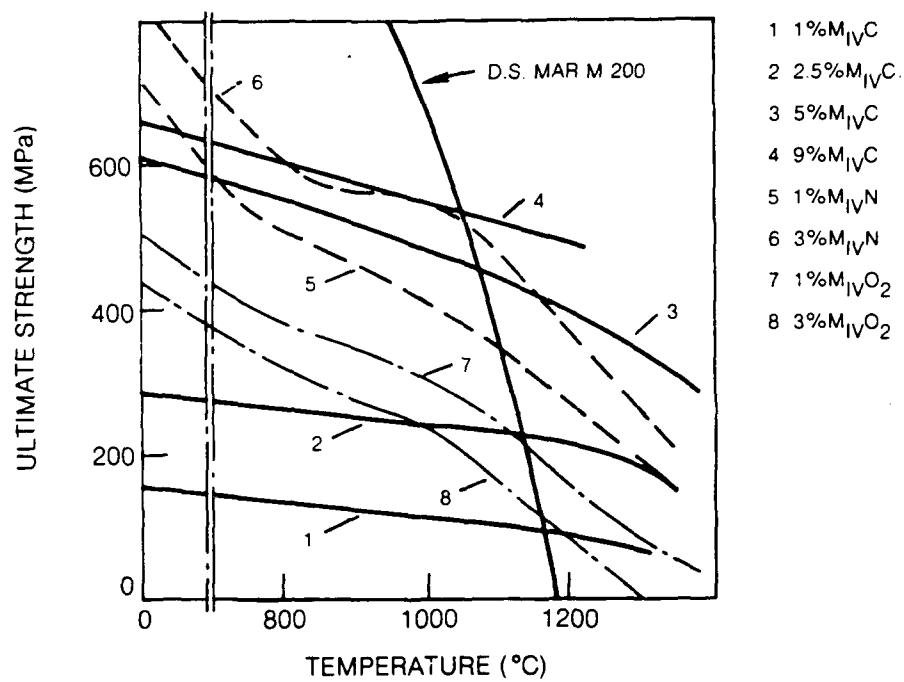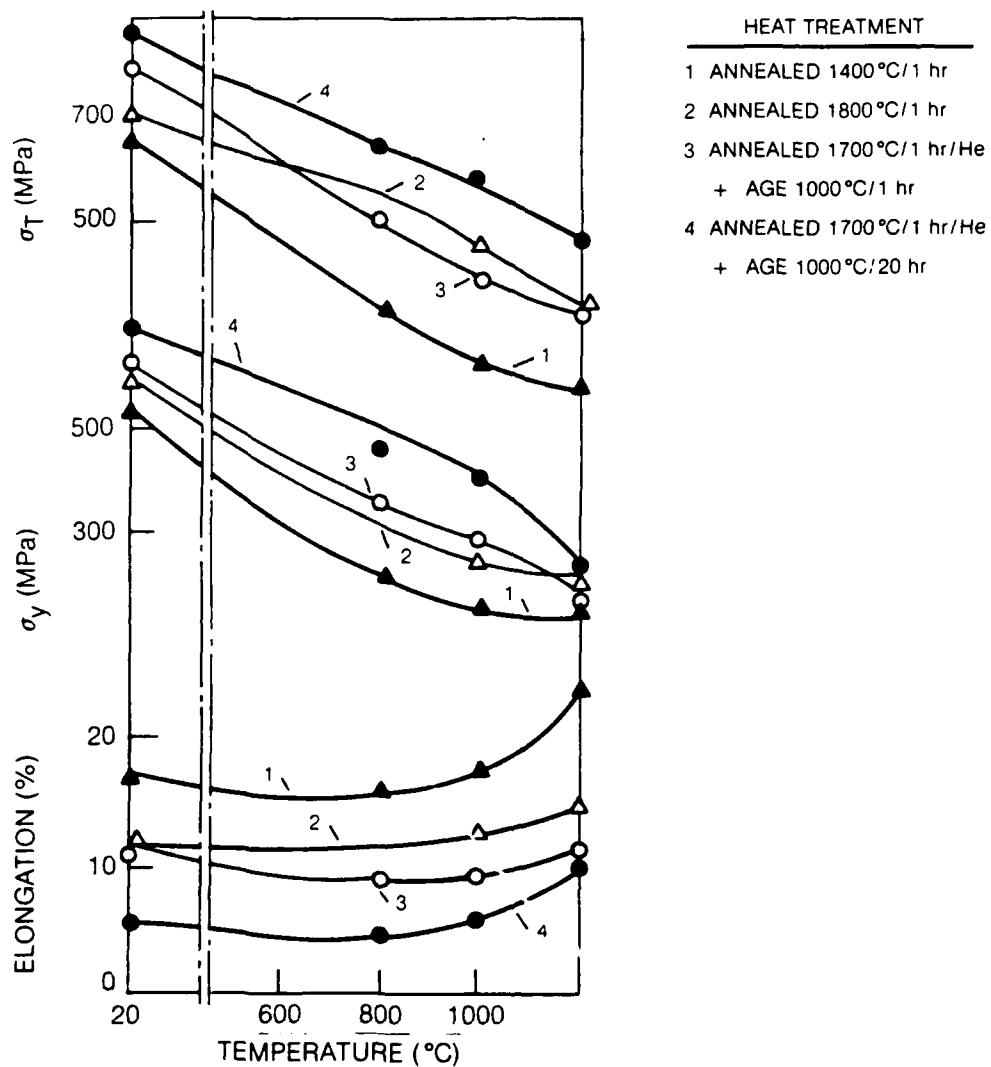
Figure 3. Dispersion Strengthened Nb Alloys
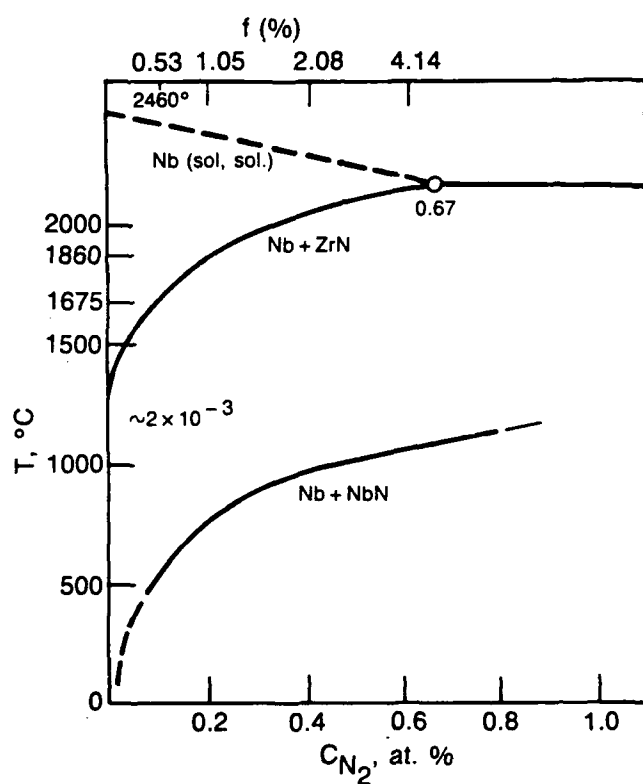
Figure 4. 2% ZrN Dispersion Strengthened Nb Alloys

HEAT TREATMENT

1 ANNEALED 1400°C/1 hr
2 ANNEALED 1800°C/1 hr
3 ANNEALED 1700°C/1 hr/He
   + AGE 1000°C/1 hr
4 ANNEALED 1700°C/1 hr/He
   + AGE 1000°C/20 hr

13

(REF. 11)

Figure 5.   Pseudo-Binary Phase Diagram for Nb-ZrN System with Zr:N = 1

14

2.0 EXPERIMENTAL PROCEDURES

2.1 Alloying and Rapid Solidification

Alloys were prepared using commercial purity starting elements by an arc casting technique. This was accomplished using an argon atmosphere gettered with Ti and continuously monitored as having an oxygen partial pressure less than 10^{-6} ppm using a calcium stabilized zirconia fast ion conducting cell where the ionic conductivity is continuously monitored and is a function of oxygen partial pressure. Nitrogen was added in the form of NbN powder. Alloys were fabricated so as to introduce 2 volume percent of the dispersions given in Table I, assuming 100% precipitation, with the inclusion of a pure Nb splat for comparison. Interstitial impurities were monitored using the gas–fusion technique.

Rapid solidification was accomplished by arc melting small buttons on a polished water cooled copper hearth, and impacting the molten alloy with a polished water cooled copper hammer which was pneumatically driven. This technique produced "splats" which have uniform thickness over a circular area of 2.8 cm^2. By changing the hammer velocity and other configurational parameters, splat thickness could be controlled. Typically, splat thicknesses of 0.013 to 0.018 cm (5 to 7 mils) were produced.

2.2 Heat Treatment and Age Hardening

The alloy splats were subsequently cut into sections and wrapped in Nb foil and heat treated in Ti gettered He with an analyzed purity of $< 10^{-7}$ ppm oxygen. Two heat treatment plans were utilized; the first being a solution at 2200°C for 4 hours followed by iterative 1600°C heat treatments for .5, 1, 2, 4, 8 and 16 hours, with the other consisting of a low temperature precipitation of 1200°C for 4 hr with iterative 1400°C heat treatments for the durations stated previously. After each of the iterative heat treatments, one specimen was removed from the furnace and mounted edge on for metallographic and hardness evaluation. Following metallographic preparation, a minimum of fifteen Vickers hardness indents at a 100 g load were made into each specimen across their thickness so as to average any chemical gradient or cooling rate effects. The outside edge of the hardness indent was not allowed to come so close to the splat surface as to allow visible buckling and any data points from this near surface region which deviated greatly from the other readings were disregarded and another measurement taken. A typical indent pattern is given in Fig. 6. An optical microscopic examination followed to characterize the grain morphology and any large precipitation which had occurred.

2.3 Analytical Electron Microscopy

This means of specimen preparation (splat quenching) is ideal for the preparation of TEM thin foil specimens. Disks are simply punched out of the splat material and jet thinned

using a South Bay Jet Polisher. This is a completely plastic and stainless steel system which allows for the rapid and automatic jet thinning of Nb alloys using hydrofluoric acid. A solution based on that reported in Ref. 16 consisting of 500 ml methyl alcohol, 100 ml ethylene glycol monobutyl ether (butyl cellusolve), 90 ml H_2SO_4 (98%), and 30 ml HF (50%), was used with good results. The polishing conditions were 50 VDC, 80 ± 10 mA, and –60 ± 15°C electrolyte temperature. Each side of a disc was polished separately for ≃25 minutes. Occasionally, ion thinning was used to finally prepare previously thinned specimens.

2.4 Mechanical Testing

"Dog bone" tensile specimens were electro–discharge machined, EDM, from the splatted alloys to be evaluated. The test specimens were the thickness of the splats, typically 180 μm (0.007"). The gauge lengths were 1.0 cm and the radii of the gage blends was 1.27 cm. Two test specimens were obtained from each splat. After specimen fabrication, four test specimens were placed between two Nb sheets supported between two alumina discs and a load of 167g was applied. A heat treatment cycle of 1200°C/4 hr was given to the specimens under an atmosphere of purified He. This heat treatment served to precipitate out a fine dispersion and concurrently stress relieve and flatten the test specimens.

Tensile testing was conducted under purified argon in an all metal testing facility with temperature capability of 2000°C. Two test types were conducted, tensile and strain rte sensitivity. Tensile tests were conducted at 1400°C at a strain rate of ≃ 0.0003 sec^{-1}. Strain was monitored by a strain gage on the grips while load was measured by a 2000 lb load cell, with measurements recorded by an x–y recorder. The strain rate sensitivity tests were carried out on two specimens of each alloy chemistry. Starting at the initial strain rate, $\dot{\epsilon}$ was 0.001 (all in sec^{-1}) and was incremented through the following sequence, 0.0004, 0.00015, 0.001, 0.00015 or until specimen failure occurred. The second specimen was tested in ascending strain rate starting at 0.001 and continuing to 0.0035, 0.007, 0.001, 0.007 or until specimen failure. Again, stress and strain measurements were recorded via an x–y recorder.

50 μm

Figure 6. Typical Vickers Hardness Indent Pattern in Alloy H87-12C After 1 hr
Age at 1600°C

3.0 RESULTS AND DISCUSSION

3.1 Interstitial Concentrations

Contamination of Nb alloys with oxygen has been shown to cause wide variations in mechanical testing results (Ref. 1). It is of interest to know and understand the oxygen concentration of these alloys at all steps during specimen fabrication so that oxygen concentrations can be controlled. In addition, control of nitrogen concentration is also necessary since many of the dispersions which are planned are nitrides.

A sample of the commercial purity Nb used in all of the testing reported here was analyzed. The results are as follows: oxygen 620 ppm by wt (0.33 at%), nitrogen 110 ppm by wt (0.07 at%), and carbon 60 ppm by wt (0.03 at%).

Table IV reviews the experimental results gained from these chemical analyses. The first four tests were conducted so as to determine the amount of nitrogen retention in a niobium alloy during arc melting using the procedures described previously. Both pure Nb and a Nb alloy were arc melted in gettered Ar and an Ar–80% N atmosphere. Analysis for nitrogen shows that in the mixed atmosphere, up to 14.3 at% (2.4 wt%) N was dissolved in the two alloys. This is the equilibrium amount as determined by Ref. 17. The commercial purity Nb after arc melting in Ar had a nitrogen concentration of 0.12 at% (180 ppm by wt), typical for commercial grade Nb. An alloy with 0.1 at% N added by use of Nb_2N powder maintained 0.13 at% N (200 ppm N by wt). Nitrogen additions through the use of NbN powder in a pure Ar atmosphere was then concluded to be adequate for N alloy additions.

Oxygen dissolution during arc melting and splat quenching and subsequent heat treatments was monitored by heat treating splat quenched alloys at elevated temperatures as summarized in Table IV. After heat treatment of a Mo–Ta–Si containing Nb alloy at 1500°C (2372°F) in a 10^{-6} vacuum, an oxygen level of 2.12 at% (3700 ppm by wt) was measured. The criticality of oxygen concentration can be measured by its effect on the DBTT as shown in Fig. 7 (Ref. 18). For the DBTT to be well below ambient, an arbitrary temperature of –130°C (–200°F) may be chosen as critical thus yielding a critical oxygen concentration of 0.36 at% (600 ppm by wt). One must also keep in mind that only dissolved oxygen has the effect of increasing the DBTT and that oxygen tied up as oxides will not be detrimental. Thus the actual allowable oxygen concentration in the presence of strong oxide formers such as Zr may be considerably higher. The oxygen concentration must be kept in the hundreds of ppm range, which was surely not maintained in the 10^{-6} torr vacuum. A previous study (Ref. 19) has shown that vacuum of 10^{-9} is necessary for the long term exposure of Nb where it is necessary to minimize oxygen concentration.

TABLE IV – GAS FUSION ANALYSIS EXPERIMENTS
(All In Wt% Unless Otherwise Specified)

1. Nb button in Ar
   0.018% N (0.12 at%)

2. Nb button in 20 Ar–80N
   2.46% N (14.33 at %)

3. Nb–Mo–Zr–N button in Ar
   0.02% N (0.13 at% vs aim 0.1 at%)

4. Nb–Mo–Zr–N button in 20Ar–80N

5. Nb–Mo–Ta–Si splat
   1500°C/4hr/vac
   0.37% O (2.12 at%)

6. Nb splat
   1500°C/4hr/g Ar–Ta env.–flowing Ar
   0.099% O (990 ppm–0.57 at%)

7. Nb splat
   1500°C/4hr/g Ar–Ta env.–dead Ar
   0.13% O (1300 ppm–0.75 at%)

8. Nb splat
   1400°C/4hr/g Ar–21 Ti + Ta env.–dead Ar
   0.0073% O (73 ppm–0.04 at%)
   0.0107% N (107 ppm–0.07 at%)

Splats of commercial purity Nb were heat treated as described in Table IV. After wrapping in Ta foil, and heating to 1500°C (2732°F) for 4 hrs, the oxygen concentration was reduced to 0.57 at% (990 ppm by wt), a great improvement over the previously cited case. By prewrapping the splat specimen in 2 Ti envelopes and a Ta layer, the oxygen concentration was further reduced to 0.04 at% (73 ppm by wt) while maintaining the nitrogen content at 0.07 at% (107ppm by wt) the starting nitrogen concentration. This last procedure worked very well in reducing the oxygen concentration during extended heat treatments and was used hereafter for heat treatments below 1500°C. The Ti foil wraps were replaced by Hf foil for heat treatments above this temperature.

3.2 Age Hardening Model

One can correlate hardness data to precipitate size through the following argument. One

assumes that hardness, H, is proportional to the yield strength, σ_y (Ref. 20), such that:

$$H \propto \sigma_y \tag{10}$$

The theoretical correlation between dispersoid particle size and σ_y was developed by Hirsch and Humphreys (Ref. 20) as being:

$$\tau_c = \frac{(0.4Gb)}{\pi \ L} \quad \frac{\ell n(r/b)}{(1-v)^{.5}} \tag{11}$$

where τ_c is the critical resolved shear stress, L the interparticle spacing which can be further written as $[(\pi/f)^{.5} - 2] \cdot r$ with f the precipitate volume fraction volume fraction, G the shear modulus, r the particle radius and v Poisson's ratio. For our analysis, σ_y can replace τ_c and the following notational simplifications made;

$$B = \ell n(2/b) \tag{12a}$$

$$A = \frac{(0.4Gb)}{\pi(1-v)^{.5}[(\pi/f)^{.5} - 2]} \tag{12b}$$

therefore:

$$H \propto Ar^{-1} \ [B + \ell n(r)] \tag{13}$$

By combining eqs. 13 and 9 we obtain;

$$H \propto A \ (r_o + kt)^{-1/3} \ [B + \ell n\{(r_o + kt)^{1/3}\}] \tag{14}$$

and by neglecting for the moment the hardening of the alloy with particle size and concentrating on the over-aging, the following simplification of eq. 14 can be shown;

$$H \propto AB(r_o^3 + kt)^{-1/3} \tag{15}$$

From this point it is clear that for small r_o (as would be the case in rapidly solidified alloys), by plotting $\ell n \ (H)$ vs $\ell n \ (t)$ one should obtain a straight line plot having a $-1/3$ slope. The actual measured slope of this line shall be defined as the unitless softening coefficient, Ψ, and given

as:

$$\Psi = -\,(d\ell n[H]/d\ell n[t]) \tag{16}$$

Two typical isothermal age hardening plots subsequent to the 1200°C precipitation heat treatment are shown in Fig. 8 for the alloys containing ZrC and Ta_5Si_3 respectively. The former shows classical age hardening response with hardening followed by softening due to over–aging. In the latter case very little hardening or only softening was observed, probably due to precipitate growth either during the lower temperature age or because of particle precipitation during rapid solidification.

By plotting these two curves as $\ell n(VHN)$ vs $\ell n(t)$ as described above, one sees in Fig. 9 that straight line plots are indeed obtained for the age softening portions of the curves. The slopes, as determined by a least squares analysis, were Ψ = –0.130 and –0.065 respectively. While these coarsening coefficients are considerably lower than the –0.333 theoretically expected, this value of Ψ can be used to categorize precipitation phenomena as to their utility at elevated temperature since it measures the change in hardness (i.e., strength) with time at temperature. This analysis is also useful since solid solution effects, which do not chai ge with time, are not measured. Close examination of the mathematical argument presented above shows that if an exponential term is present in eq. 10, this would translate to a product of this term times Ψ. The assumptions made above may be in minor error, affecting this term. It will be assumed that if the coarsening exponent is low, that is the alloy over–ages at a slow rate, that the rate limiting step in particle coarsening is slow and the dispersoid may be suitable as a high temperature dispersoid. Conversely, if the material softens rapidly, any dispersoid present acting as a barrier to dislocation motion may be rapidly coarsening, thereby lowering strength.

There are a number of hazards one must guard against in this analysis. For instance, in the event no precipitates are formed, no hardening or softening due to precipitate mechanisms can occur. Thus, the over–aging slope, Ψ, will be nil and one may inadvertently assume a very stable precipitate is present. A measurable coarsening of the particles, by age softening as monitored through DPH testing, is a prerequisite.

Additionally, some single phase effect will also lead to age softening such as grain growth, oxygen depletion or vacancy annihilation. In order to minimize some of these effects it was found helpful to pre–age the specimens at 1200°C for 4 hours. This brings the rapidly solidified material into a stress relieved state along with precipitating the dispersed phase into a fine dispersion. To monitor grain growth, which will also be a function of the precipitate process and grain boundary pinning, a pure niobium splat quenched alloy was prepared and aged as noted previously.

3.3 Aging Results

Table V gives the age softening data of the pure Nb and alloyed splat quenched material given the two heat treatments noted in the previous section. In addition to the calculated lin-

ear regression data of slope and intercept, the quartile ranking of the 1400°C aged alloys is also given. This ranking will be used to identify candidate dispersions for further microscopic and mechanical test evaluation. Optical examinations were conducted on splat cross sections and the qualitative results are summarized in Table V.

The pure Nb metal is seen to definitely have an age softening character with a unitless softening rate constant of -0.019. Optical metallography reveals that grains grew rapidly upon aging which could be one source of the age softening. In addition it was shown in Ref. 1 that aging in very pure gas results in deoxidation of the splat material. By lowering the dissolved oxygen concentration the interstitial hardening is diminishing with exposure time. In alloys which tie up the oxygen as oxides, the alloys are to a large extent deoxidized and this effect should be minimized. Considering this as a base-line, any alloys with a significantly lower softening rate constant will be considered to have unmeasurable precipitate coarsening by this technique.

The 1600°C aged alloys displayed either very low or very high age softening rates. The very low softening rate constants, $\cong 0.005$, which are seen in the carbide containing alloys are indicative of minimal over-aging due to either totally over-aged precipitates or possibly solutioned precipitates. This is consistent with previous findings that carbides are not significant dislocation barriers at high temperatures. The high softening rate constants of 0.156 and 0.050 were observed in nitride containing alloys, while the boride containing alloys maintained moderate rate constants of $\cong 0.030$. Additionally, all of the grain structures after this heat treatment were equiaxed vs. the initial columnar grained splats, indicating that extensive grain growth has occurred. The borides and nitrides still display properties which make them desirable as high temperature dislocation barriers.

The 1600°C exposure has proved to be too severe. Possible candidate precipitates either coarsen too rapidly, are over-aged during the 2000°C "solutioning" treatment or go into solution. Thus a lower heat treatment was devised. An age at 1200°C is expected to precipitate particles from the rapidly quenched metastable solid solution into a fine evenly distributed dispersion. Further aging at 1400°C will serve as the test temperature.

The softening rate constants at 1400°C varied from 0.014 for SiO_2 as a possible precipitate to 0.131 for ZrC. This was considered an ideal distribution from which candidate dispersions could be selected. These dispersions were ranked into quartiles according to softening rate. Two alloy additions, Y and Ti/N, displayed atypical behavior and could not be readily ranked and were put into the fourth quartile. These alloys will be briefly discussed later.

The alloys with the greatest softening rate constants, in the third quartile, contained carbides of Hf and Zr, the carbide resulting from the commercial alloy containing Ta, Zr and C and the nitrogen only alloy. It was not surprising to find the carbides in this quartile since their high temperature stability is known to be insufficient. Additionally, the free energy, $-\Delta G$, of ZrC is the highest of those tested here (see Table II), giving experimental validation to the precipitate stability argument set forth previously.

TABLE V – CANDIDATE DISPERSOIDS AND AGE HARDENING RESULTS

Alloy Number	Alloy Aim Composition	$-d\ln(H)$ Ppt.	Quartile $d\ln(t)$	Int.	Aging	Aging Temperature	Grain Morphology	Precipitation
H87-12A	Pure Nb	---	0.019		2.081	1400	Equiaxed	None
-12B	Mo-Zr-N	ZrN	0.156		2.530	1600	Columnar	None
	Zr-N	ZrN	0.050		2.072	1600	Equiaxed	Very Large
			0.057		2.143			
-12C	Zr-B	ZrB_2	0.012		2.348	1600	Equiaxed	Prior G. B. Ppt.
-12D	Hf-B	HfB_2	0.030		2.161	1600	Equiaxed	Very Large
-24A	Zr-C	ZrC	0.004		2.123	1600	Bamboo	Acicular Ppt.
-24B	Hf-C	HfC	0.005		2.085	1600	Equiaxed	G. B. Ppt.
-12B	Zr-N	ZrN	0.024	2	2.309	1400	Columnar	G. B. Ppt.
-12C	Zr-B	ZrB_2	0.027	2	2.323	1400	Columnar	
-12D	Hf-B	HfB_2	0.018	1	2.039	1400	Columnar	
-22A	Mo-Ta-Zr-C	ZrC	0.034	3	2.465	1400	Columnar	G. B. Ppt.
-13A	Hf-N	HfN	0.023	2	2.354	1400	Columnar	
-23B	Ta-Si	Ta_5Si_3	0.065	3	2.313	1400	Columnar + Equiaxed	
-24A	Zr-C	ZrC	0.131	3	2.208	1400	Equiaxed	"mottled"
-24B	Hf-C	HfC	0.039	3	2.075	1400	Equiaxed	"mottled"
-24C	Ti-B	TiB_2	0.019	1	2.196	1400	Equiaxed	Very Large
-25A	Ti	Ti_3O_6	0.022	1	2.389	1400	Equiaxed	Small Ppt.
-25B	Si	SiO_2	0.014	1	2.386	1400	Columnar	Small Ppt.
-25C	N	NbN	0.097	3	2.372	1400	Columnar	G. B. Ppt.
H88-06	Si-N	Si_3N_4	0.032	2	2.500	1400	Columnar	Small Ppt.
-08	Ti-N	TiN	---	4	---	1400	Columnar	Small Ppt.
-09	Y	Y_2O_3	---	4	---	1400	Columnar	Small Ppt.

The age hardening curves of this group are typified by Figs. 8a and 8b, with rapid hardening followed by softening over an extended time. The grain structure as observed optically after an 8 hour exposure at 1400°C is equiaxed, further evidence of over-aged precipitates which did not pin the grain boundaries. An optical micrograph of one such alloy is given in Fig. 10 where the equiaxed grain structure is evident. In addition, many relatively small dispersoids can also be identified distributed throughout the matrix. However, any precipitates which can be optically identified are too large to be effective as dislocation barriers.

Those alloys composing the second quartile contained ZrB_2, HfN, and Si_3N_4. The two former alloys were originally proposed and are still under consideration while the latter dispersion was chosen based on the free energy arguments. Their softening coefficients, Ψ, ranged from 0.023 to 0.032 and the microstructure revealed columnar grain structure. This grain structure, remnant from the rapidly solidified state indicates grain boundary pinning by a dispersion. Indeed, grain boundary precipitates were observed for all of the alloys in this quartile and a representative micrograph is given in Fig. 11 from the Hf-N containing alloy. Figure 12 illustrates a typical age hardening curve of this group. Hardening occurred totally within the first half hour of aging at 1400°C with age softening resulting after further aging. The extended softening allowed good fitting of the data to the ℓn-ℓn model proposed. This fit is shown in Fig. 9b.

Those alloy compositions which fell into the first quartile were not as uniform as those in the preceding two groups. One hardening curve given in Fig. 13, for the Ti-B alloy, shows initial age hardening through two hours followed by softening with a slight hardness increase after 16 hours at temperature. The same response was obtained for both the Ti and Si containing alloys. Since both Ti and Si are very strong oxide formers, the inadvertent introduction of oxygen during the aging treatment may have caused further precipitation, beyond what was present upon rapid solidification. These three alloys were not heat treated simultaneously, and they were aged with other alloys which did not display this hardening at 16 hours. This eliminates the possibility of oxygen contamination during one heat treatment. The slight secondary hardening at 16 hours, the only data point for which this was observed, moderated the softening parameter in the regression analysis.

As shown in Table V, two of these alloys contained equiaxed grain structures with the Si containing alloy retaining the columnar grain structure and fine dispersions. Very large precipitates were observed in the Ti-B containing alloy but were not identified.

Those alloys ranked in the fourth quartile did not show classical age hardening response and little change in hardness above experimental error could be identified. The Ti-N containing alloy was much different than the other alloys in that a large hardness increase upon aging at 1400°C for 0.5 hours occurred, see Fig. 14. The Vickers hardness varied about the mean of approximately 275 by ±10 through the 16 hours of aging. Extensive electron microscopy will be shown of this system in the following section, but it is expected that a short range ordering

reaction has occurred on cooling from 1400°C which results in the high hardness at ambient temperatures.

The softening coefficients, Ψ, can be plotted as a function of free energy, $-\Delta G$, which is given in Fig. 15. The precipitates studied display a broad trend of decreasing softening coefficient with increasing $-\Delta G$, as would be predicted from the free energy arguments proposed. For precipitates with $-\Delta G$ greater than 150 kJ/mole of interstitial solute, the softening is less pronounced but observable. A power law curve fit was made on this data with the resulting equation:

$$\Psi = 2.45(-\Delta G)^{0.86} \tag{17}$$

3.4 Microstructural Investigations

3.4.1 Pure Nb Base Line

A micrograph of a typical splat is given in Fig. 16. This figure shows an evenly splatted area of approximately 3 square cm and a thickness of 0.15 mm (0.006 in.). This evenly splatted area is surrounded by metal which cooled from one side only. This occurs when not enough liquid is present locally to be squeezed in between the hammer and anvil.

A cross section of a typical Nb splat is given in Fig. 17. During the rapid solidification, nucleation occurs simultaneously at the hammer and anvil surface and continues inward until the liquid is totally solidified at the centerline of the splat. This explains the columnar nature of the grains. No porosity was seen at the splat centerline due to solidification shrinkage, probably due to the pressure exerted by the hammer. The average grain size observed in this micrograph is 15 μm. An x-ray determination of texture in the splat plane was carried out in order to determine if preferential grain growth occurred and competitive grain growth did not have a chance to begin in the short growth distances encountered here.

Tensile specimens were electro-discharge machined, EDM, from the splatted material. These specimens have a gage length of 0.8 cm and their grip sections extend into the unevenly quenched area of the slat. In this fashion, two tensile specimens can be taken from each splat and each will have a uniformly thin gage section.

3.4.2 Nb-8M0-0.1Hf-0.1N (at%)

A splat of a Nb-8Mo-0.1Hf-0.1N alloy was made and heat treated in vacuum at 1500°C (2732°F) for 4 hrs. Both an etched surface view and a cross sectional micrograph are given in Fig. 18. The grains are now seen to be equiaxed, indicative of a totally recrystallized alloy with a grain size of -25 μm. The precipitates shown in the cross-sectional view are considered to be oxides since it was shown that heat treatment in vacuum is insufficient to minimize oxygen pickup. In addition, the splats heat treated in this fashion were very brittle and could not withstand being bent back upon themselves.

3.4.3 Nb-8Mo-0.1Zr-0.1N (at%)

The Nb-Mo-Zr-N system was used extensively to develop experimental techniques and procedures. Molybdenum was added as a solid solution strengthener and because initial studies indicated an enhanced cyclic oxidation resistance with additions of up to 3 atomic percent (Ref. 23).

Figure 19 shows a typical bright field-dark field pair with the accompanying diffraction pattern for a Nb-8Mo-0.1Zr-0.1N alloy which was heat treated at 1400°C for 1 hr. From Fig. 5, it is expected that a precipitate volume fraction of 0.5% should occur. The dark mottling is an artifact of the ion milling procedure used in final thinning and should not be confused with the larger precipitates which appear in the dark field image. In some instances, ion milling was found necessary to clean the jet thinned surface of an adherent residue.

The particles clearly visible in the dark field image are seen to be discrete and appear incoherent. They have an average diameter of 18.5 nm and are widely spaced although evenly distributed. From the resulting diffraction pattern, most nitrides and carbides having cubic structures can be ruled out (remembering the ZrN has the NaCl crystal structure).

In addition to the fine evenly dispersed intragranular precipitates, coarser grain boundary precipitates were observed, but not shown here. Preferential etching occurred in the grains adjacent to these grain boundary particles, thus making it difficult to analyze since many of the particles drop out of the specimen during the jet polishing procedure. Further analysis of these particles will be dealt with below.

The alloy described above was heat treated at 1400°C for 4 hrs with resulting microstructure given in Fig. 20. Here, both a bright field and its accompanying dark field images are given. The particles have grown substantially to 43.5 nm and now have rectangular cross sections in these micrographs.

A thin foil micrograph of a Nb-8Mo-0.6Zr-0.6N alloy in the splat quenched condition is given in Fig. 21. Since nitride particles were not identified after heat treatment at 1400°C, higher levels of both Zr and N were added in order to induce precipitation. From Fig. 5, the theoretical volume fraction of precipitates should be expected to be 4.1%. There are no precipitates visible in the grain interiors. However, a number of small particles are observed at the grain boundaries which have an approximate size of 48 nm. It is thus concluded that precipitation has been suppressed via rapid solidification.

The larger grain boundary precipitates mentioned above were also found in this alloy after heat treatment at 1400°C for 4 hrs. Selected area diffraction patterns have shown that these large grain boundary particles are identical in crystal structure to the finely dispersed particles mentioned earlier. As such, the large particles were examined closely to determine their structure and chemistry, thus giving us an indication of the nature of the fine dispersion. A representative image of one such particle is given in Fig. 22a. The preferential etching is

clearly visible with a particle having already fallen out to the right of the central precipitate. Both the large central particle (designated as P2) and that at the top of the micrograph (designated P3) were used for chemical and crystallographic evaluation.

The diffraction pattern given in Fig. 22b is that of P2 (not rotationally corrected). Crystallographic analysis shows this to have the monoclinic structure corresponding to ZrO_2 as illustrated in Table VI. Here the d spacings are those measured from the electron diffraction patterns and the "Mono ZrO_2" are those calculated from the lattice parameters given in Shunk (Ref. 24) for the various planes given in the right-hand column. From these match-ups, the zone axis of the particles as seen in the micrographs was determined and given in this table as $\overline{G}$. The comparisons showed excellent correlation giving an unambiguous determination of monoclinic ZrO_2.

TABLE VI – CRYSTALLOGRAPHIC ANALYSIS OF LARGE GRAIN BOUNDARY PARTICLES IN NB–8MO–0.1ZR–0.1N ALLOY

P2 $\overline{G}$ = [011]

d Spacing	Mono ZrO_2	Planes
5.075	5.08	100
3.71	3.69	011
3.16	3.16	$11\overline{1}$
2.85	2.84	111

P3 $\overline{G}$ = [$\overline{1}$11]

d Spacing	Mono ZrO_2	Planes
3.64	3.64	010
3.70	3.69	011
3.40	3.39	101

To further confirm this finding, an energy dispersive x-ray analysis was conducted on both particles mentioned above. Figure 23 presents the resulting spectra for P2. No nitrogen was present, while oxygen along with niobium and zirconium showed very high concentrations. This evidence agrees with the crystallographic findings above.

The absence of ZrN precipitates in these foils after heat treatment is a cause for concern. It has been reported in the literature (Ref. 25) that a volatile β –Mo_8N_3 phase can form and thus deplete the alloy of nitrogen. For this reason, molybdenum was removed from the alloys in the remaining experiments with the substitution with Ta or W for solid solution strengthening.

27

3.4.4 Nb-8Mo-0.1Hf-0.1B (at%)

An alloy containing Nb-8Mo-0.1Hf-0.1B was cast and splat quenched. A typical thin foil section is given in Fig. 24. This low magnification micrograph reveals a much different microstructure than was obtained in the nitrogen containing alloys. Large plates are clearly visible in the grain interiors. In addition, small grain boundary precipitates were also observed.

Stereo pairs of a similar splat quenched boron containing niobium alloy were made (Ref. 26), and it could be seen that these plates lay on (011) planes, the close packed plane in the BCC structure.

A typical grain boundary precipitate is shown in Fig. 25 under both bright and dark field conditions with the accompanying diffraction pattern showing the diffracted spot used for dark field. The precipitate which is highly faulted, has pinned the grain boundary. Analysis of the diffraction pattern is summarized in Table VII where d spacings are calculated from measurements taken from the diffraction patterns. "Ortho NbB" d spacings are those calculated from the crystallographic data given in Ref. 27 for orthorhombic NbB having lattice constants of a = 3.292, b = 8.713 and c = 3.165 Å followed by the appropriate plane. This analysis was conducted for a number of precipitates found both in the grain interiors and at boundaries, two of which are given in Table IV with the first from the diffraction pattern of Fig. 25c. An excellent correlation was obtained leaving little doubt that these particles are NbB. In addition, the particle diffraction spots are paired, indicative of twinning. Thus, the high degree of faulting obvious in Fig. 25 is most probably twinning.

TABLE VII – CRYSTALLOGRAPHIC ANALYSIS OF LARGE GRAIN BOUNDARY PARTICLES IN NB-8MO-0.1HF-0.1B

d Spacing	Ortho NbB	Planes
4.35	4.36	020
3.08	3.08	110
1.65	1.65	200
4.41	4.36	020
3.16	3.17	001
2.56	2.56	021
1.81	1.79	041

3.4.5 Nb-8Mo-0.1Zr-0.1B (at%)

Figure 26 is a micrograph of a Nb-8Mo-0.1Zr-0.1B alloy in the splat quenched condition. Again, the platelet phase is observed in the grain interiors as in the Hf and B containing

alloy described above. The many grain boundary perforations are indicative of preferential attack in the vicinity of precipitates. The diffraction pattern given in Fig. 26b shows diffuse spots in between the bright matrix spots. These diffuse spots are caused by short range ordering. This is the only alloy studied here to show short range order.

3.4.6 Nb-8Mo-0.1Ti-0.1B (at%)

The lattice parameter of the BCC matrix of splat quenched Nb-8.3Mo-0.05Ti-0.48NbB was determined from [001] selected area diffraction patterns (SADP's), using a thin foil specimen with a layer of gold sputtered onto its surface. This procedure yielded a lattice parameter of 3.295 ±.015 Å, which suggested that less than 8 at% Mo was present in solid solution after arc melting. Knowledge of this a_o made it possible to calibrate the camera constant of subsequent individual SADP's by using the matrix spot spacings.

Examination of the microstructure of Nb-8.3Mo-0.05Ti-0.48NbB in the as-splat-quenched condition revealed a strikingly geometric array of thin intragranular precipitates (Figs. 27-29). Figs. 27 and 28 are two-beam bright field images, $\bar{g}$ = [110] in the former case, and $\bar{g}$ = [002] in the latter. The direction of view is close to [100]. Most of the precipitates in dark contrast are thin plates of orthorhombic NbB; a_o = 0.3292 nm, b_o = 0.8713 nm, c_o = 0.3165 nm (Ref. 27). Both the diffraction patterns (Figs. 29b-30) and the observed orientations (Figs. 27-28) of the NbB indicated that three variants had precipitated, each with [010] NbB || {100} matrix.

Aging at 1200 or 1400°C resulted in the complete dissolution of the NbB precipitates observed in the splat quenched specimens.

3.4.7 Nb-1.2Ti-0.6N (at%)

As-splat-quenched specimens of this alloy were supersaturated; no precipitates were observed in the thin foil specimens. Specimens aged at 1200°C for 4 hours contained several types of precipitates; ranging from dark, blocky particles at both intergranular and intragranular sites, to thin rods with approximate diameters of 30-60 nm and lengths of 30-100 nm (Fig. 31).

The grain boundary precipitates (Fig. 32) were identified by selected area (Fig. 30) and convergent beam diffraction (CBED) to be hexagonal Nb_2N (Table VIII). In a few instances, the Nb_2N precipitates had coalesced along grain boundaries to form a continuous row (Figs. 34-35), but this was not commonly observed. The presence of kinematically forbidden 0001 reflections in the $< 11\bar{2}0 >$ CBED's (Fig. 35) is not unusual in compounds of this type (e.g. Cr_2N and AlN, Ref. 28).

TABLE VIII – OBSERVED VS CALCULATED LATTICE PARAMETERS, NB$_2$N PRECIPITATES <11$\bar{2}$0> ZONE AXIS PATTERNS

	Observed d's (nm)		
Plane	Fig. 20	Fig. 23	Calculated* d's (nm)
(0001)	0.500	0.495	0.496
(1$\bar{1}$00)	0.267	0.264	0.265
(1$\bar{1}$00)	0.236	0.233	0.234
(1$\bar{1}$01)	0.182		0.181
(1$\bar{1}$02)			

* a_o = 0.3058 nm; c_o = 0.4961 nm (Ref. 9)

The larger, dark intragranular precipitates shown in Figs. 31 and 36 were identified by selected area diffraction as the same phase which was observed at the grain boundaries: hexagonal Nb$_2$N. The short rows of multiple spots centered on each Nb$_2$N spot which are visible in Fig. 36c suggest the presence of stacking faults, or possibly twins.

The small, rod shaped precipitates which were randomly distributed throughout the grains (Fig. 31) were identified by crystallographic data to be TiN, first by using convergent beam diffraction to tilt the thin foil near a major precipitate zone axis, then by evaluating SADP's to obtain quantitative lattice plane spacing data (Fig. 37, Table IX). The relative orientations of the superimposed matrix and precipitate patterns suggests the following crystallographic relationship; {$\bar{1}$12} TiN || {$\bar{1}$12} Nb matrix and < $\bar{1}$1$\bar{1}$ >TiN || <110> Nb matrix.

TABLE IX – OBSERVED VS. CALCULATED LATTICE PARAMETERS TIN PRECIPITATE <11$\bar{2}$> ZONE AXIS PATTERNS

	Observed d's (nm)	
Plane	Fig. 24	Calculated* d's (nm)
(111)	0.244	0.244
(2$\bar{2}$0)	0.149	0.149
(3$\bar{1}$1)	0.126	0.126

* a_o = 0.4224 nm (Ref. 11)

3.4.8 Nb–0.2Zr–0.2B (at%)

Specimens aged for 1200°C/4hrs, then 1400°C/8hrs contained both inter–and intragranular precipitates (Figs. 38 and 39). The intergranular precipitates were determined by selected area diffraction and EDXS to be predominantly ZrO$_2$. Most of the intragranular pre-

cipitates were thin (< 50 nm) plates, which exhibited some evidence of coherency strain when image with $\bar{g}$ = <310> matrix (Fig. 40), but not with $\bar{g}$ = <110> (Fig. 39) or <200> (Fig. 41). They were identified by selected area diffraction (Figs. 42 and 43), Table X and EDXS (Fig. 44) as cubic ZrB.

TABLE X – OBSERVED VS. CALCULATED LATTICE PARAMETERS, Zr PRECIPITATES <011> ZONE AXIS PATTERN

Plane	Observed d's (nm) Figs 30B, 30C	Calculated* d's (nm)
(111)	0.266	0.248
(200)	0.232	0.232
(220)	0.164	0.164

3.4.9 Nb-0.6Hf-1.2N (at%)

The precipitate distribution in thin foils of the Nb–Hf–N alloy, aged sequentially at 1200°C/4 hrs and 1400°C/8hrs, was similar to that of aged Nb–Ti–N, save that the small, intragranular precipitates had a plate, rather than a rod, morphology. These were identified as cubic HfN (Fig. 45), based on analysis of SADP's in which the <001> zone axes of the matrix and the HfN were coincident (within this relplane, <110> matrix was parallel to <200> HfN). As in the case of the Nb–Ti–N alloy, the large intragranular precipitates (lower right, Fig. 46) were identified by diffraction pattern analysis to be Nb_2N. All of the grain boundary precipitates that were examined were monoclinic HfO_2 (Fig. 47).

3.4.10 Nb-1.2Hf-0.6C (at%)

Most of the intragranular precipitates in Nb–1.2Hf–0.6C, aged at 1200°C/4 hrs, were 100–400 nm plates (Fig. 48), identified by diffraction pattern analysis as cubic HfC (Fig. 49). A population of very small (< 30 nm) precipitates was also observed (Fig. 48), but not identified due to their size and low volume fraction.

3.5 Mechanical Test Evaluation

Room temperature tensile tests were conducted on pure Nb splats to verify the strength of this material and the testing technique. Figure 51 shows the dimensions of the miniature foil tensile specimens. The resulting data are as follows: E = 79.3 GPa (11.5 x 10^6 psi), σ_y = 281 MPa (40.8 ksi), σ_u = 340 MPa (49.3 ksi) and ϵ_f = 10.8%. This can be compared with E = 100 GPa (14.5 x 10^6 psi) (Ref. 29), σ_y = 250 MPa (36.3 x 10^6 psi) and ϵ_f = 50% (Ref. 30) for arc melted commercially pure Nb. The 20% drop in modulus cannot be readily explained by texture arguments as described previously, but it is expected that it may be due to specimen slippage. The yield strength is comparable and the best judge of the overall testing procedures.

The results of the elevated monotonic tensile testing are given in Table XI. As with the ambient temperature results, the moduli measured here at 1400°C are lower than those measurements reported in the literature. By extrapolation, the ultrasonic data of Laverty and Evans (Ref. 31) predicts a 1400°C modulus of 87.2 GPa as contrasted with an average of 8.68 GPa measured here. This discrepancy probably has a number of causes, the most important being time dependant changes, especially at these high temperatures. Extraordinary measures were taken to minimize slippage including spot welding of Pt foil to the specimens to act as a compliant layer for the grips to hold and the use of W screws with a lower modulus than the grip material Mo, thus utilizing the difference in thermal expansion. Typical of the stress strain curves generated for these alloys is that for alloy H87-24-C given in Fig. 51. The continuous drop in stress after the peak yield stress was common and is considered to be the result of stable plane stress crack growth which is common in thin foil specimens. The stresses thus obtained are considered to be lower bound values since crack propagation may have lead to lowered values.

The range of ultimate strength measurements were in much better agreement with previously published results than the modulus values. Figure 52 shows the range of tensile test results obtained here compared to results from Ref. 32. These results are confirmation of the validity of the mechanical test procedures used here. The data obtained is in the range between the electron beam melted pure Nb rod and rolled and annealed F48 sheet. With reference to the F48 alloy composition given in Table I, this is a high strength alloy with 20 at. % solid solution strengtheners (W and Mo) along with Hf and C for dispersion strengthening. The high level of solid solution strengthening will greatly enhance the tensile properties of this alloy while only marginally improving the creep properties, the main intent of this study. The majority of the strengthening of the alloys tested in this study must also be due to dispersion strengthening since it has been shown that (i) interstitial content is maintained at a very low level and (ii) the alloy additions introduced into the Nb are at a very low level (on the order of an atomic percent) and not expected to significantly strengthen pure Nb.

In comparing the strengths of these test specimens, one must take into account the failure location given in the last column. Where a "T" occurs, the failure initiated in the tab section of the specimen while a "G" indicates a gage section failure. Tab failure is indicative of premature failure due to gripping or a specimen flaw and the ultimate strengths generally reflect this with their low values. Because of this early failure, the strength of these specimens can always be expected to be higher than that reported. An analysis of ultimate strength vs failure strain was conducted to be certain that flaws introduced in the specimen gage sections during the EDM process did not bias the results. No trend in σ_m with ϵ_f was evident and in fact the higher strength alloys had ϵ_f's in the middle of those reported in Table XI.

The strongest alloys were those containing Ti-N, Si-N, Zr-B, Hf-B, Hf-N and the highly alloyed Mo-Ta-Zr-C. The latter would be expected to be strong owing to its higher solid solution element content. No significant trend in strength could be discerned with precipitate

32

coarsening rate coefficient, Ψ. Of the alloys cited above, one was in the first quartile, three in the second and one both in the third and fourth.

Strain rate sensitivity tests were conducted in order to gain some knowledge of the slower strain rate deformation mechanisms that occur under creep environments. By changing the strain rate during a simple tension test one can determine the strain rate sensitivity of the alloys. This will allow for the extrapolation to lower strain rates and thus a preliminary indication of creep resistance. This indirect method for determining creep resistance was employed to minimize the number of specimens needed for evaluation.

The mathematical model most commonly used in strain rate sensitivity testing is;

$$\sigma = A \, \dot{\epsilon}^m \qquad (20)$$

where m is a measure of the strain rate sensitivity. Generally, m is itself strain rate sensitive, but this factor must be experimentally determined.

A typical set of strain rate sensitivity results are given graphically in Fig. 53 for the alloy H87-24-C containing Ti and B with the corresponding monotonic tensile curve overlayed. One notes first that the apparent modulus is much greater at a $\dot{\epsilon}$ = 0.001 as opposed to $\dot{\epsilon}$ = 0.00026. This supports the supposition made previously that the low moduli observed from the tensile tests were in fact due to time dependent deformation. The slower strain rates are seen to lie just within the envelope described by the monotonic stress–strain curve. Tearing failure is evident in both specimens beginning at approximately 3% strain. A tabular summary of the strain rate sensitivity experiments is given in Table XII.

TABLE XI – MONOTONIC TENSILE TEST RESULTS

Spec. No.	Additions	$\dot{\epsilon}$ (sec^{-1})	σ_y (MPa)	σ_u (MPa)	E (GPa)	ϵ_f (MPa)	Failure Locations
88–25–A	Ti	0.00028	36.1	39.7	9.20	5.6	G
88–25–A1		0.00025	38.4	41.4	11.40	2.5	T
88–08–01	Ti–N	0.00029	75.2	88.3	4.70	9/3	G
88–08–3		0.00029	36.5	54.5	12.90	11.4	T
88–08		0.00024	82.7	103.4	12.40	6.3	G
88–06–1	Si–N	0.00030	67.6	67.6	5.50	8.4	G
88–06		0.00026	43.4	45.6	5.00	4.5	G
88–06–B		0.00026	12.4	49.0	6.50	9/5	T
87–12–D1	Hf–B	0.00026	69.0	72.4	6.60	3.8	T
87–12–C1	Zr–B	0.00025	57.4	65.5	12.40	4.5	G
87–13–A1	Hf–N	0.00029	135.1	138.6	10.90	6.6	G
87–13–A–1B		0.00024	42.1	43.0	15.20	2.3	T
87–13–A		0.00025	54.5	65.5	6.80	2.4	G
87–24–C2	Ti–B	0.00026	40.7	44.8	5.40	6.0	G
87–22–A2	Mo–Ta–	0.00026	53.8	88.9	7.80	10.5	G
87–22–A	Zr–C	0.00024	——	67.6	6.80	1.0	G

T = Tab Failure   G = Gage Section Failure

TABLE XII – STRAIN RATE SENSITIVITY RESULTS AT 1400°C

Alloy No.	Alloying Elements	$\dot{\epsilon}$ (sec^{-1})	σ_m (MPa)	m
H88-25-A2	Ti	0.001		
		0.0004	41.14	
		0.00015	29.20	
		0.001	15.56	
H88-25-A2		0.001		0.060
		0.0033	28.97	
		0.0065	50.73	
		0.001	43.67	
		0.0065	39.89	
H88-08-4	Ti-N	0.001	57.19	
		0.00035	58.14	
		0.00015	53.55	
		0.001	59.48	
		0.00015	42.50	
		0.001	42.40	
H88-08-5		0.001		0.048
		0.0034	49.15	
		0.0068	58.97	
		0.001	52.17	
		0.0068	60.35	
H88-06-2	Si-N	0.001		
		0.00375		
		0.00015	44.33	
		0.001	53.22	
		0.00015	24.97	
H88-06-A-3		0.0011		0.138
		0.0034	55.96	
		0.0069	82.95	
		0.0011	68.06	
		0.0069	76.40	
H87-12-D2	Hf-B	0.001		
		0.0039	74.26	
		0.00015	62.28	
		0.001	53.88	
H87-12-D		0.001		0.084
		0.0033	77.29	
		0.0066	90.05	

TABLE XII – STRAIN RATE SENSITIVITY RESULTS AT 1400°C (CONTINUED)

Alloy No.	Alloying Elements	$\dot{\epsilon}$ (sec^{-1})	σ_m (MPa)	m
H87–12–C–2	Zr–B	0.001		
		0.0004		
		0.00016	75.37	
		0.001	91.50	
		0.00016	35.59	
H87–12–C		0.001	10.94	
		0.003	24.29	
		0.0067	42.87	
		0.001	63.70	
		0.0067	53.55	
H87–13–A–3	Hf–N	0.001		
		0.0033		
		0.0067		
		0.001	80.60	
		0.0067	40.06	
H87–24–C–3	Ti–B	0.0011		
		0.00042	34.52	
		0.00017	30.71	
		0.0011	63.23	
		0.00017	38.72	
H87–24–C–1		0.001		0.170
		0.0033	66.49	
		0.0067	65.59	
		0.001	41.23	
		0.0067	39.40	
H87–22–A–3	Mo–Ta–Zr–C	0.001	6.55	
		0.0032	43.09	
		0.0065	36.54	
H87–22–A–4		0.001		
		0.0039		
		0.000156		
		0.001	164.31	
		0.000156	114.66	
		0.001	88.95	

Only maximum stresses, σ_m, are reported where a well defined flow stress could be measured. In all cases, the maximum stress and the flow stress were the same except in instances where specimen tearing could be inferred due to rapidly decreasing strength. In many instances, the initial strain rate of 0.001 sec^{-1} was terminated prior to achievement of a well defined flow stress (see Fig. 52) and thus in these instances no stress data is reported in Table XII. Calculations of the coefficient, m, were made and are also given where statistically reliable results were obtained. Any stress levels which were reported in Table XII and later identified as resulting from the tearing region of the stress strain curve were disregarded.

A number of difficulties were encountered in this analysis. Due to the thin cross section of the specimens, limited strain to failure was observed with plane stress tearing occurring at about 3% strain. These plane stress effects were enhanced by the high temperature of testing. The limited strain to failure did not allow for extensive testing of strain rate in any of the specimens.

Generally, the alloys studied here were strain rate insensitive over the two orders of magnitude of strain rate studied. Only two alloys, H88–06 and H87–24–C, showed appreciable strain rate sensitivity. The low strain rate exponents are characteristic of superalloy blade materials which are utilized in high temperature, low stress conditions. Additionally, this low value of m may also indicate a high back stress condition resulting from dislocations piled up against the fine precipitate phase.
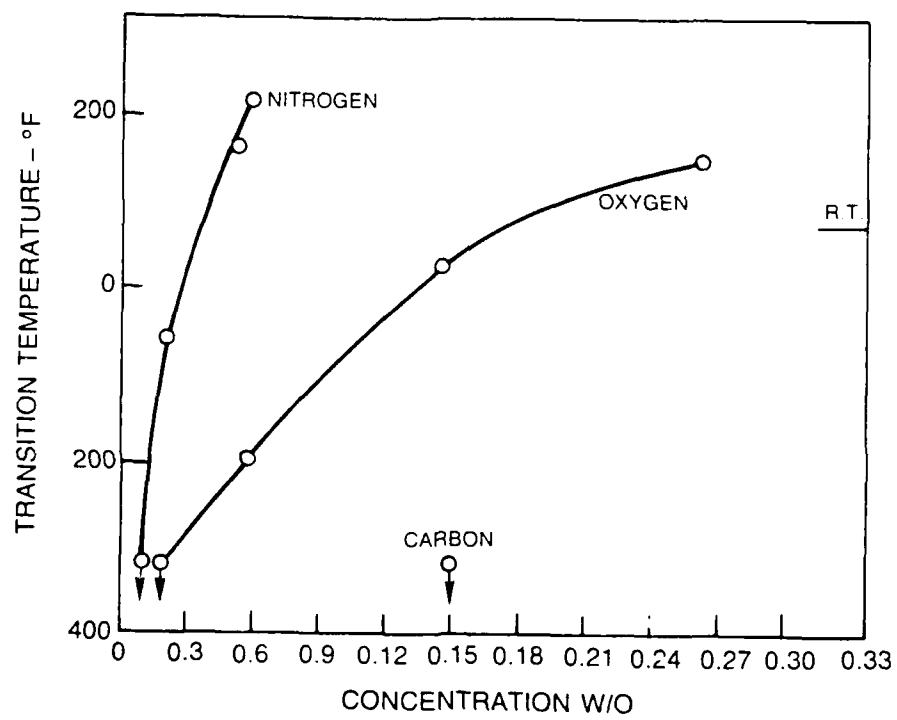
Figure 7.   Effect of Interstitals on Transition Temperature of Niobium

(a)

(b)
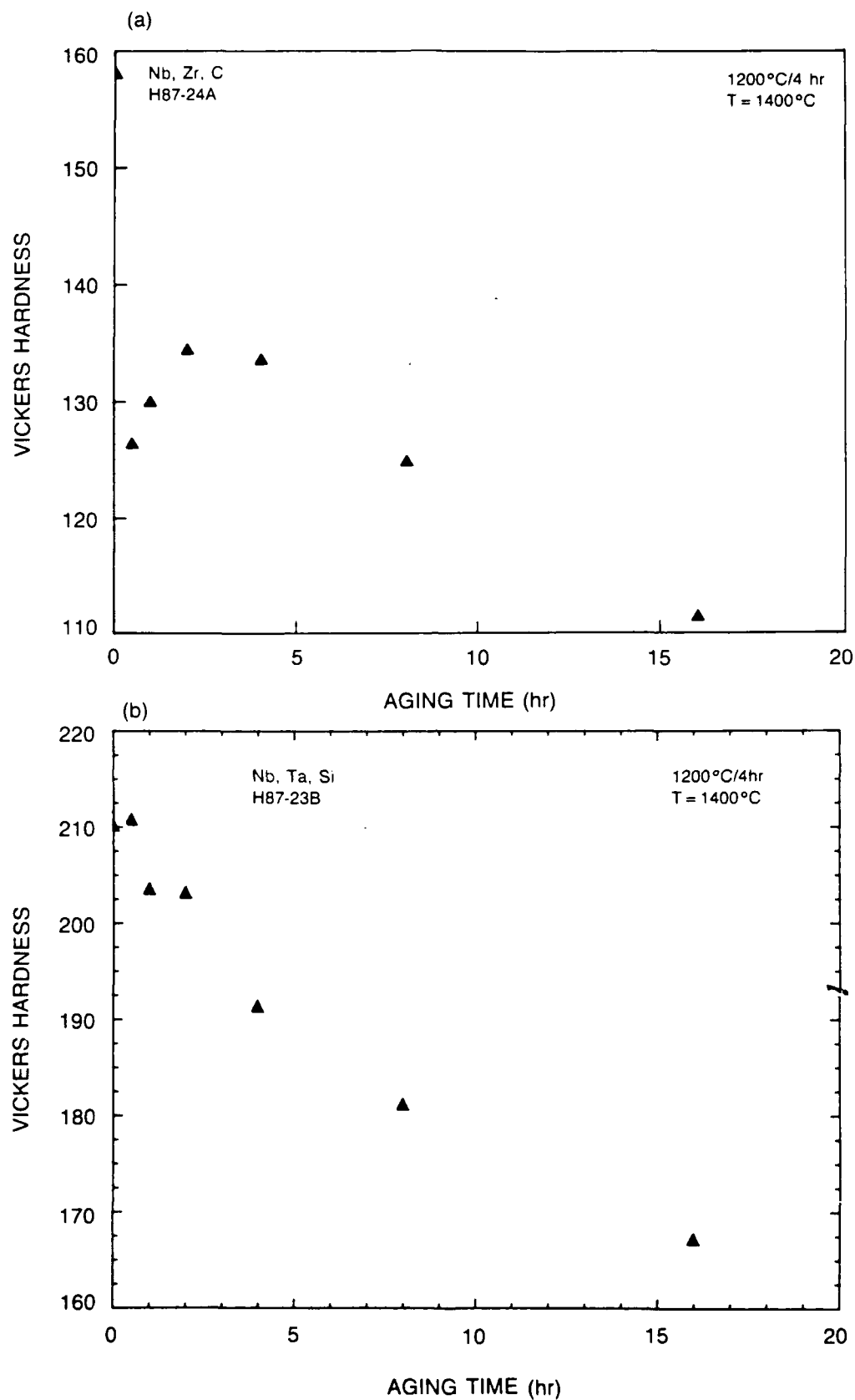
Figure 8. Isothermal Age Hardening Plot for (a) ZrC and (b) Ta_5Si_3 Hardened
System Showing Classical Age Hardening Followed by Softening

89—6—73—17

(a)

SLOPE = 0.131
INTERCEPT = 2.208

(b)

SLOPE = 0.065
INTERCEPT = 2.313
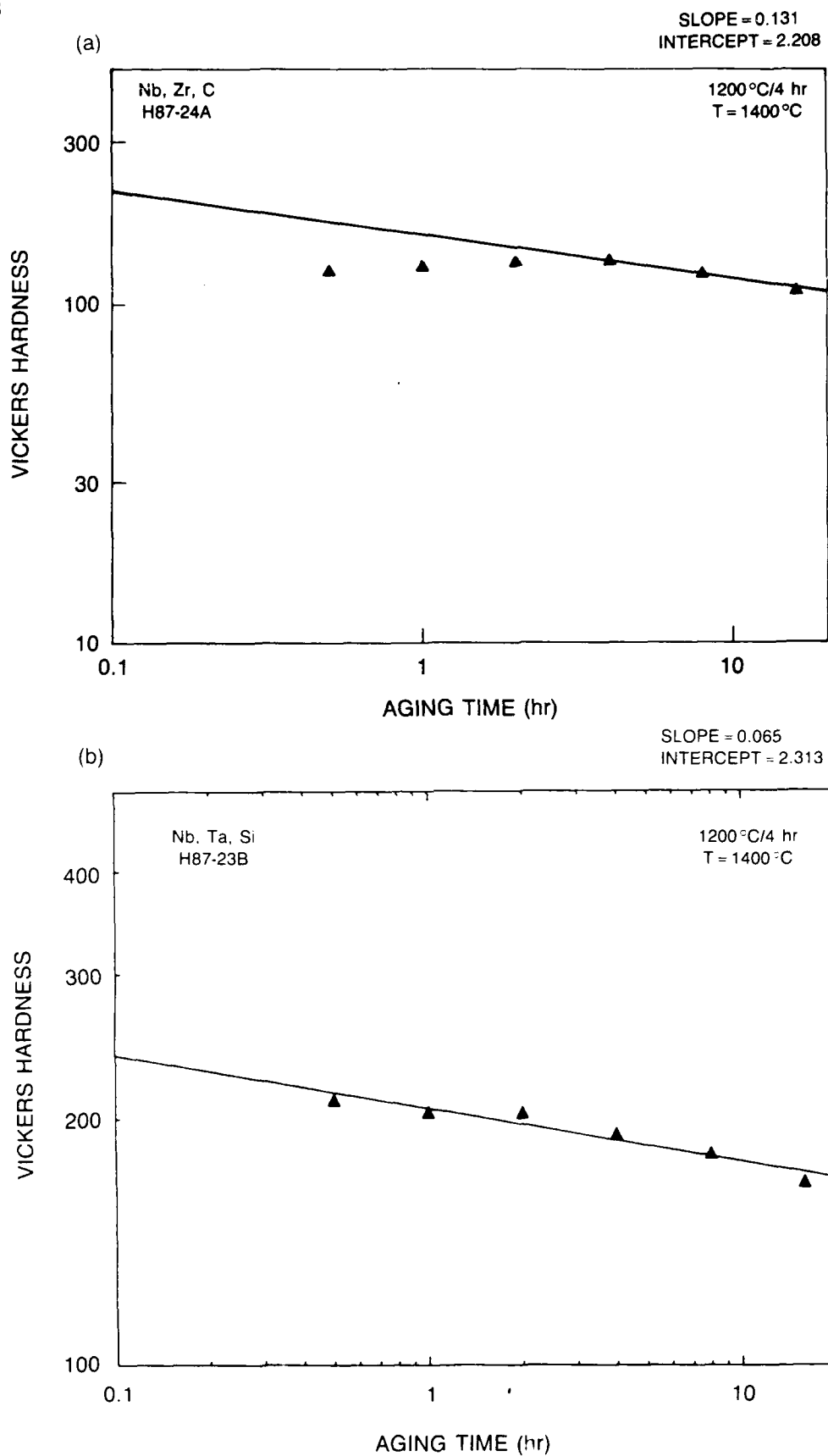
Figure 9.   Isothermal Age Hardening Plots as Shown in Fig. 8 Illustrating ℓn-ℓn Plot in Over-Aged Regions of (a) ZrC and (b) Ta$_5$Si$_3$ Containing Alloys

88—7—1—3

20 μm
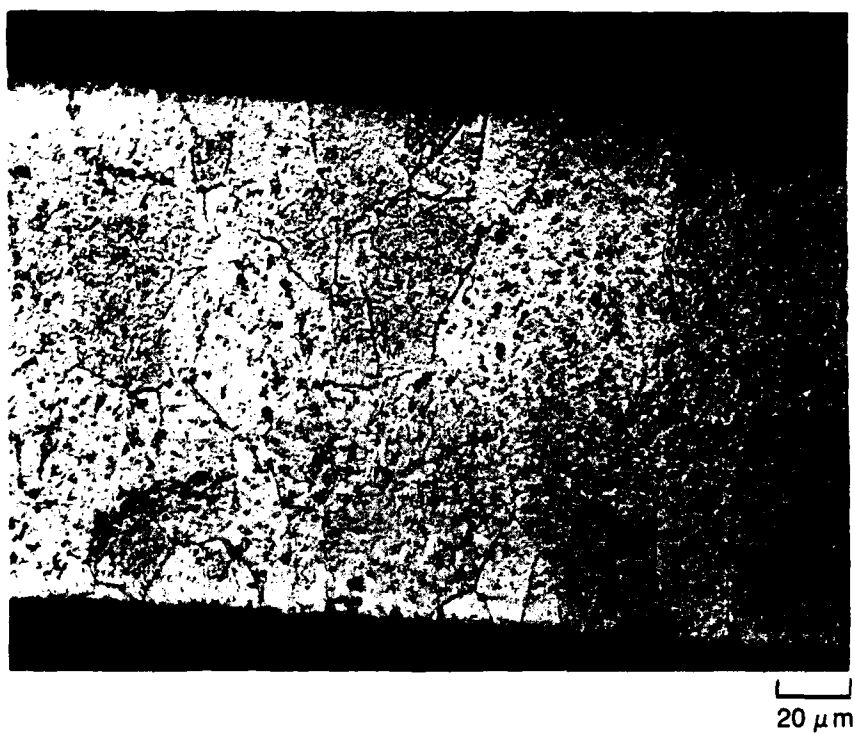
Figure 10. Cross-Section of Zr-C Alloy Splat After Exposure at 1400°C for 8 hrs Revealing Equiaxed Grain Structure and Fine Precipitates.

20 μm
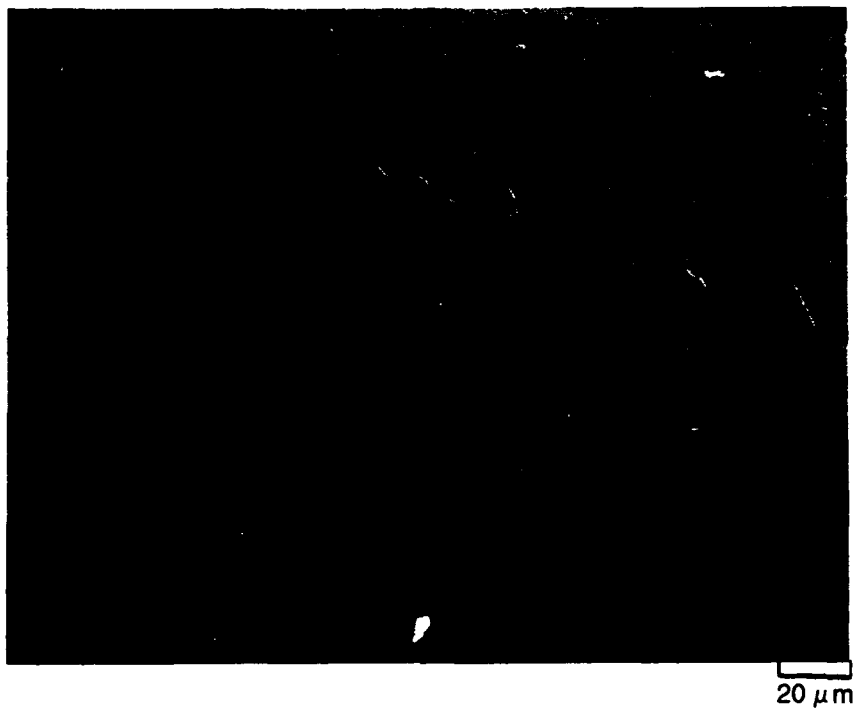
Figure 11. Cross-Section of Hf-N Alloy Splat After Exposure at 1400°C for 1 hr Revealing Equiaxed Grain Structure and Grain Boundary Precipitates.

88—7—1—5
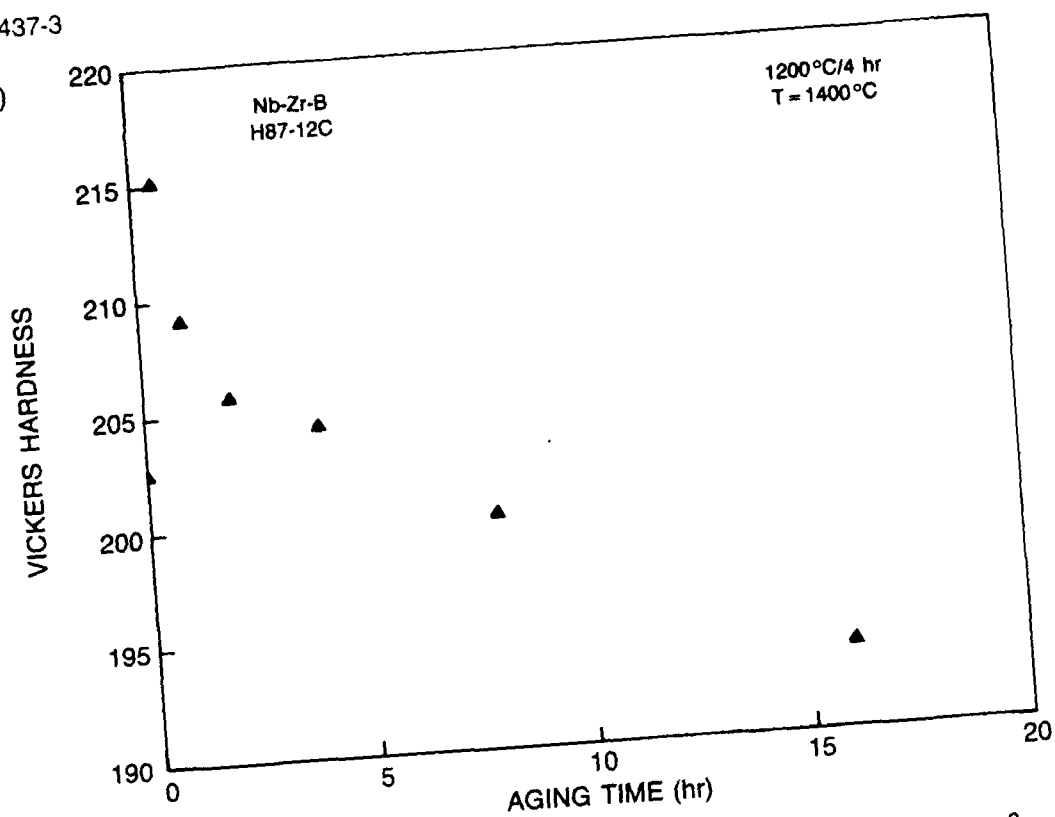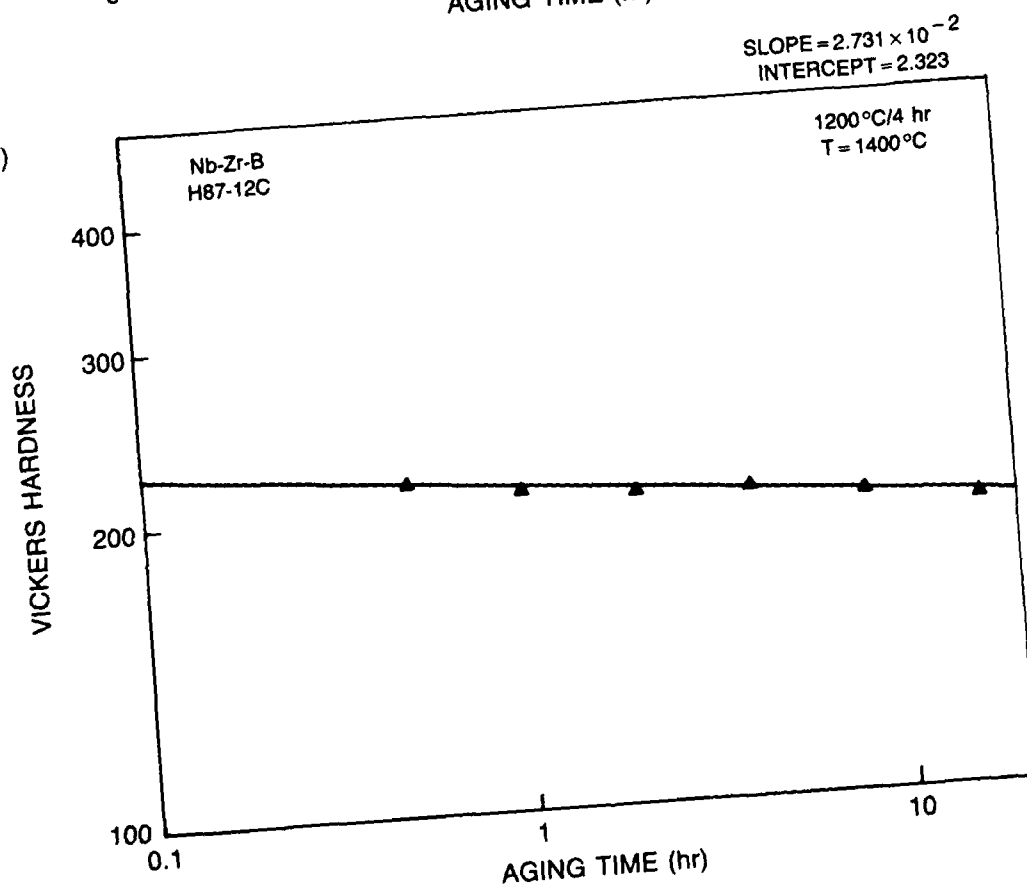
Figure 12. Isothermal Age Hardening Plots for Zr-B Alloy Illustrating (a) Rapid Hardening Followed by Over-Aging and (b) Linearized Plot Showing Excellent Fit of Data.

42

88—7—1—6
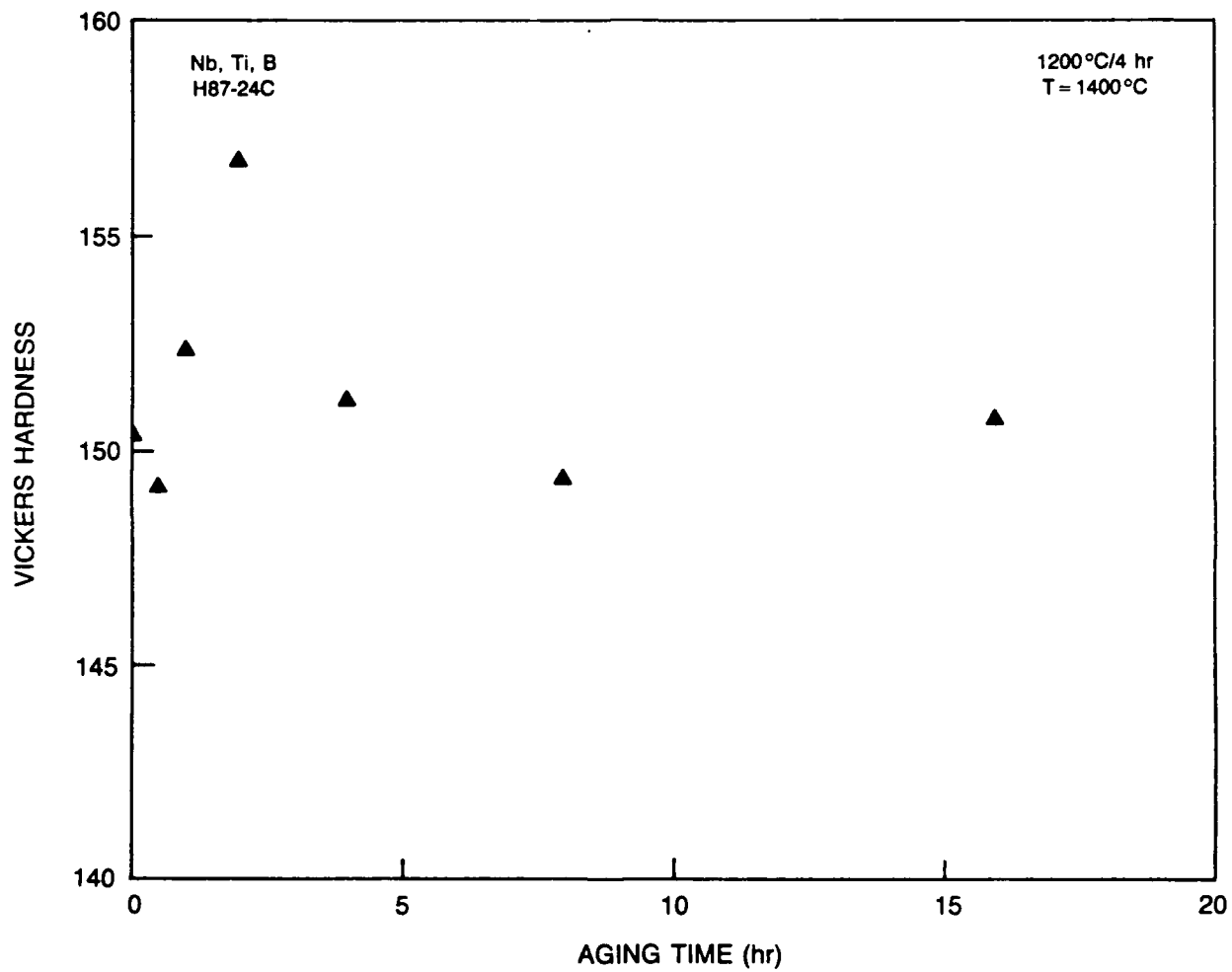
Figure 13. Isothermal Age Hardening Plot for Ti-B Alloy Illustrating Primary and Secondary Hardening.
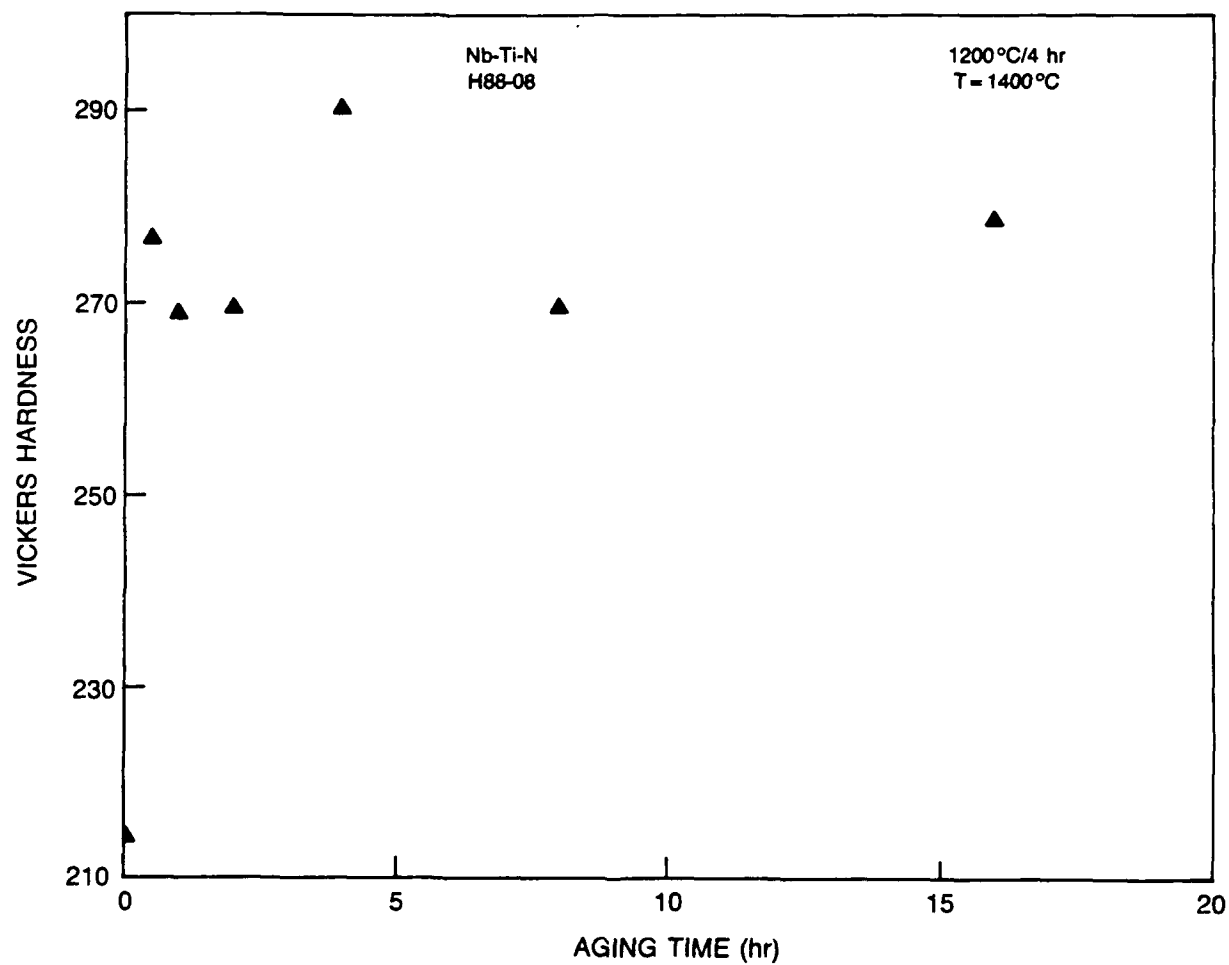
Figure 14. Isothermal Age Hardening Plot for Ti-N Alloy Illustrating Rapid Hardening on Initial Exposure to 1400°C and Negligible Subsequent Hardening.

88—7—1—8
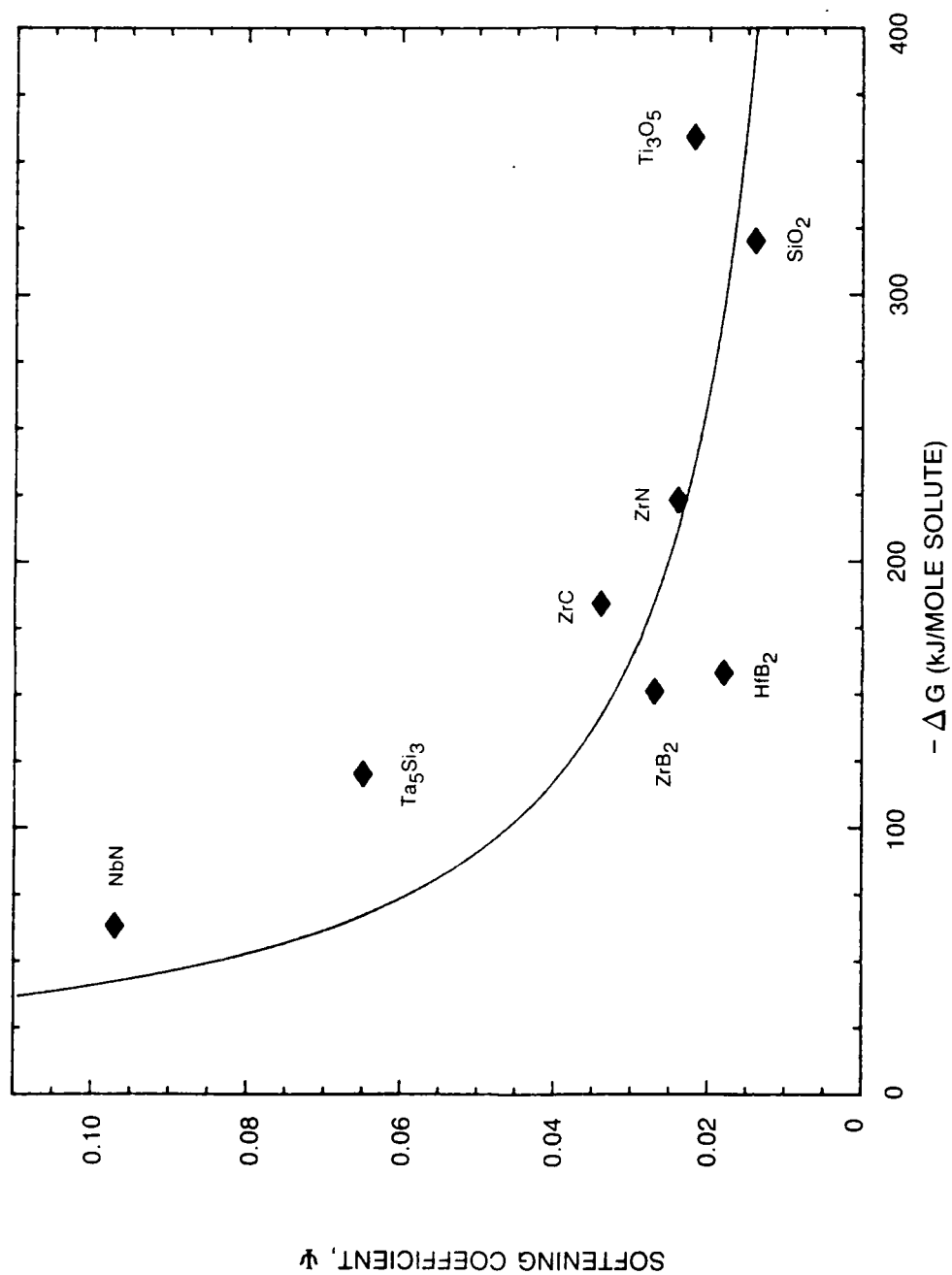
Figure 15. Plot of Ψ as a Function of $-\Delta G$ Showing a General Trend of Lower Ψ with Greater $-\Delta G$

45
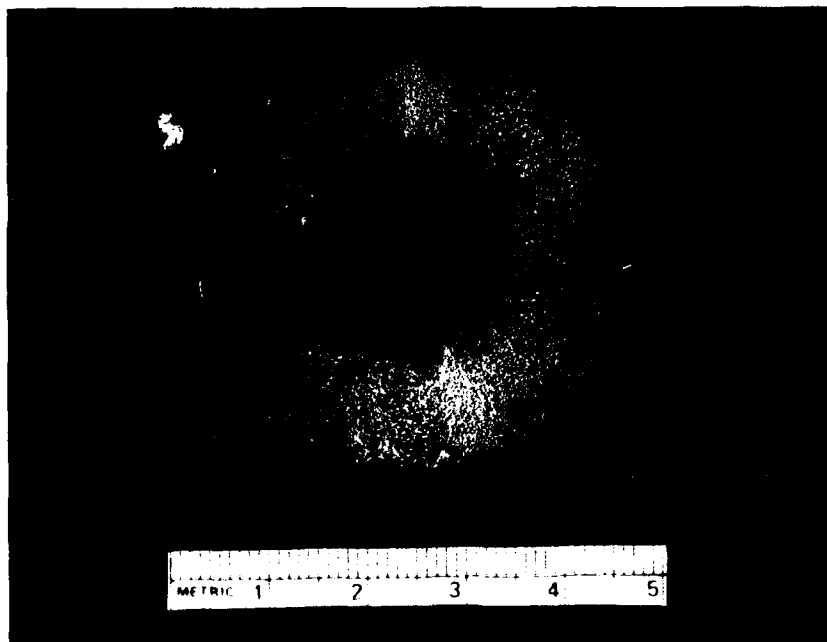
Figure 16. Typical Splat of Niobium

20μm

Figure 17. Pure Niobium Cross Section

(a)

HEAT TREATED 1500°C/4 hrs/vac

20μm

(b)

20μm
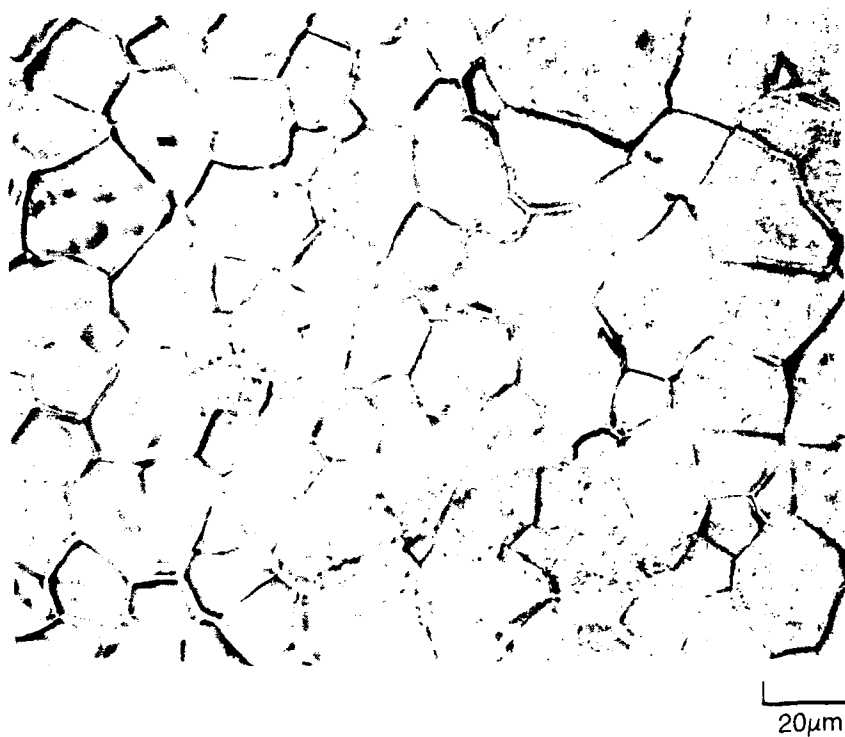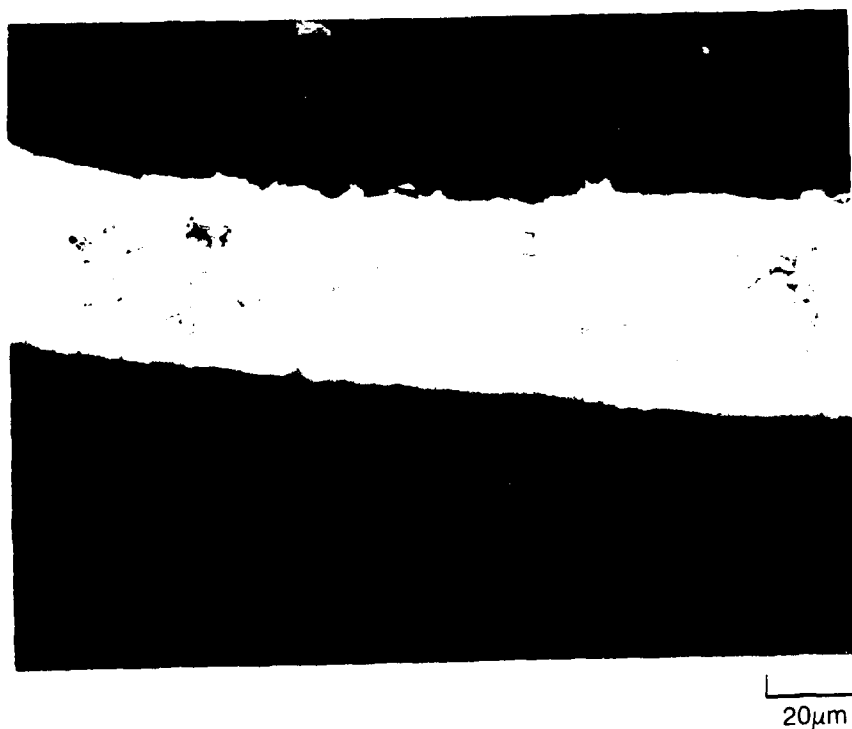
Figure 18   Nb-Hf-N Splat

87 - 6 - 20 - 6

48

(a) BRIGHT FIELD

(b) DARK FIELD

0.22μ
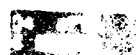
(c) DIFFRACTION PATTERN

Figure 19. Zirconia Particles After Heat Treatment

NOTE GROWTH OF PARTICLES AS COMPARED TO FIG 19

ALLOY: Ng-8Mo-0.1Zr-0.1N
CONDITION: SQ/1400C/4 hr

(b) DARK FIELD

(a) BRIGHT FIELD

0.15μm
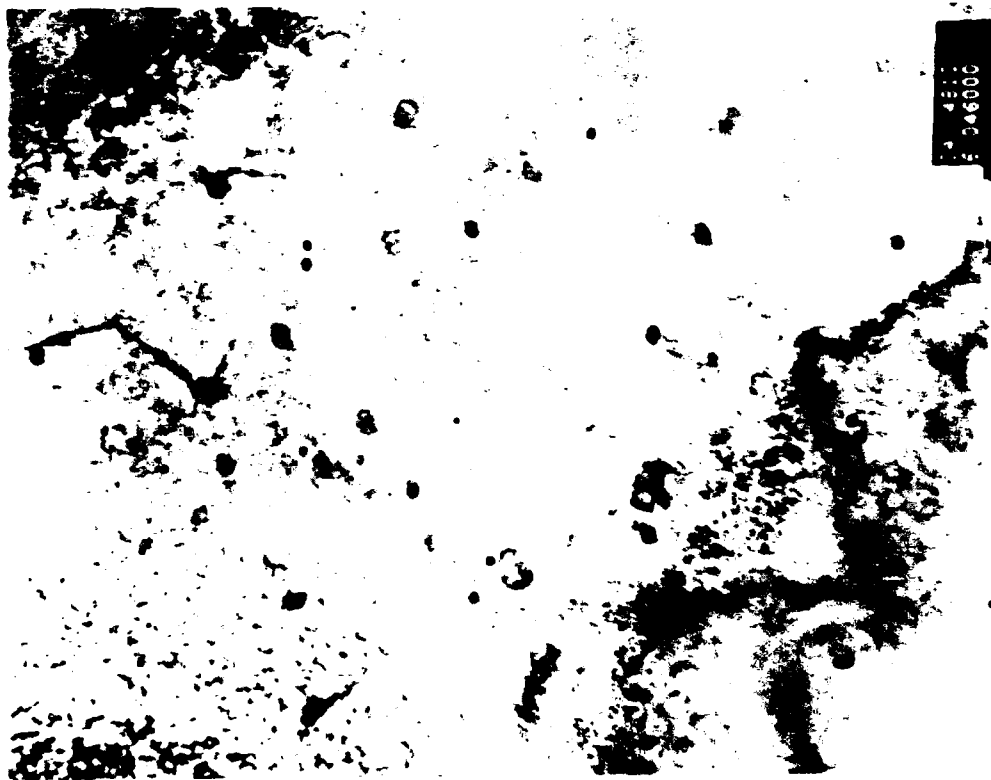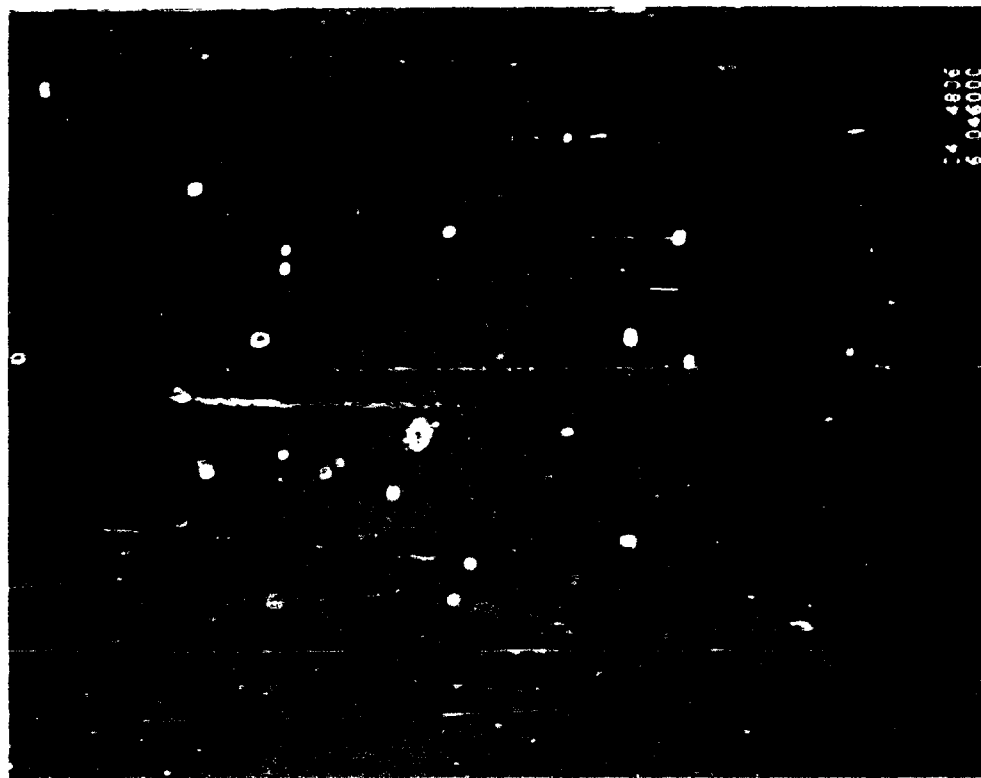
Figure 20.   Zirconia Particles After Heat Treatment

GRAIN BOUNDARY PARTICLES ARE ZrO_2

0.24µm

Figure 21. As Splat Quenched Microstructure Showing No Matrix Precipitates

ALLOY: Nb-8Mo-0.6Zr-0.6N
CODITION: SQ/1400C/4 hr

(b) DIFFRACTION PATTERN

6.15μm
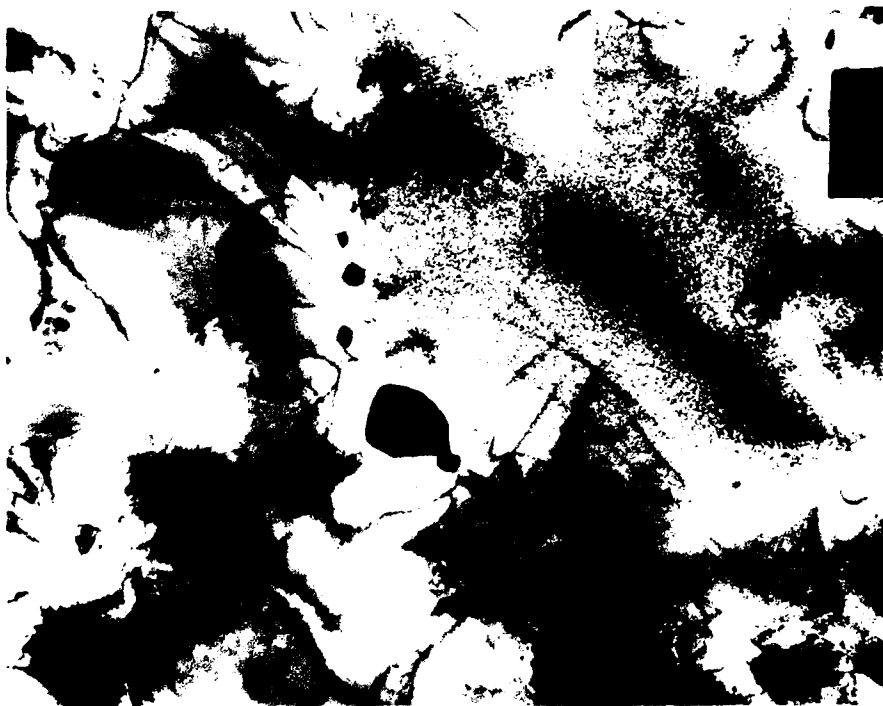
(a) BRIGHT FIELD

Figure 22. Precipitate Used in Identification of ZrO$_2$ with P2 at Center and P3 at Upper Left

87—6—20—10
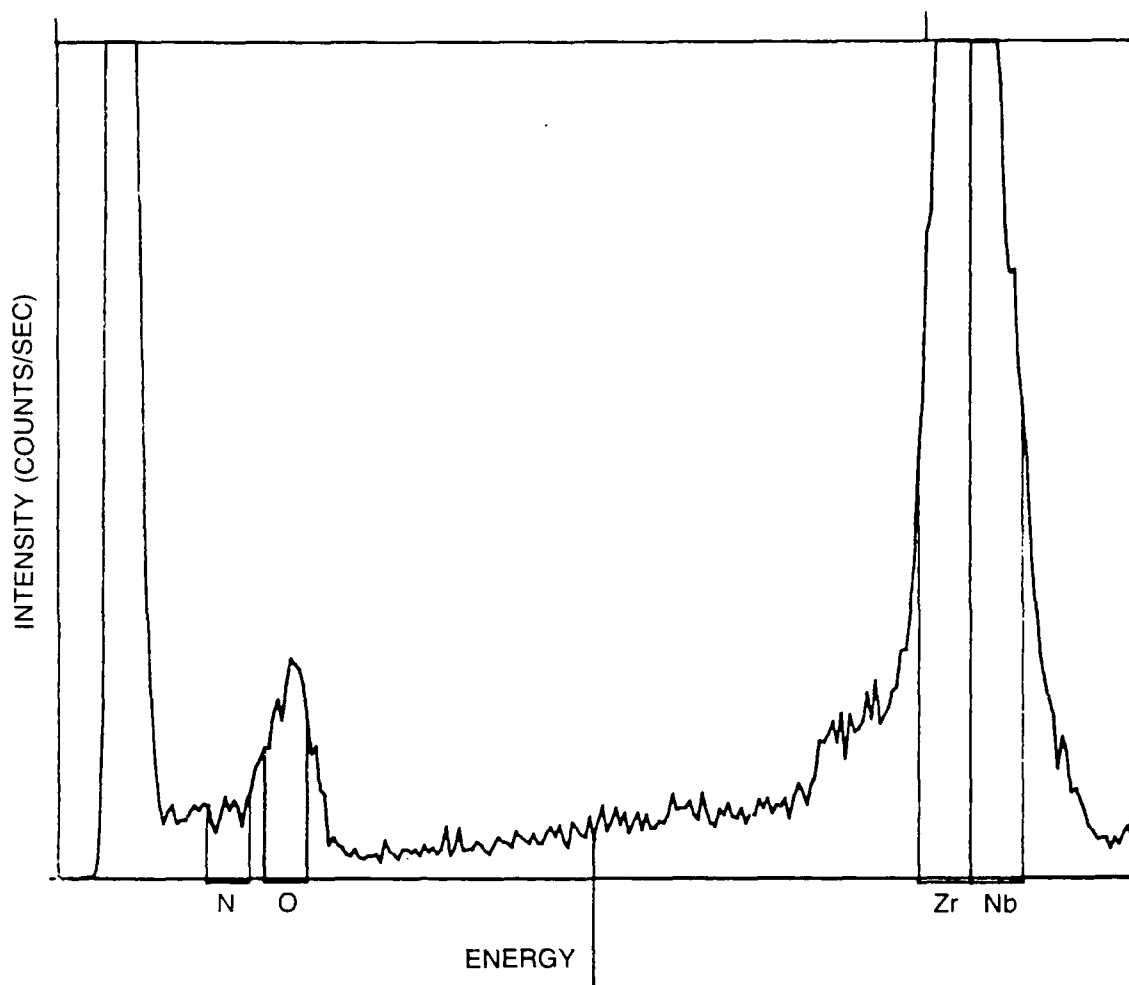
Figure 23. Energy Dispersive Spectra of P2 Particle (See Text) Confirming Oxygen and Zirconium Content

53

ALLOY: Nb-8Mo-0.1Hf-0.1B
CONDITION: SQ

0.67μm
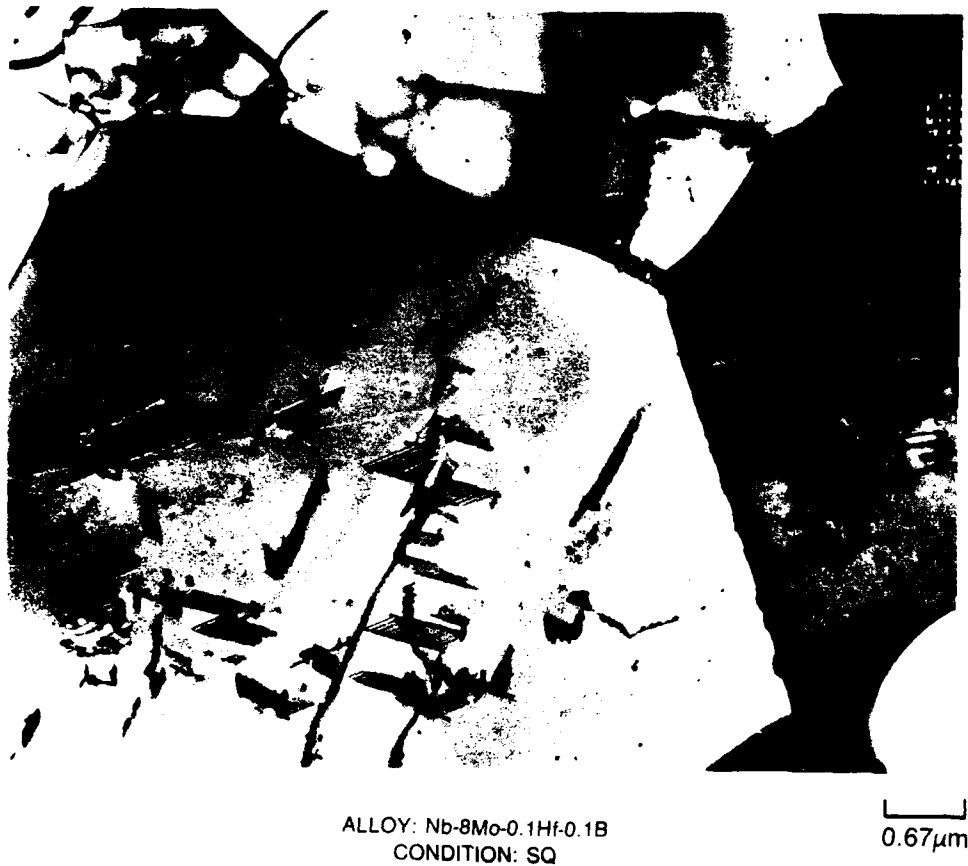
Figure 24.   Platelet Phase Found in Grain Interiors Identified As NbB

ALLOY Nb-8Mo-0.1Hf-0.1B
CONDITION SQ

(a) BRIGHT FIELD

|___|
80 nm

(b) DARK FIELD
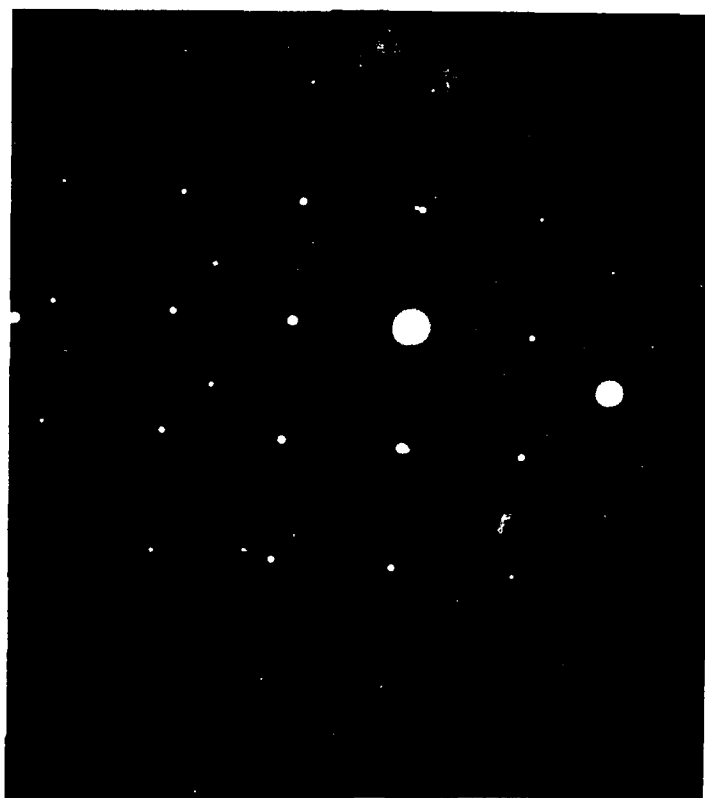
(c) DIFFRACTION PATTERN

Figure 19.   Zirconia Particles After Heat Treatment

87 6-20 8

ALLOY: Nb-8Mo-0.1Zr-0.1B
CONDITION: SQ

(b) DIFFRACTION PATTERN
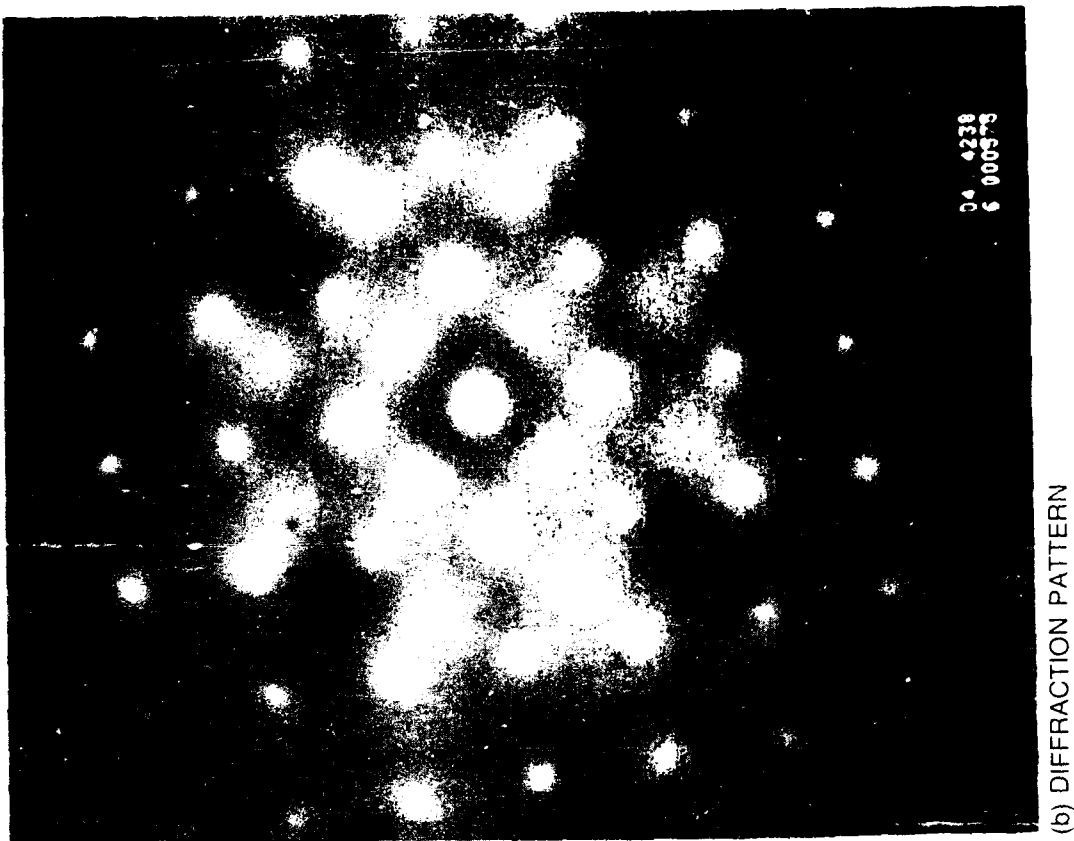
(a) BRIGHT FIELD

Figure 26.   Platelet Phases Identified As NbB

GENERAL VIEW OF THE MICROSTRUCTURE

Figure 27.   Splat Quenched Nb-8Mo-0.1Ti-0.1B

(a) INTRAGRANULAR PRECIPITATES ON (100). AREA OF FIG. 27. BRIGHT FIELD
$\bar{q}$ = PRIMARILY [002] MATRIX
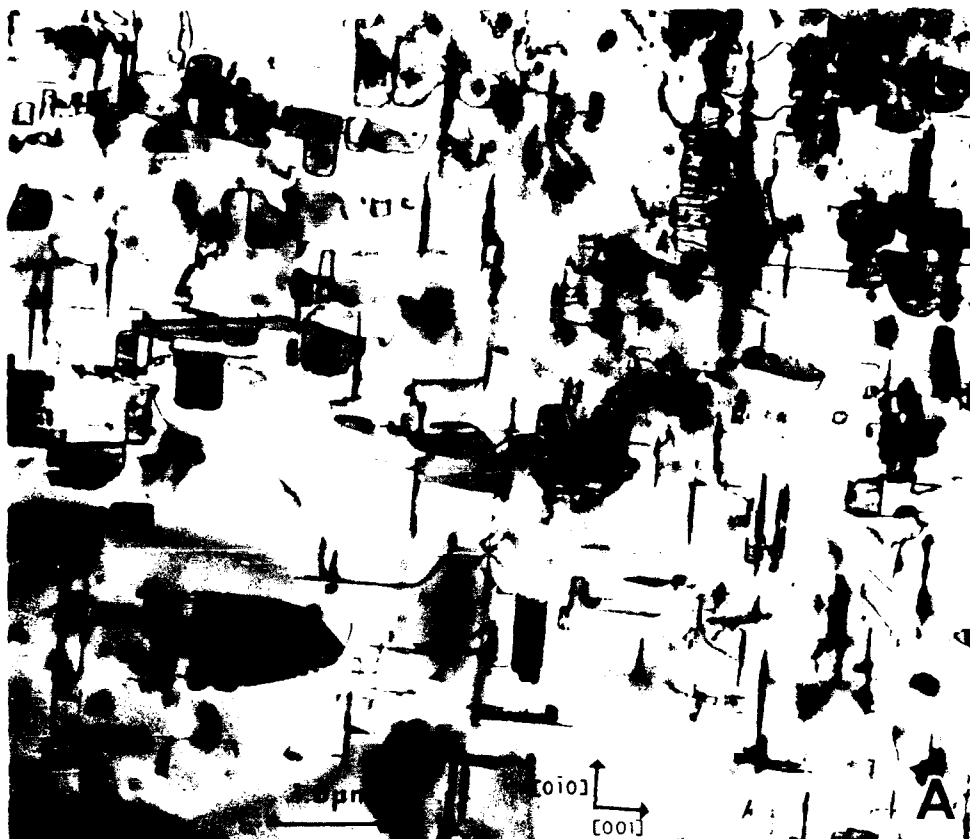
(b) SELECTED AREA DIFFRACTION PATTERN FROM CENTER OF (a), $\bar{B}$ NEAR [001]
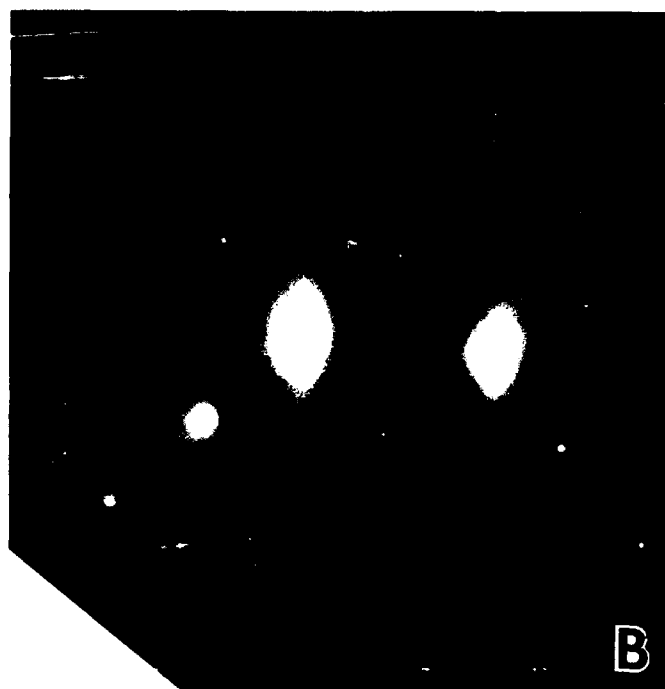
Figure 28.   Splat Quenched Nb-8Mo-0.1Ti-0.1B

58

(a) BRIGHT FIELD. (b) DARK FIELD, $\bar{g}=[0\bar{2}\bar{1}]$ NbB. (c) SADP FROM THIS AREA, $\bar{B}$ NEAR [001]. POINTER MARKS $\bar{g}$ USED FOR (b).
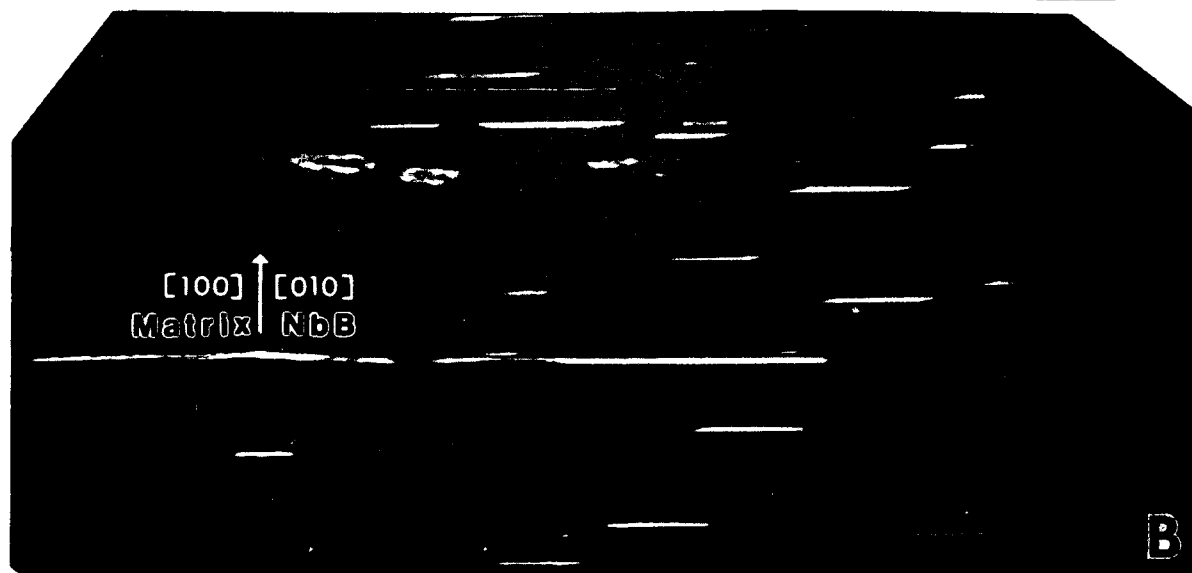
Figure 29.   Splat Quenched Nb-8Mo-0.1Ti-0.1B

88—7—1—16

SCHEMATIC SELECTED AREA DIFFRACTION PATTERNS ILLUSTRATING THE ORIENTATION
OF ONE VARIANT OF ORTHORHOMBIC NbB TO THE BCC MATRIX (FIG. 3)

Lattice Parameter(s):   a = 3.295 Å

a = 3.292 Å   b = 8.713 Å   c = 3.165 Å

330

220

130   1̄10

020

000

001   002   003   004

010   011   012   013   014

020   021   022   023   024

1̄30   +̄10   030   031   032   033   034

              040   041   042   043   044

2̄20

3̄30
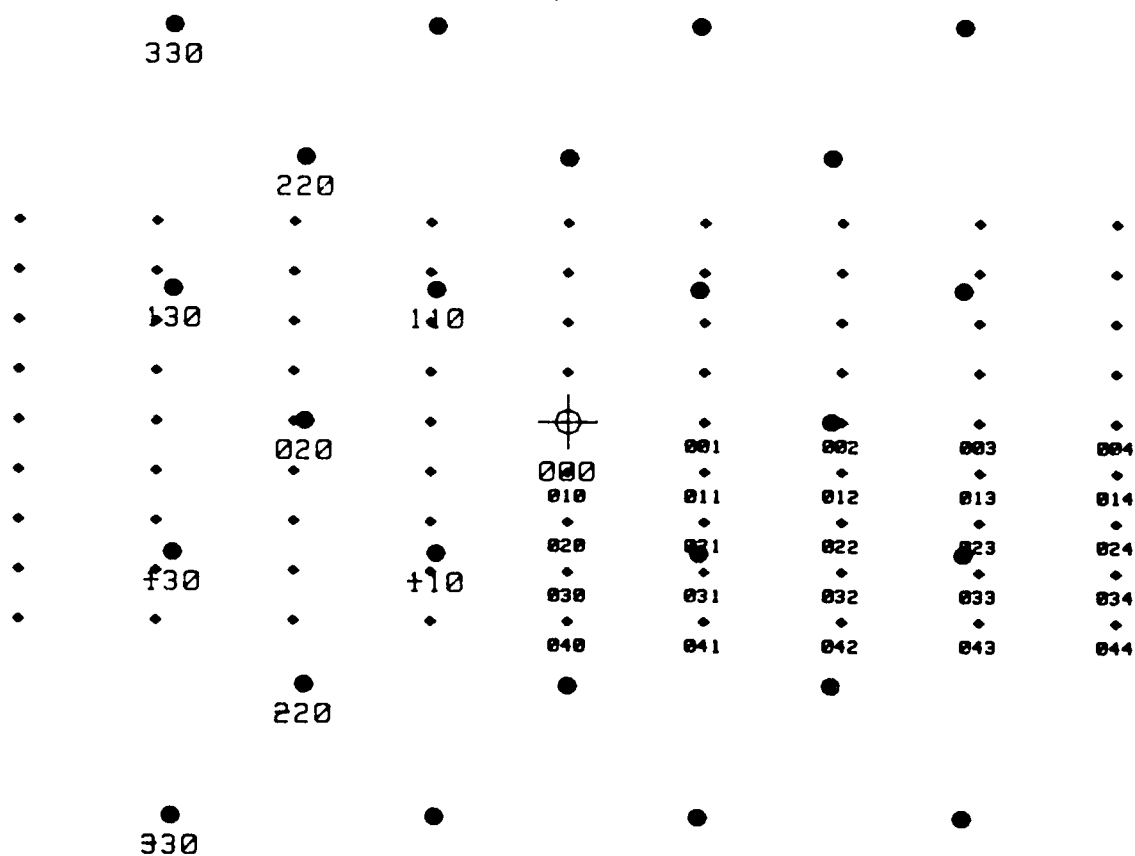
Figure 30. Splat Quenched Nb-8Mo-0.1Ti-0.1B

60

GENERAL VIEW OF THE MICROSTRUCTURE

Figure 31.   Nb-1.2Ti-0.6N, Aged at 1200°C/4 hr

(a) BRIGHT FIELD. (b) DARK FIELD, $\bar{g}=[1\bar{1}01]$ Nb$_2$N. (c) SADP FROM THIS AREA, $\bar{B}$ NEAR [001] MATRIX AND [11$\bar{2}$0] Nb$_2$N. POINTER MARKS 1$\bar{1}$01 SPOT USED TO FORM (b)
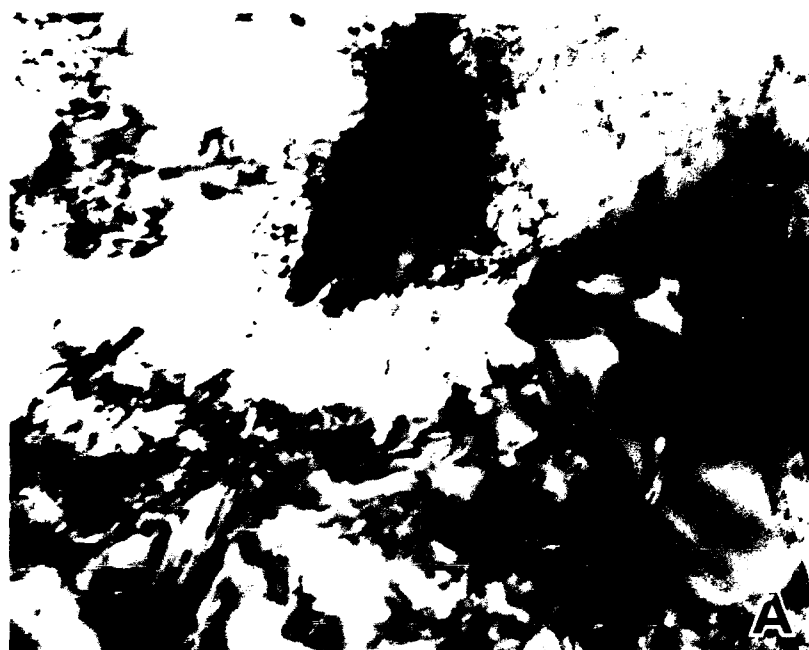
Figure 32. Grain Boundary Precipitate, Nb-1.2Ti-0.6N, Aged at 1200°C/4 hr

SCHEMATIC OF SUPERIMPOSED SELECTED AREA DIFFRACTION PATTERNS,
[001] MATRIX AND [11$\bar{2}$0] Nb$_2$N, CORRESPONDING TO FIG. 32(c)

Lattice Parameter(s): a = 3.3007 Å
a = 3.058 Å   c = 4.961 Å
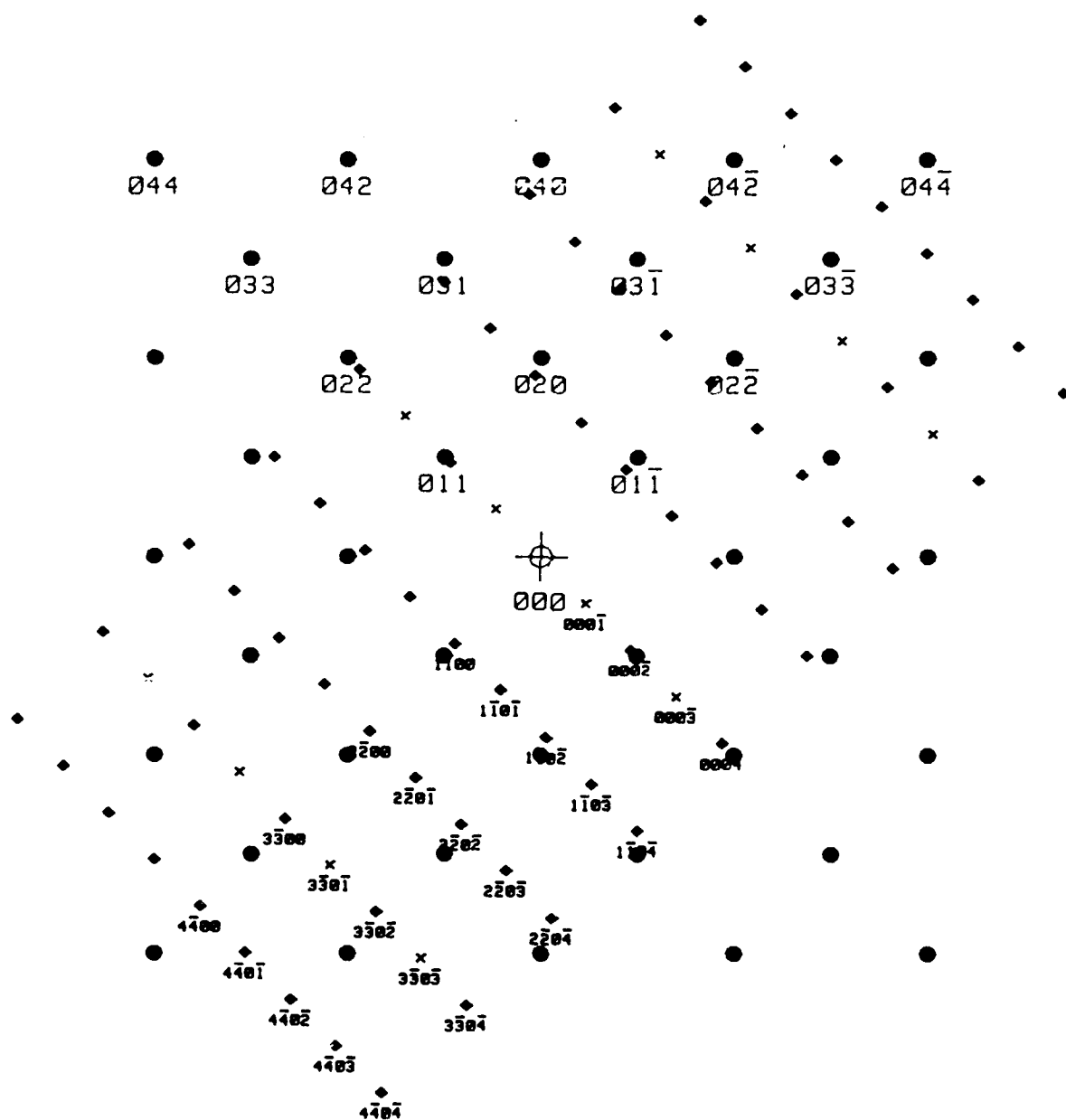
Figure 33.   Nb-1.2Ti-0.6N, Aged at 1200°C/4 hr

63

(a) BRIGHT FIELD. (b) DARK FIELD, $\bar{g} = [1\bar{1}02]$ Nb_2N. (c) SADP FROM THIS AREA, $\bar{B}$ NEAR [001] MATRIX AND $[11\bar{2}0]$ Nb_2N. POINTER MARKS $1\bar{1}02$ SPOT USED TO FORM (b)
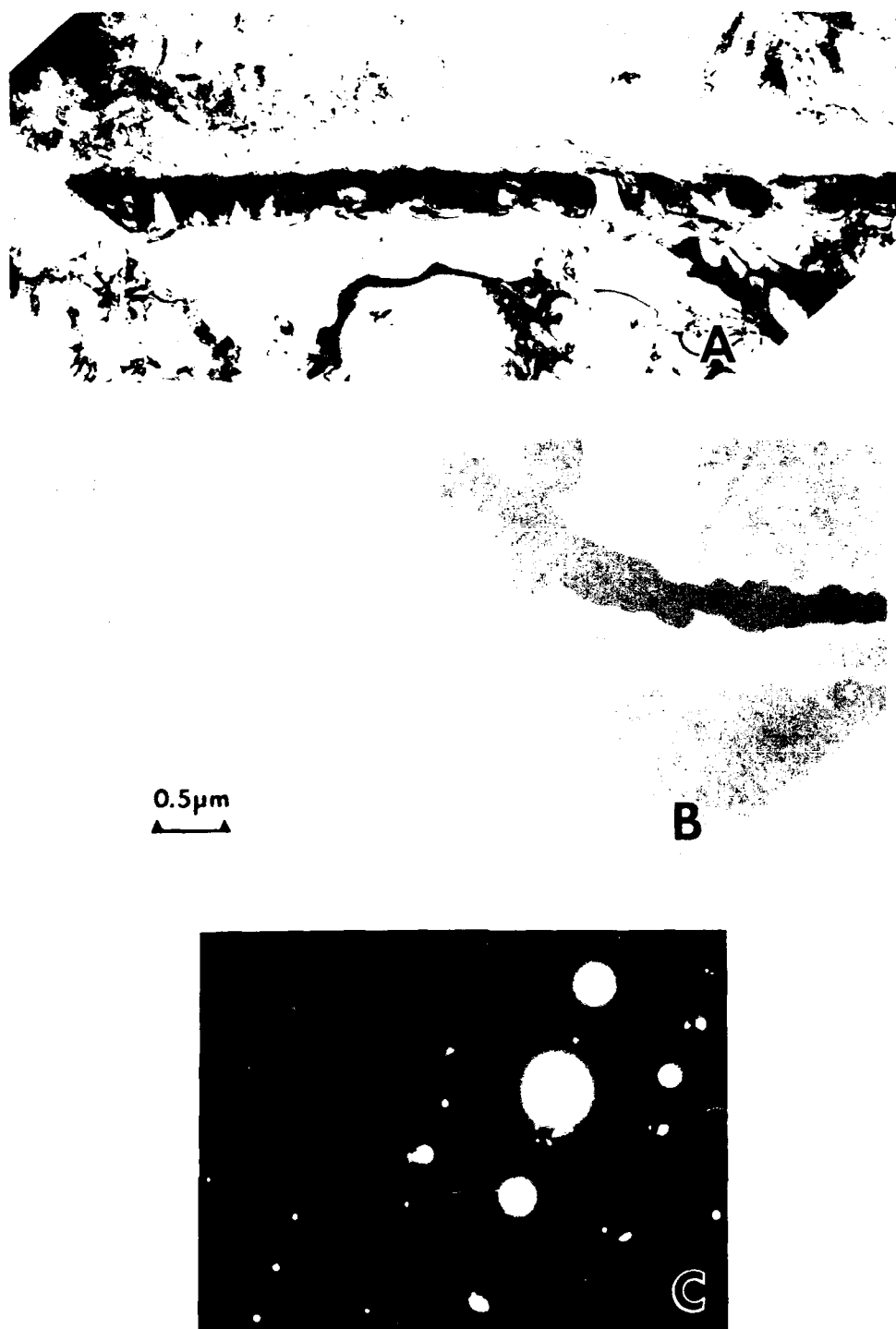
Figure 34.   Coalesced Grain Boundary Precipitates, Nb-1.2Ti-0.6N, 1200°C/4 hr

88—7—1—21

HIGH AND LOW CAMERA LENGTH 11$\bar{2}$0 ZONE AXIS PATTERNS, PRECIPITATE
IN ROW SHOWN IN FIG. 34
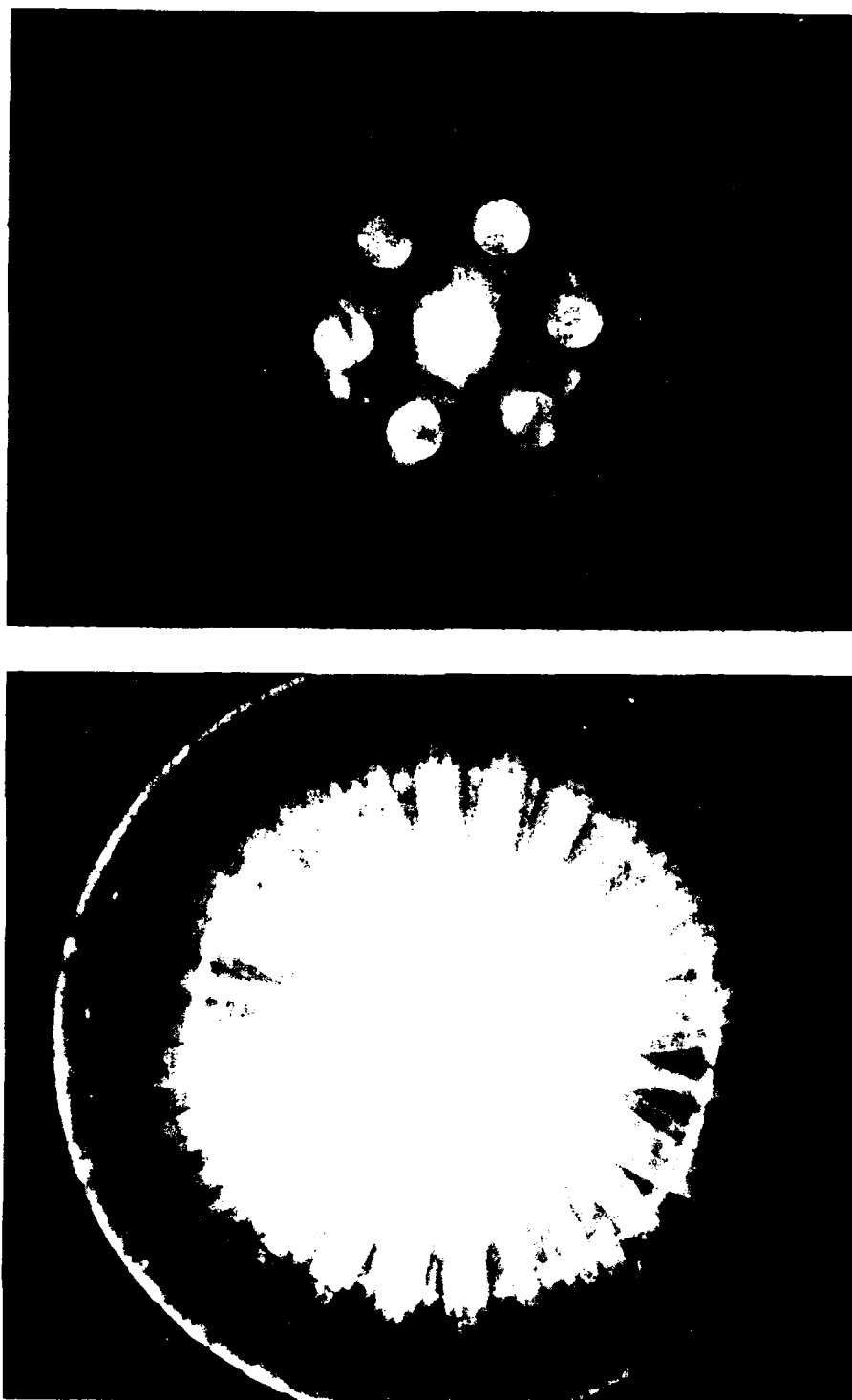
Figure 35. CBED Patterns from Grain Boundary Precipitate, Nb-1 ?Ti-0.6N, 1200°C/4 hr

88—7— 1—22

(a) BRIGHT FIELD. (b) DARK FIELD, $\bar{g}=[1\bar{1}01]$ Nb$_2$N. (c) [11$\bar{2}$0] SADP FROM THIS AREA, [110] MATRIX PARALLEL TO [0001] Nb$_2$N. POINTER MARKS 1$\bar{1}$01 SPOT USED TO FORM (b). (d) [11$\bar{2}$0] ZONE AXIS CONVERGENT BEAM MICRODIFFRACTION PATTERN FROM PRECIPITATE; 50 μm CONDENSER APERTURE; 100 nm SPOT SIZE
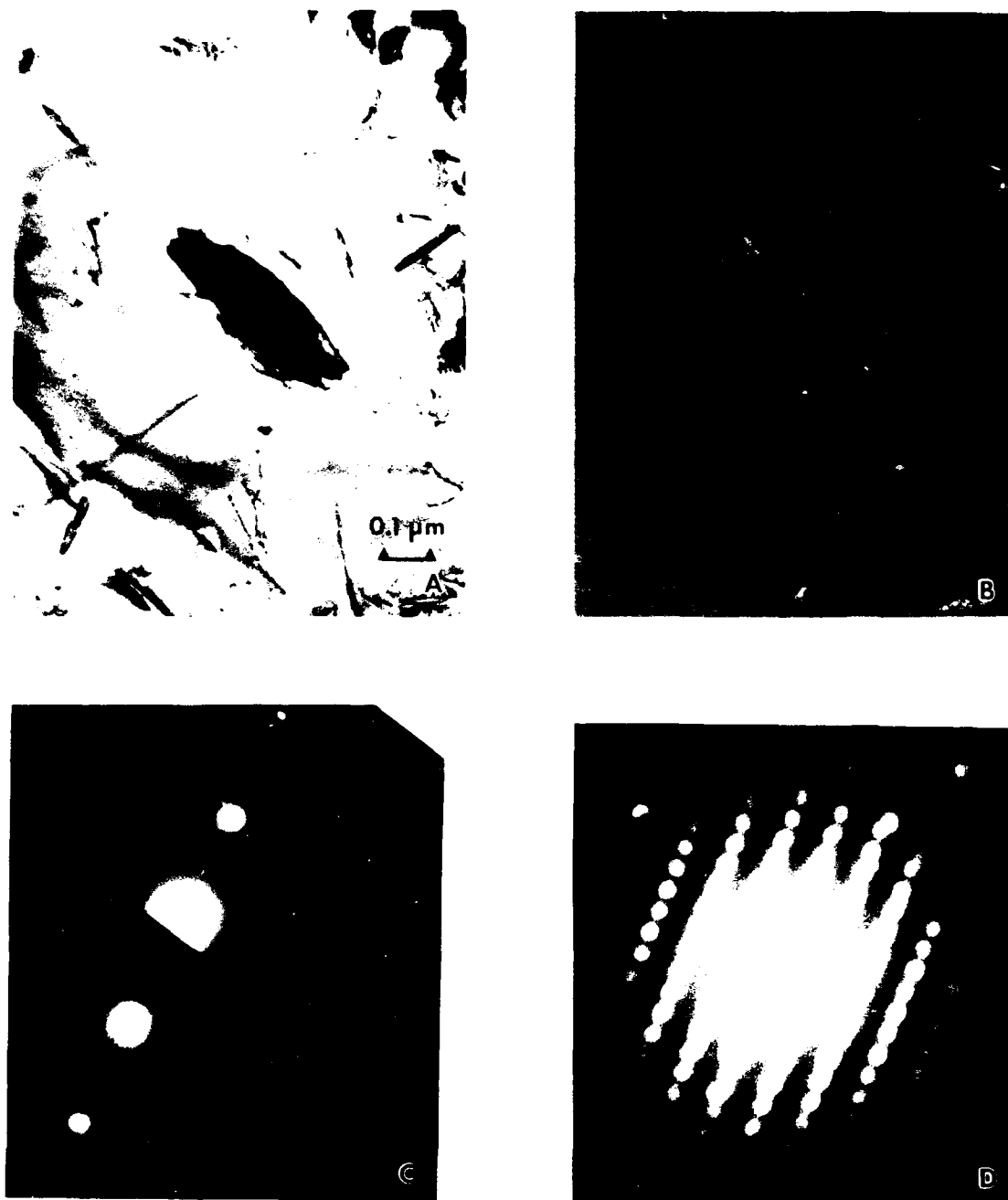
Figure 36. Intragranular Nb$_2$N Precipitate, Nb-1.2Ti-0.6N, Aged at 1200°C/4 hr

(a) BRIGHT FIELD. (b) DARK FIELD, $\bar{g} = [220]$ TiN. (c) SUPERIMPOSED $[\bar{1}12]$ MATRIX AND $[\bar{1}12]$ TiN SADP'S FROM THIS AREA, ARROW MARKS 220 TiN SPOT USED FOR (b). (d) CONVERGENT BEAM MICRODIFFRACTION PATTERN CORRESPONDING TO (c), 70 μm CONDENSER APERTURE; 100 nm SPOT SIZE.
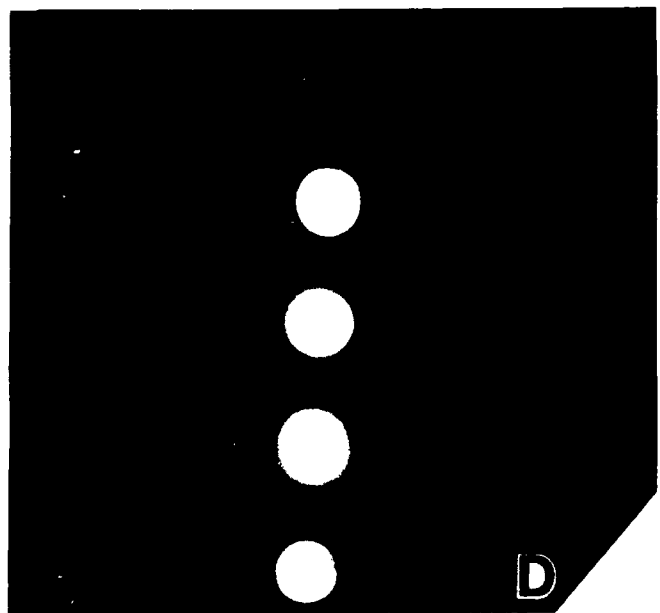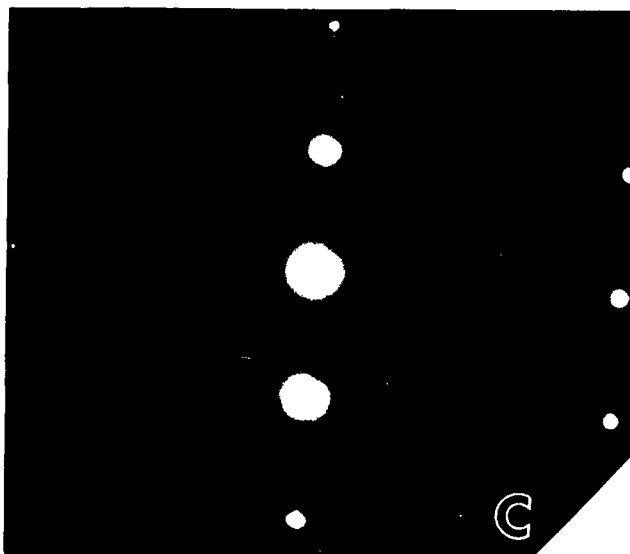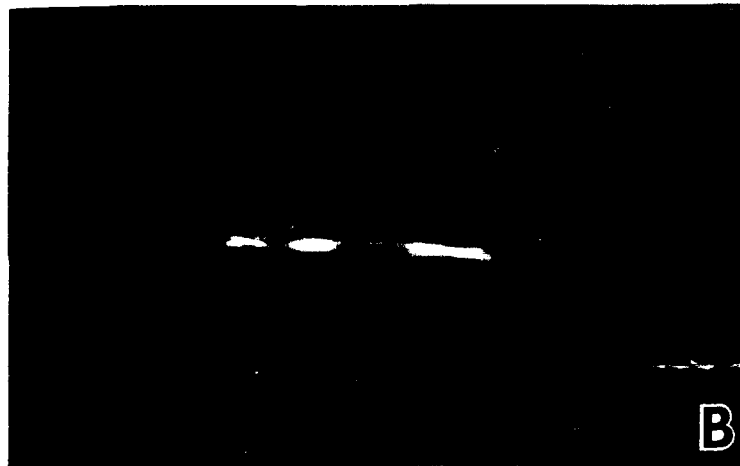
Figure 37.   Intragranular TiN Precipitate, Nb-1.2Ti-0.6N, Aged at 1200°C/4 hr

88—7—1—24

GENERAL VIEW OF THE MICROSTRUCTURE, TRAVERSED DIAGONALLY BY A GRAIN
BOUNDARY. GRAIN BOUNDARY PRECIPITATES AND LARGE, ELONGATED PRECIPITATES ARE
ZrO_2 AND Nb_2N, RESPECTIVELY. THE PLATE-SHAPED (SMALLEST) PRECIPITATES ARE ZrB.

0.5μm
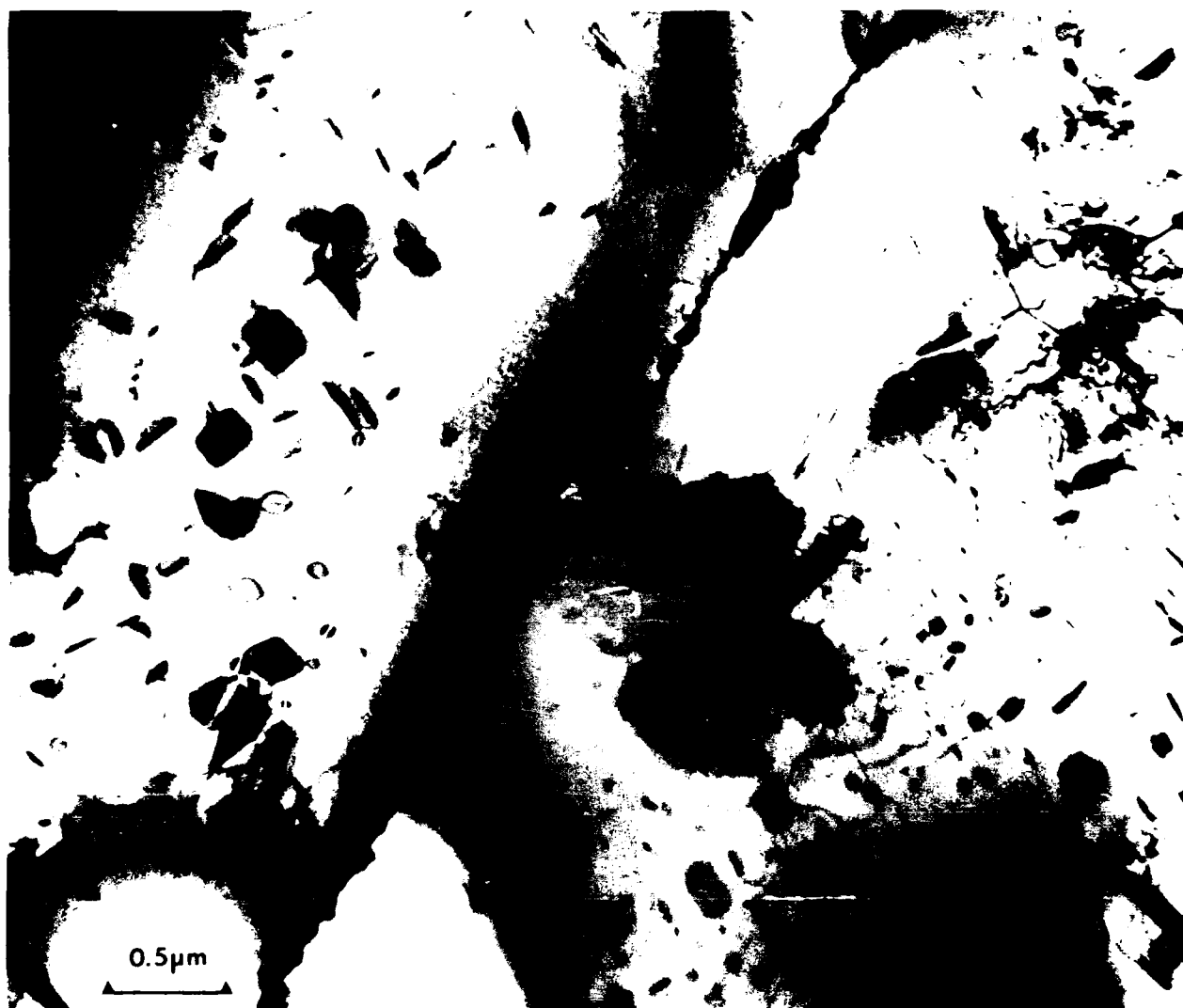
Figure 38.   Nb-0.2Zr-0.2B, Aged at 1200°C/4h; 1400°C/8h

DARK FIELD, $\overline{g} = <110>$ OF MATRIX

Figure 39.   Area in Left Grain, Fig. 38

89—6—73—5

DARK FIELD, $\bar{g}$ · ·310· OF MATRIX.
LIGHT CONTRAST SHOWS AREAS OF THE MATRIX BENT BY COHERENCY STRAIN.

0.2μm
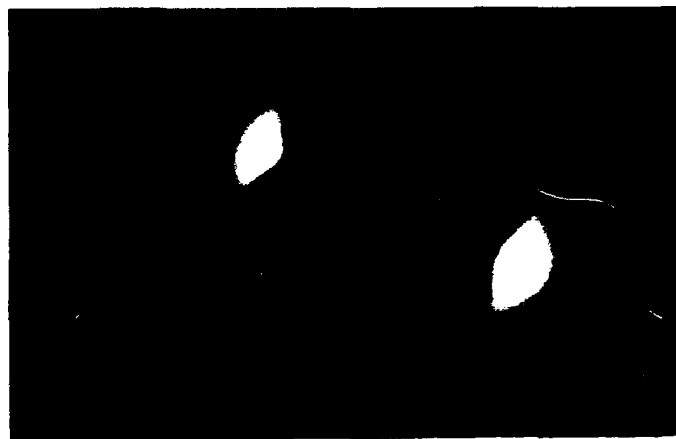
Figure 40.   Area in Top Center, Fig. 38

89—6—73—6

(A) BRIGHT FIELD. (B) DARK FIELD. (C) POINTER MARKS $\overline{g} = \cdot 200 \cdot ZrB$ USED FOR (B)

Figure 41.   Area in Upper Left, Fig. 38

(A) DARK FIELD. (B) POINTER MARKS $\overline{g} = \overline{2}00$ ZrB USED FOR (A).
(C) BRIGHT FIELD SADP FROM (A). POINTER BLOCKS 000.
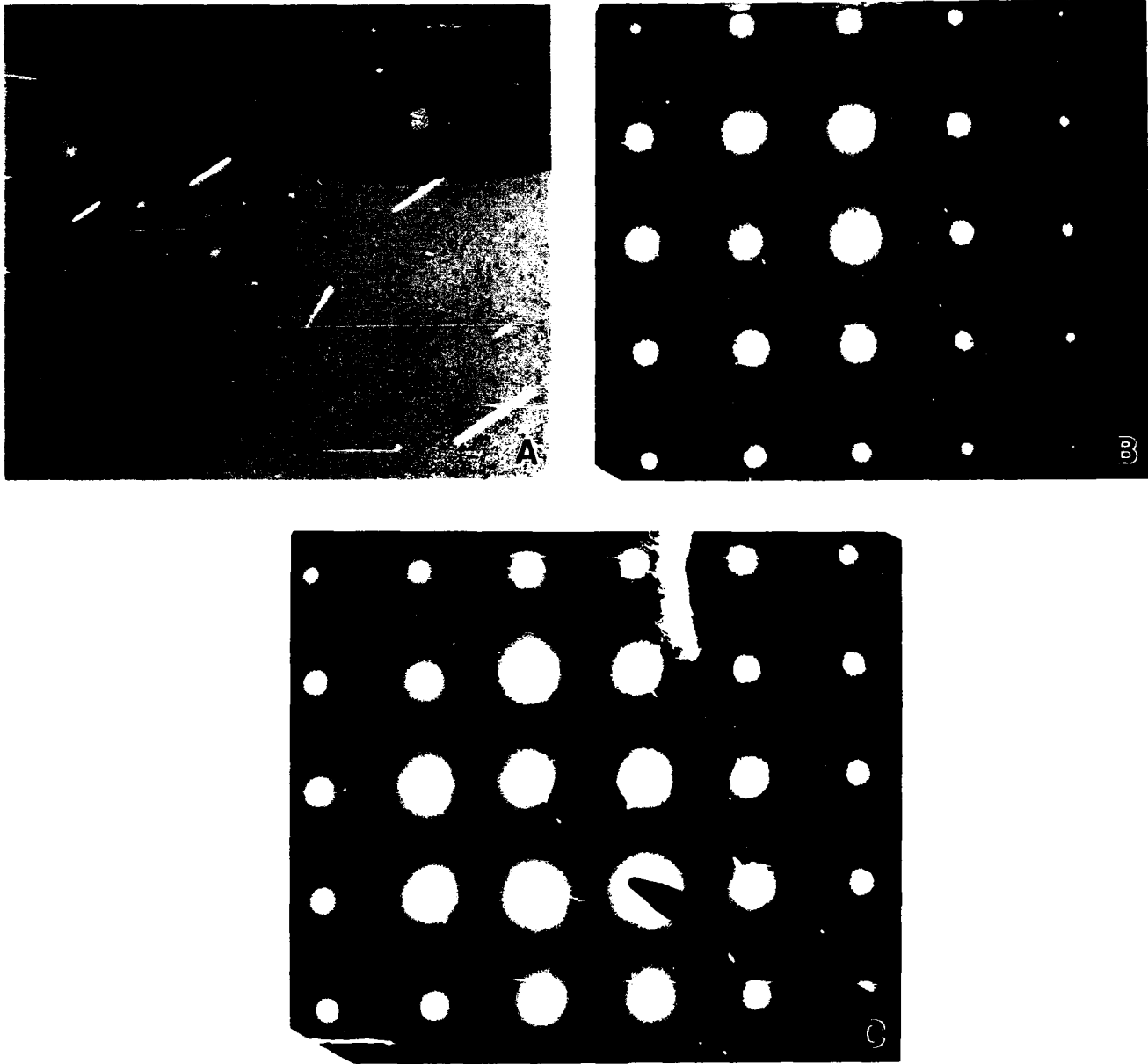
Figure 42.   ZrB Precipitates in Nb-0.2Zr-0.2B, Aged at 1200°C/4h + 1400°C/8h

72

SCHEMATIC OF SUPERIMPOSED SELECTED AREA DIFFRACTION PATTERNS,
[001] MATRIX AND [011] ZrB, CORRESPONDING TO FIGS. 30B AND 30C

BODY-CENTERED CUBIC Zone Axis = 001

FACE-CENTERED CUBIC Zone Axis = 011

Niobium Matrix
ZrB precipitate, one variant

Lattice Parameter(s): a = 3.3007 A
a = 4.647 A

Figure 43. Matrix and ZrB SADP's, Nb-0.2Zr-0.2B, Aged at 1200°C/4h + 1400°C/8h

73

89—6—73—2

(A) EDXS FROM ZrB PRECIPITATE MARKED BY ARROW, FIG. 42A.
120kV, 40nm SPOT SIZE
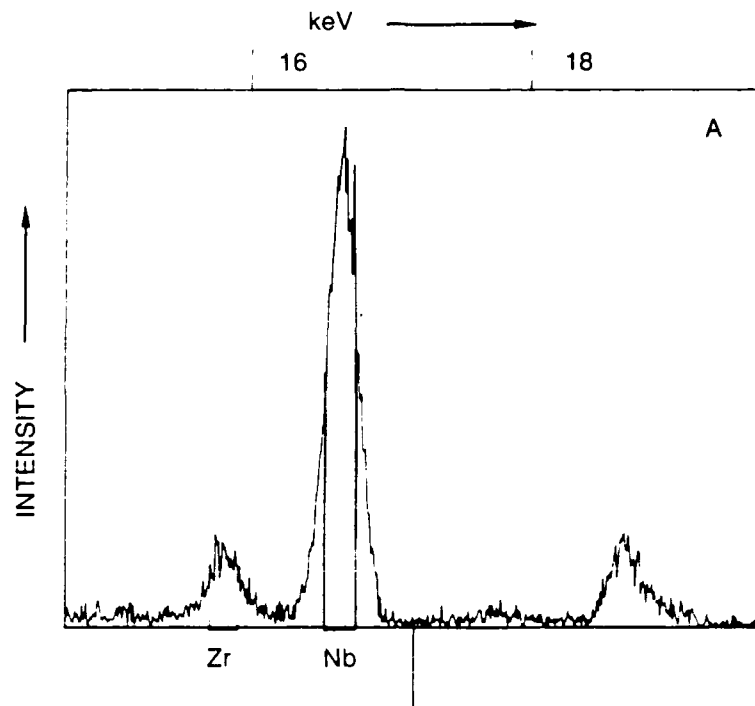
(B) EDXS FROM MATRIX, FIG. 30A
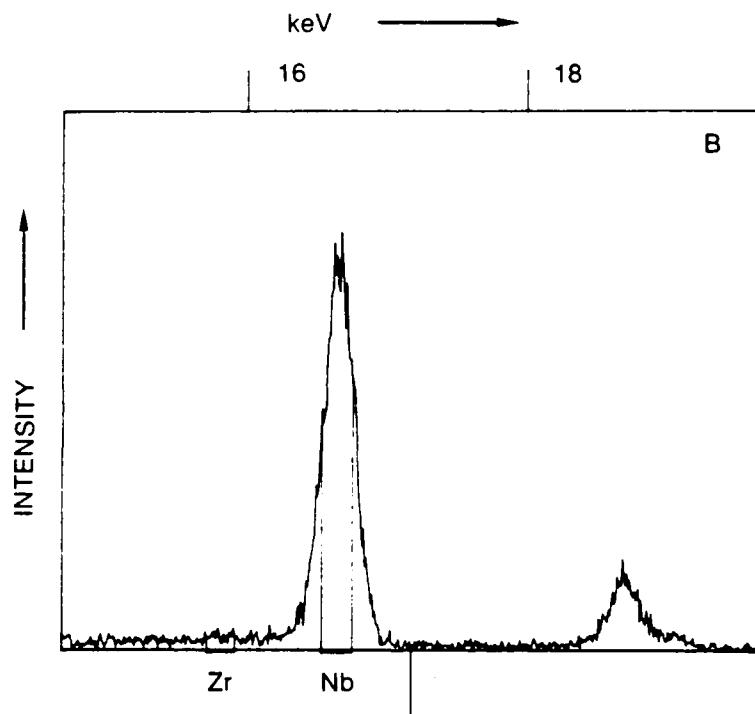
Figure 44.   Energy Dispersive X-ray Spectra from Area of Fig. 42

74

(A) BRIGHT FIELD, $\bar{\mathrm{B}}$ NEAR <001>. (B) DARK FIELD.
(C) SADP: POINTER MARKS $\bar{\mathrm{g}}$ =<400> HfN USED FOR (B).

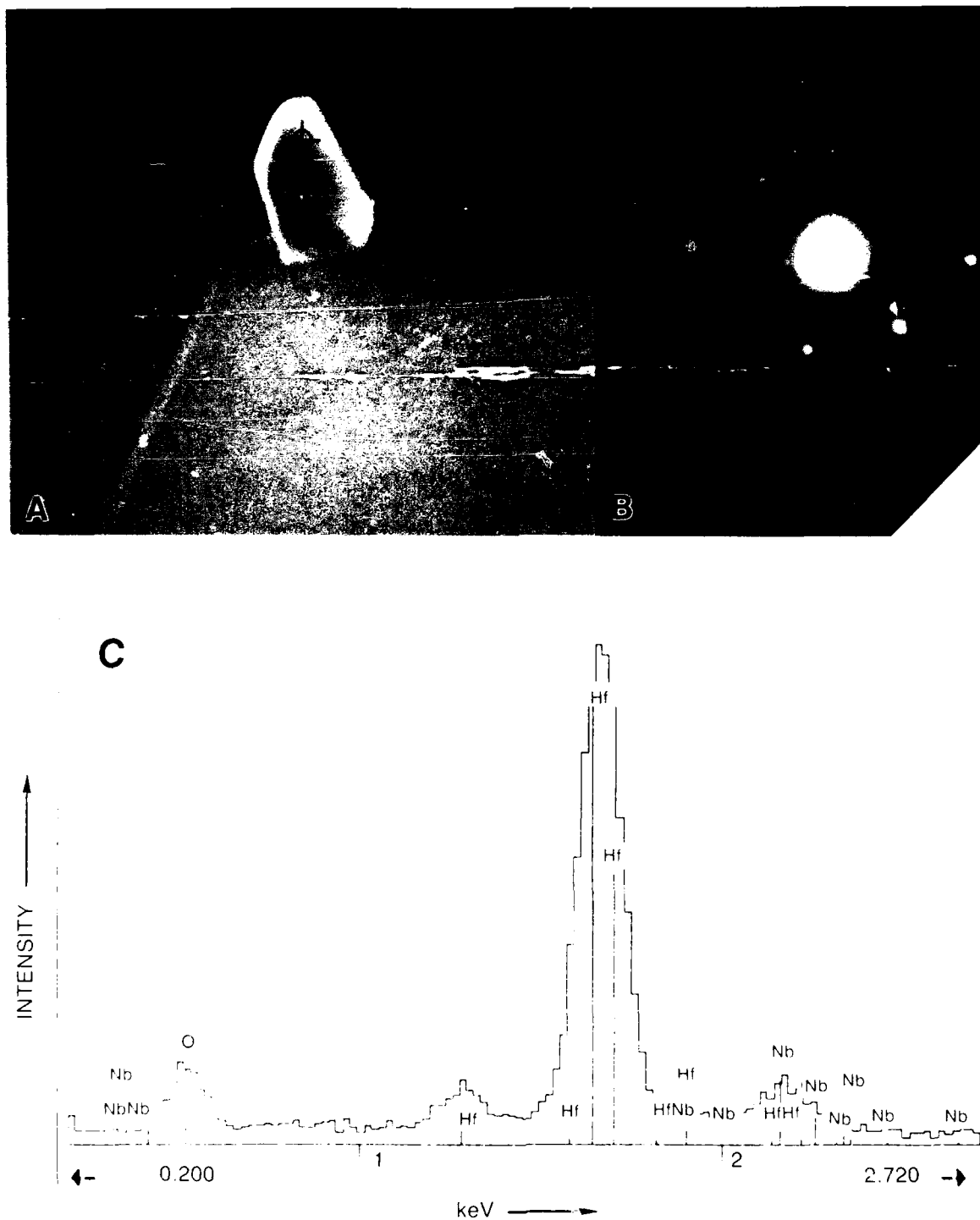**Figure 45. Hfn Precipitates in Nb-0.6Hf-1.2N (at%), Aged at 1200°C/4h + 1400°C/8h**

GENERAL VIEW OF THE MICROSTRUCTURE. GRAIN BOUNDARY PRECIPITATES
ARE HfO_2; LARGE, ELONGATED PRECIPITATES ARE Nb_2N;
AND PLATE-SHAPED (SMALLEST) PRECIPITATES ARE HfB.

1.0μm

Figure 46. Nb-0.6Hf-1.2N (at%), Aged at 1200°C/4h + 1400°C/8h

76

89-6 73-10

(A) DARK FIELD, GRAIN BOUNDARY HfO$_2$ AT FOIL EDGE (B) SADP;
POINTER MARKS $\overline{g}$ =<200>, $\overline{B}$ =<011>, MONOCLINIC Hf$_2$O.
(C) EDXS FROM Hf$_2$O, 120 kV, 5nm SPOT SIZE.

Figure 47. **HfO$_2$ Grain Boundary Precipitate in Nb-0.6Hf-1.2N (at%), Aged at 1200°C/4h + 1400°C/8h**
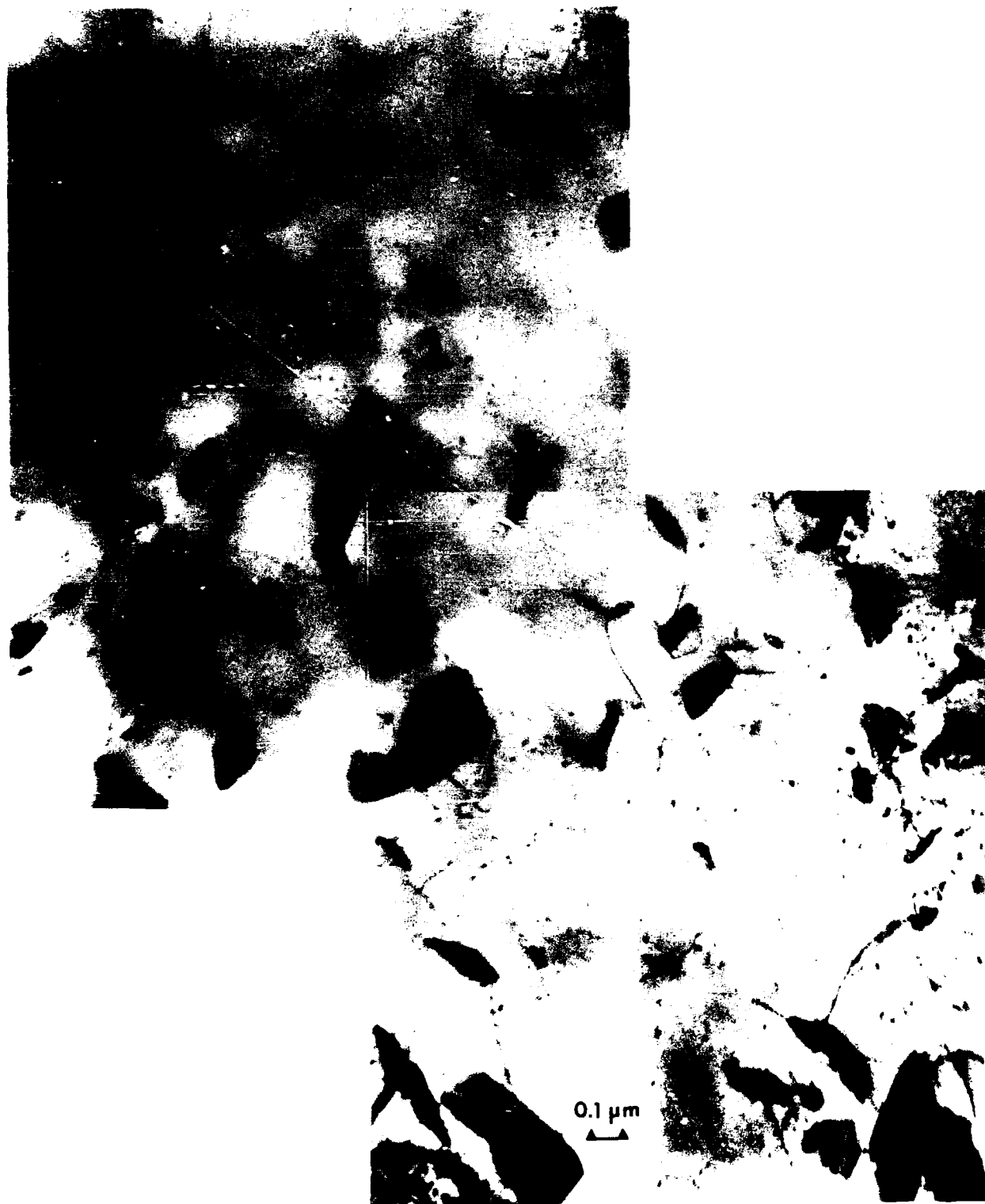
77

GENERAL VIEW OF THE MICROSTRUCTURE

Figure 48.   Nb-1.2Hf-0.6C (at%), Aged at 1200°C/4h + 1400°C/4h

78

(A) DARK FIELD IMAGE OF NbC PRECIPITATES. AREA TO LEFT OF THAT SHOWN IN FIG. 48.
(B) SADP. $\bar{B}$ NEAR $\langle 110 \rangle$ MATRIX. ARROW MARKS $\bar{g} = \langle 220 \rangle$ NbC USED FOR (A).
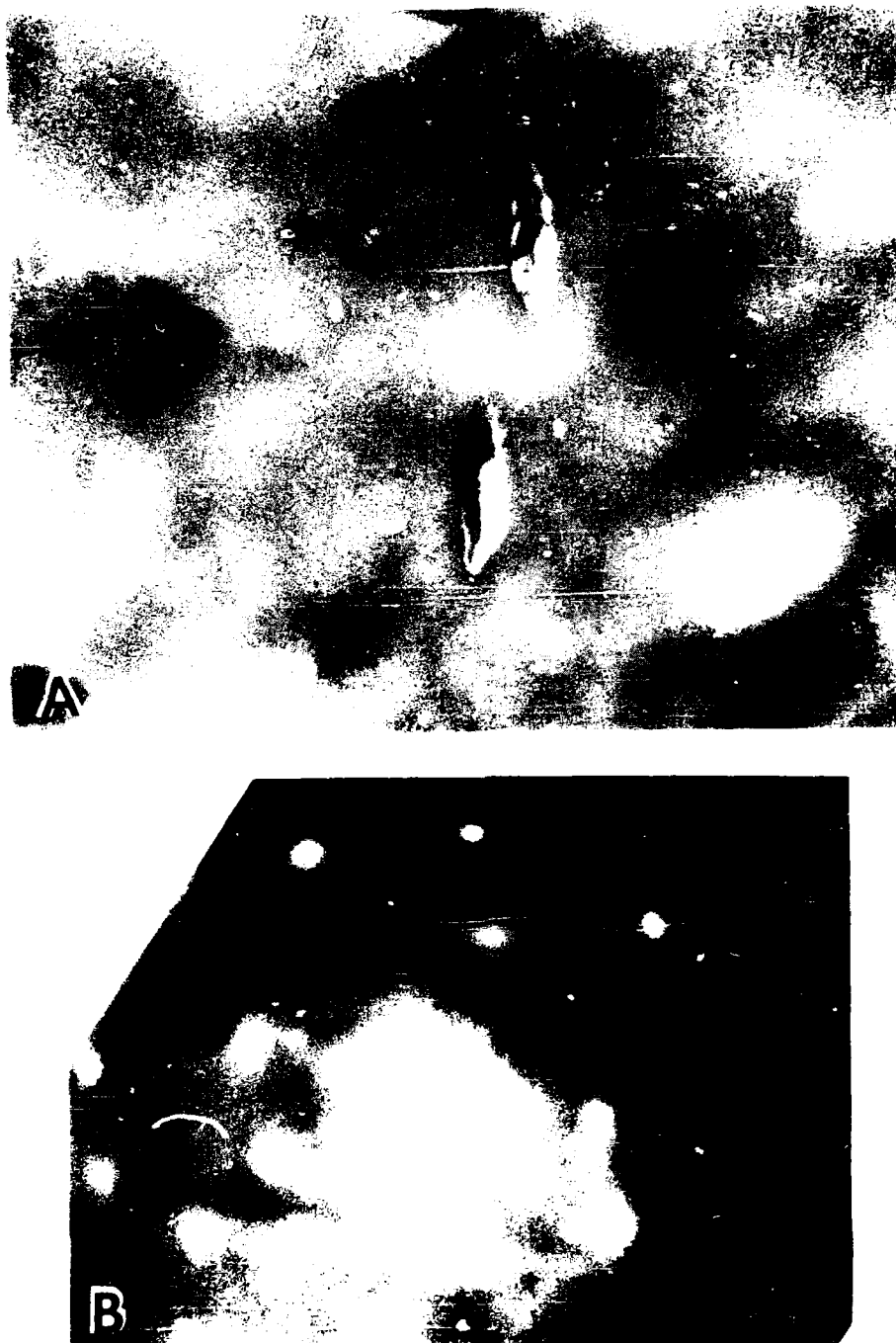

Figure 49.   Nb-1.2Hf-0.6C (at%). Aged at 1200°C/4h + 1400°C/n
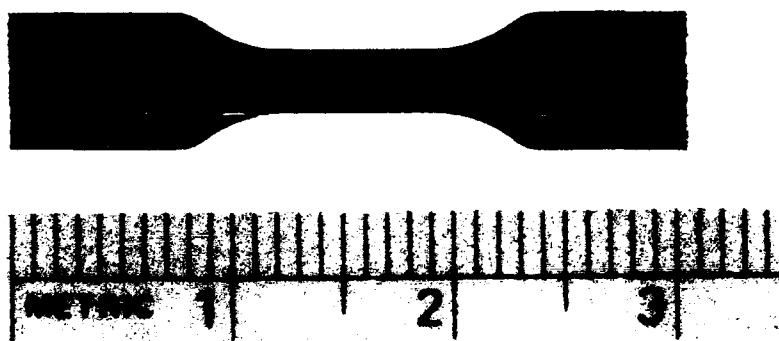
Figure 50. Splat Quenched Niobium Alloy Tensile Test Specimen

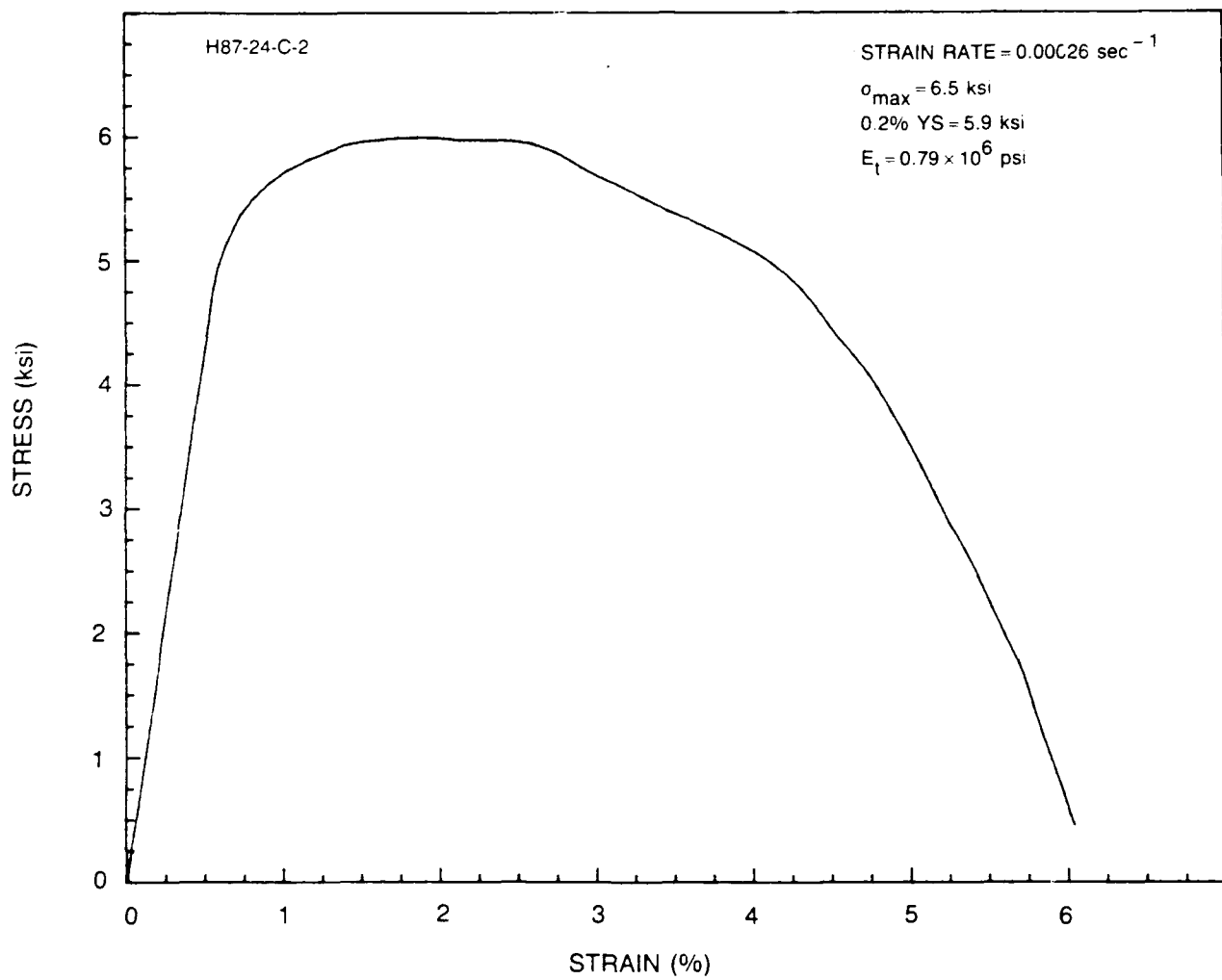89—6-73 19

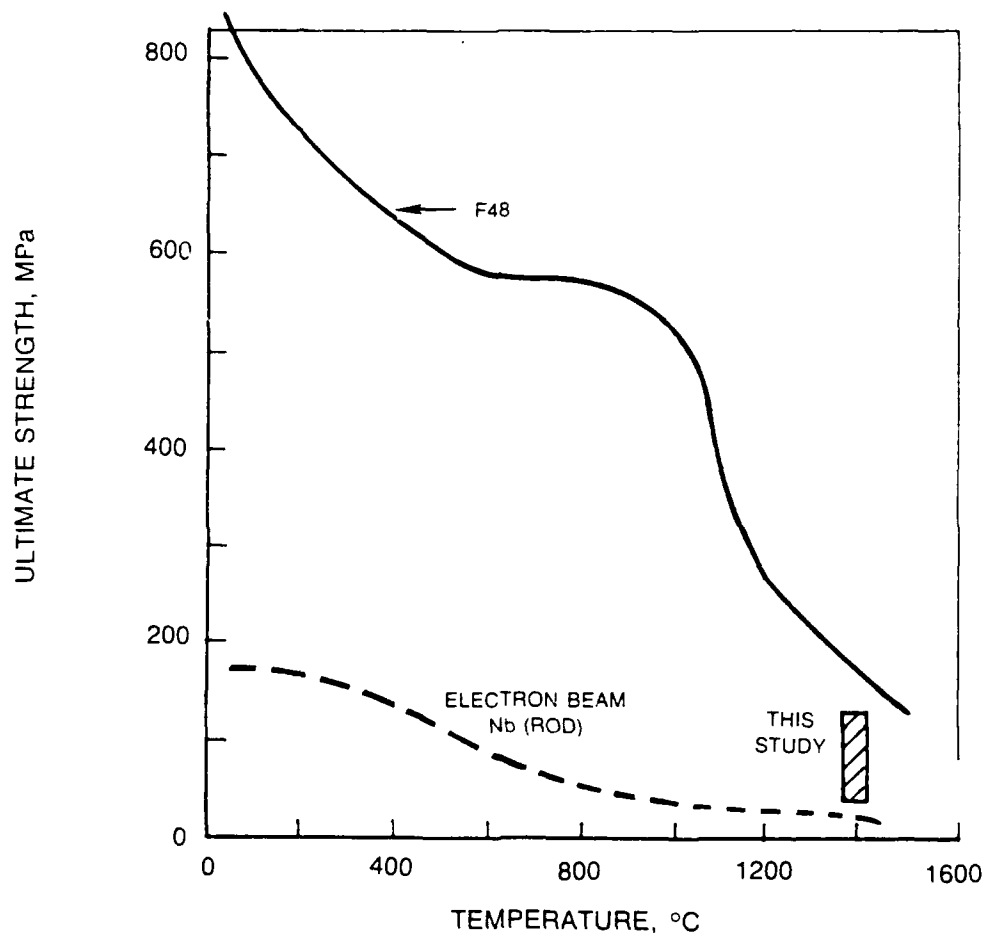Figure 51.   Typical Monotonic Tensile Test at 1400°C/Argon

89—6—73—20

Figure 52. Ultimate Tensile Strength Range of Rapidly Solidified Alloys of this Study when Compared to Highly Alloyed Sheet and Pure Nb Rod
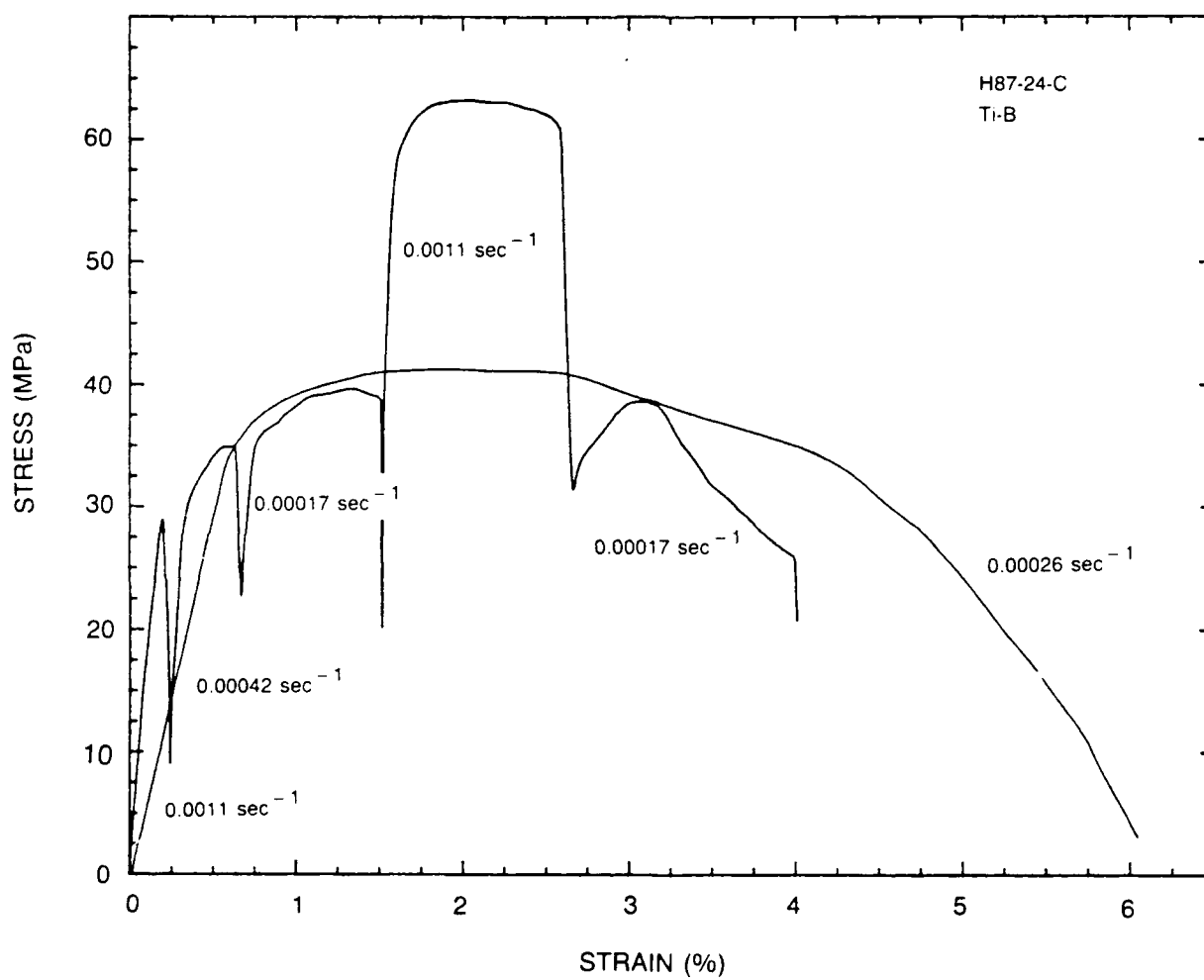
82

Figure 53. Strain Rate Sensitivity 1400°C/Argon

4.0 CONCLUSIONS

The splat quench and heat treatment procedures developed under this contract have proven themselves to be excellent means of fabricating reproducible rapidly solidified specimens of clean Nb alloys. Both microstructural investigations through analytical TEM and microhardness analysis were carried out successfully. High temperature tensile properties were also measured at 1400°C in purified Ar and no problems are foreseen in extending these tests to creep environments. However, the strain rate sensitivity tests were not found to yield the creep like response necessary to extrapolate properties into the long term/low stress regime.

Thermal aging at 1600°C/4 hr was found to over-age the rapidly solidified specimens. A prior heat treatment at 1200°C for 4 hours was successfully used to set a fine precipitate dispersion which was later coarsened at 1400°C through 16 hours. Coarsening of the precipitated particles was observed to follow an exponential law with the negative free energy of formation of the precipitate phase, as determined through micro-hardness testing. From this precipitate coarsening analysis, candidate precipitates were selected for further evaluation.

Both analytical transmission electron microscopy and thermal aging studies on alloys containing 0.1 at % refractory alloy additions showed these alloys to be inadequate with the refractory element being tied up with nascent oxygen and the carbon, nitrogen or boron forming the niobium equivalent. Additions of up to 0.6 at % refractory metal were found to be necessary to bring about a uniform precipitate dispersion of refractory metal compound. Also in these instances, large blocky oxides of the refractory metal were detected in the grain boundaries. Of the fine refractory metal precipitates observed here, none were fine discrete particles as obtained for the case of rare earth oxides in Ti alloys; in this case, thin plates and needles predominated. The heat treatment techniques used here were found to yield uniform dispersions of the precipitates sought.

Tensile testing of 0.015 cm (0.006") thick splats were conducted at 1400°C with stress and strain to failure results matching typically reported values reported in the literature. The measurement of the elastic modulus was found to be in error due to thermally activated deformation. The tensile test results did not compare with the hardness results obtained at room temperature. The strongest alloys at 1400°C could be grouped as follows: those with precipitates of the refractory metals Zr and Hf as either nitrides or borides; the commercial alloy with large additions of Mo, Ta and Zr; and the alloy containing TiN. Failure strains were generally on the order of 10%, strikingly high considering the foil nature and reactivity of the specimens.

REFERENCES

1. C. English, in Niobium, TSM-AIME, Warrendale, PA, 1981, p.239.

2. A. L. Hoffmanner, in Refractory Metals and Alloys IV, R. I. Jaffee, G. M. Ault, J. Maltz and M. Senichyshen eds., Gordon and Breach, New York, NY, 1965.

3. R. T. Begley, J. A. Cornie and R. C. Goodspeed, AFML-TR-67-116, 1969.

4. V. G. Grigorovich and E. N. Sheftel, Met. Sci. and Heat Treatment, 24, (7-8), 472 (1983).

5. M. McLean, Acta Met., 33, 545 (1985).

6. G. S. Ansell and J. Weertmann, Trans. AIME, 215, 838 (1959).

7. U. F. Kocks, Phil. Mag., 13,541 (1966).

8. R. W. Lund and W.D. Nix, Acta Met., 24, 469 (1967).

9. J. W. Martin and R. D. Doherty, Stability of Microstructures in Metallic Systems, Cambridge University Press, Cambridge, G. B. (1976).

10. E. A. Brandes, Smithells Metals Reference Book. 6th ed., Butterworth & Co., London, G. B. (1983).

11. J. Askill, Tracer Diffusion Data for Metals and Simple Oxides, Plenum Press, New York, NY (1970).

12. V. G. Grigorovich, E. N. Sheftel and G. S. Usmanov, "Aging in Niobium Alloys Hardened with Zirconium Nitrides", Izv. Akad. Nauk SSSR, Met., 6 (1980).

13. V. G. Grigorovich, E. N. Sheftel and G. S. Usmanov, Russ. Metall., 141 (1975).

14. J. R. Cost and C. A. Wert, Acta Met., 11, 231 (1963).

15. D. G. Konitzer and H. L. Fraser, in High Temperature Ordered Intermetallic Alloys, C. C. Koch, C. T. Liu and N. S. Stoloff eds., Materials Research Soc., Pittsburgh, PA (1985).

16. B. J. Kestel, Ultramicroscopy, 9, 379 (1982).

17. R. P. Elliot and S. Komjathy, in Columbium Metallurgy, Interscience Publishers, p.367, NY, NY (1960).

18. R. H. Hiltz, Jr., Columbium, ASM Metals Engineering Panel Conf., Metals Congress, Chicago (1959).

19. F. F. Schmidt, D. J. Maykuth and H. R. Ogden, DMIC Rept. 205, Battelle Mem. Inst., Columbus, OH (1964).

20. J. B. Cahoon, W. H. Broughton and A. R. Kutzak, Metall. Trans., 2, 1979 (1970).

21. I. M. Lifshitz and V. V. Slyozov, J. Phys. Chem. Sol., 19, 35 (1961).

22. C. Wagner, Z. elektrochem., 65, 581 (1961).

23. D. L. Anton, Unpublished Research (1985).

24. F. A. Shunk, Constitution of Binary Alloys, 2nd Supplement, p. 590, McGraw-Hill, New York, NY (1969).

25. A. Taylor and N. J. Doyle, J. of the Less Com. Metals, 13, 413 (1967).

26. D. B. Snow and D. L. Anton, Unpublished Research (1987)

27. M. Hansen, Constitution of Binary Alloys, p. 255, McGraw-Hill Inc., New York, NY (1958).

28. J. Mansfield, Convergent Beam Electron Diffraction of Alloy Phases, 87, 63, Adam Hilger, Bristol (1984).

29. P. E. Armstrong and H. L. Brown, Trans. ASM, 58, 30 (1965).

30. R. T. Begley and W. N. Platte, WADC TR57-344, AT33, Westinghouse Res. Labs. (1957).

31. D. P. Laverty and E. B. Evans, in Columbium Metallurgy, D. Douglas and F. Kunz eds., Interscience Publishers, New York, USA (1961).

32. T. K. Redden, in Columbium Metallurgy, D. Douglas and F. Kunz eds., Interscience Publishers, New York, USA (1961).